Origin of the Relation between Galaxy Morphology and its Gas Content

by

Shigeru V. Namiki

Dissertation

submitted to the Department of Astronomical Science

in partial fulfillment of the requirements for the degree of

Doctor of Philosophy

The Graduate University for Advanced Studies, SOKENDAI

February 2022

Contents

List of Figures

List of Tables

Acknowledgement

I'm proud of my past five years in SOKENDAI with Yusei Koyama. He has been a grateful supervisor, mentor, and co-investigator, who always gave me valuable advice and helpful comment. I couldn't have completed this thesis without his dedicated and patient cooperation.

I thank my assistant supervisors, Masato Onodera and Masayuki Tanaka. I also acknowledge my past supervisors, Nobunari Kashikawa and Ikuru Iwata. They have supported me in research and my daily life in Mitaka and Hilo.

I appreciate my collaborators, Shuhei Koyama, Takuji Yamashita, Masao Hayashi, Rhythm Shimakawa, Ken-ichi Tadaki, Tadayuki Kodama, and Ichi Tanaka. My study in Namiki et al. (2019) was possible through the critical contribution of N. M. Förster Schreiber, Jaron Kurk, and R. Genzel, who kindly cooperated with us to obtain the data of LUCI. Martha P. Haynes also let me access the radio spectra of the ALFALFA survey. Without her excellent support, I could not have completed Namiki et al. (2021) and this thesis. About the visual classification of simulated galaxies in Illustris, I thank Hugh Dickinson for kindly providing his catalog in Dickinson et al. (2018).

I would like to tell my gratitude to the referees of this thesis. I could improve the quality of my thesis through their review.

ALFALFA surveys, on which this work is based, were conducted at the Arecibo Observatory. The Arecibo Observatory is operated by SRI International under a cooperative agreement with the National Science Foundation (AST-1100968), and in alliance with Ana G. Méndez-Universidad Metropolitana, and the Universities Space Research Association.

Funding for the Sloan Digital Sky Survey (SDSS) and SDSS-II has been provided by the Alfred P. Sloan Foundation, the Participating Institutions, the National Science Foundation, the U.S. Department of Energy, the National Aeronautics and Space Administration, the Japanese Monbukagakusho, and the Max Planck Society, and the Higher Education Funding Council for England. The SDSS Web site is http://www.sdss.org/.

The SDSS is managed by the Astrophysical Research Consortium (ARC) for the Participating Institutions. The Participating Institutions are the American Museum of Natural History, Astrophysical Institute Potsdam, University of Basel, University of Cambridge, Case Western Reserve University, The University of Chicago, Drexel

University, Fermilab, the Institute for Advanced Study, the Japan Participation Group, The Johns Hopkins University, the Joint Institute for Nuclear Astrophysics, the Kavli Institute for Particle Astrophysics and Cosmology, the Korean Scientist Group, the Chinese Academy of Sciences (LAMOST), Los Alamos National Laboratory, the Max-Planck-Institute for Astronomy (MPIA), the Max-Planck-Institute for Astrophysics (MPA), New Mexico State University, Ohio State University, University of Pittsburgh, University of Portsmouth, Princeton University, the United States Naval Observatory, and the University of Washington.

This work was financially supported in part by Grants-in-Aid for Scientific Research (No. 18K13588) by the Japanese Ministry of Education, Culture, Sports and Science.

This report is based on data collected at Subaru Telescope, which is operated by the National Astronomical Observatory of Japan, as well as by observations made with the Large Binocular Telescope, which is an international collaboration among institutions in the United States, Italy, and Germany. LBT Corporation partners are: LBT Beteiligungsgesellschaft, Germany, representing the Max-Planck Society, the Astrophysical Institute Potsdam, and Heidelberg University; The University of Arizona on behalf of the Arizona university system; Istituto Nazionale di Astrofisica, Italy; The Ohio State University, and The Research Corporation, on behalf of The University of Notre Dame, University of Minnesota and University of Virginia.

My student's life was financially supported by the Department of Astronomical Science, SOKENDAI, and Research Corporation of the University of Hawai'i.

I gratefully acknowledge my co-worker outside of the research, Yuki Kashiwada, Yui Yamashita, Takuya Midooka, and all other organizers of Summer School on Astronomy and Astrophysics 2020.

I thank the support of my life in the Ph.D. course by Mizuho Inoue, Mihiro Fujimori, Kaori Kanou, Yumiko Omura, Yukiko Uemura, Yukie Matsuda, Kaya Kitabayashi, Masayo Nakajima, Noriko Otsuki, Satoko Chiba, Carolyn Nakasone-Medeiros, Kentaro Aoki, Akito Tajitsu, Yuhei Takagi, Tsuyoshi Terai, Masatoshi Imanishi, Saeko Hayashi, Yuu Niino, Takuma Izumi, Jun Hashimoto, Tomoko L. Suzuki, Taiki Kawamuro, Hisakazu Uchiyama, Haruka Baba, Masafusa Onoue, Tsuguru Ryu, Kotomi Taniguchi, Tomonari Michiyama, Moegi Yamamoto, Tadafumi Matsuno, Satoshi Kikuta, Misaki Ando, Masaki Yoshida, Nagaaki Kambara, Jungha Kim, Shaoo Ananya, Hiroyuki Tako Ishikawa, Satoshi Tanioka, Yoshiki Hatta, Noriharu Watanabe, Ko Hosokawa, Cui

Yuzhu, Kei Ito, Takafumi Tsukui, Shuichiro Tsuda, Ryotaro Ishikawa, Nao Fukagawa, Yongming Liang, Yuta Tanimoto, Hideaki Takemura, Takaho Masai, Suzuka Nakano, Raiga Kashiwagi, Yui Kasagi, Kanako Sugimori, Abdurrahman Naufal, Ryota Ikeda, and all colleagues and staffs of SOKENDAI, National Astronomical Observatory of Japan, Subaru telescope, Research Corporation of the University of Hawai'i, and Hilo base facility.

At last, I appreciate my family and friends, who always encourage me.

Abstract

The morphology of galaxies—the distribution of stellar components inside the galaxies—has long been believed to represent the evolutionary stages of galaxies. Many studies over the past decades demonstrated the relationship between the galaxy morphology and other physical parameters of galaxies, such as stellar mass (M_*), color, and star-formation rate (*SFR*). In this thesis, we focus on the amount of atomic hydrogen (H I) in the galaxies—a representative of the total gas content of galaxies available for their future star formation—and their morphology. We perform a stacking analysis of the H I 21 cm spectra from the Arecibo Legacy First ALFA (ALFALFA) survey for the optically selected local galaxies ($0.01 < z < 0.05$) drawn from the Sloan Digital Sky Survey (SDSS), to study the average gas fraction of galaxies at fixed M_* and *SFR*. The focus of this study is to investigate the morphological dependence of the H I gas mass fraction at fixed M_* and *SFR*, to minimize the effects of these parameters. We first confirm that the average gas fraction strongly depends on the stellar mass and *SFR* of host galaxies. Massive galaxies tend to have a lower gas fraction, and actively star-forming galaxies show higher gas fractions, consistent with many previous studies. We use three morphological classifications based on parametric indicator (Sérsic index), non-parametric indicator (C-index), and visual inspection (smoothness from the Galaxy Zoo 2 project) measured on the optical images. We find that there is no significant morphological dependence of the H I gas mass fraction at fixed M_* and *SFR* when we use C-index for the morphological classification. We confirm a similar result in the case that we use the Sérsic index for the morphological classification. However, we cannot draw a firm conclusion due to the small number of samples for the statistical discussion when using the Sérsic index. In contrast, interestingly, we demonstrate that the H I gas mass fraction for visually "smooth" galaxies is on average

$0.71^{\pm 0.11}$ dex lower than that of "non-smooth" galaxies with the same M_* and *SFR*. By comparing the visual morphology with other morphological indicators and inspecting the optical images of "smooth" and "non-smooth" galaxies, we find that the visual smoothness is sensitive to small-scale structures within the galaxies (spiral arms, barred bulges, and clumps). Our result suggests that even at fixed M_* and *SFR*, the presence of such small-scale structures (seen in the optical images) is linked to their total H I gas content. Motivated by the significant difference in the H I gas fraction between smooth and non-smooth galaxies at fixed M_* and *SFR* verified by the observations, we use the recent cosmological simulation (Illustris) to identify the physics behind the relationship between galaxy morphology and its H I gas fraction. We first confirm that the simulation reproduces the different gas fractions between smooth and non-smooth galaxies at fixed stellar mass and *SFR*, consistent with our observational results. By tracking down the formation history of galaxies in the simulated universe, we find that smooth and non-smooth galaxies have similar stellar mass growth and star formation histories. In contrast, they show a significant difference in the gas mass growth and their past merger histories in the stellar mass range of $M_* < 10^{11} M_\odot$. We argue that the consecutive merger events to the gas-rich disk would cause gravitational instability and structure formation inside the galaxies, resulting in different appearances and gas fractions at $z = 0$.

1 Introduction

1.1 Morphological classification of galaxies

Since the early study stage for external galaxies, people have recognized that galaxies can be classified into several categories. Hubble's tuning fork is one of the well-ordered sequences (Figure 1.1; Hubble 1936), which appears to show a possible evolution or formation of galaxies. The left side of Figure 1.1 is called as "early-type" and right side is "late-type". Early-type galaxies are also called "Elliptical" because they have a rounded shape, large bulge, and smooth light profile. Late-type galaxies are further divided into spirals and barred spirals. Both of them consist of the bulge, disk, and spiral arms. The difference between spirals and barred spirals is whether its bulge shows a spherical or rod-like shape.

After Hubble's tuning fork, the morphological classification of galaxies was developed by many authors. For example, de Vaucouleurs (1959) found that the surface brightness of the elliptical galaxy decreases in proportion to a quarter power of the distance from the center (de Vaucouleurs's law). Then Sérsic (1963) generalized de

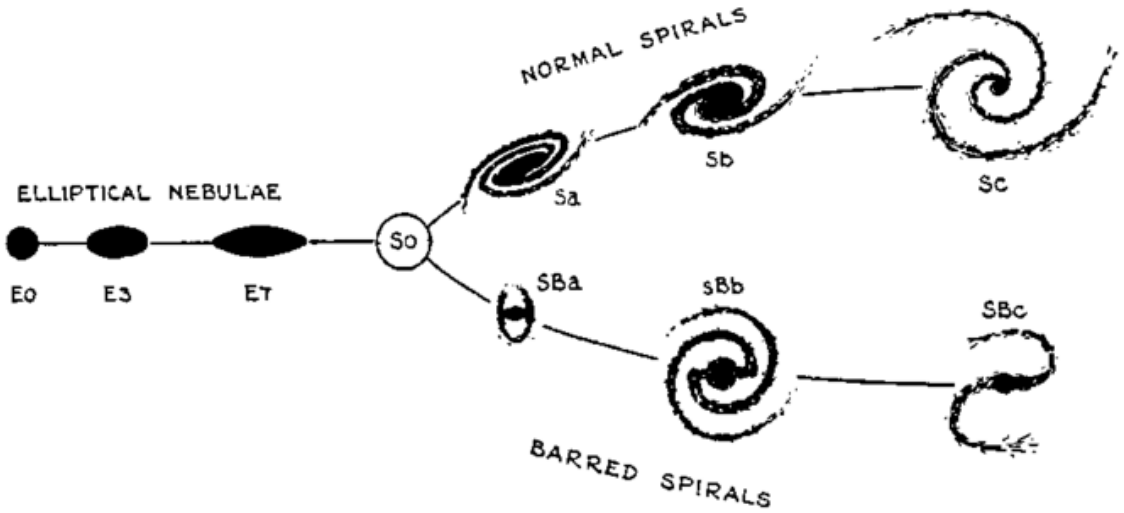

Figure 1.1: Tuning fork sequence defined by Hubble (1936, 1958).

Vaucouleurs's law as equation 1.1,

$$I(r) = I_e \left\{ -b_n \left[\left(\frac{r}{r_e} \right)^{1/n} - 1 \right] \right\}. \tag{1.1}$$

Here $I(r)$ is the surface brightness at the radius r, while r_e and I_e are the half light radius and surface brightness at r_e. If $n = 4$, equation 1.1 will be the same formula to de Vaucouleurs's law, and if $n = 1$, equation 1.1 will be so-called exponential disk profile. Thus the n of galaxies determined by the fitting of light profile is often used as an indicator of galaxy morphology (Sérsic index; e.g., Caon et al. 1993; Graham & Guzmn 2003; Ferrarese et al. 2006; Kormendy et al. 2009; Lange et al. 2015).

While Sérsic index is a parameter determined by the fitting of the integrated light profile, authors commonly use non-parametric measurements of galaxy light profile to evaluate the features of galaxy morphology too (e.g., Takamiya 1999; Conselice 2003, 2014). Concentration index (C-index) is a non-parametric indicator of morphology, often defined as the ratio of Petrosian half-light radius and 90 % light radius. Many authors demonstrated the tight correlation between the visual morphology and concentration index (e.g., Morgan 1962, 1958; Rix & Zaritsky 1995; Shimasaku et al. 2001) and used to investigate the relation between the galaxy morphology and other

parameters (e.g., Strateva et al. 2001; Wang et al. 2018; Koyama et al. 2019).

1.2 Galaxy morphology and other parameters

Previous authors have studied the relations among the parameters describing galaxy properties. Morphology is one of the commonly used parameters. For example, observations reveal that spiral galaxies have a blue color, while elliptical galaxies show red color (Tempel et al., 2011). Figure 1.2 shows the distribution of spiral (blue points) and elliptical galaxies (red points) on the plane of stellar mass (M_*) and $u - r$ color. Galaxies in Figure 1.2 is $z = 0$ galaxies selected from Sloan Digital Sky Survey (SDSS; York et al. 2000). Tempel et al. (2011) used the visual morphology determined by the citizen scientist and their own eyes (Galaxy Zoo, see Lintott et al. 2008 and Sec. 4.3). The vertical axis of Figure 1.2 means that the upper is red and the lower is blue in galaxy color. Because the color of the galaxy represents the dominant population of stars in that galaxy, Figure 1.2 suggests that elliptical galaxies mainly consist of old stars.

In contrast, a large part of stars in spirals is young stars. This also indicates the difference between star-forming history in elliptical and spiral galaxies. Optical spectroscopy supports this opinion. Kennicutt (1992) observed local galaxies classified along with Hubble's tuning fork + irregular galaxies and found many differences, e.g., the strength of blue continuum, stellar absorption features, and the existence of nebular emissions (Figure 4-22 in Kennicutt 1992). From all those features, we believe that elliptical galaxies have made a large part of their stars in the early epoch and stopped star-formation. On the other hand, both imaging and spectroscopic observations indicate that spiral galaxies are still actively forming their stars.

In addition to the color and star-formation activity, the environment is known to have a strong correlation with galaxy morphology. Dressler (1980) pointed out that, in the local universe, elliptical galaxies generally dominate the central regions of galaxy clusters. The number fraction of elliptical galaxies decreases towards the outskirt of the galaxy cluster, while that of spiral galaxies increases. Butcher & Oemler (1984) then showed that the number fraction of blue, spiral galaxies in the cluster region increases with the redshift at least $z < 0.5$. After the early work by Dressler (1980) and Butcher & Oemler (1984), many authors have been investigating the environmental

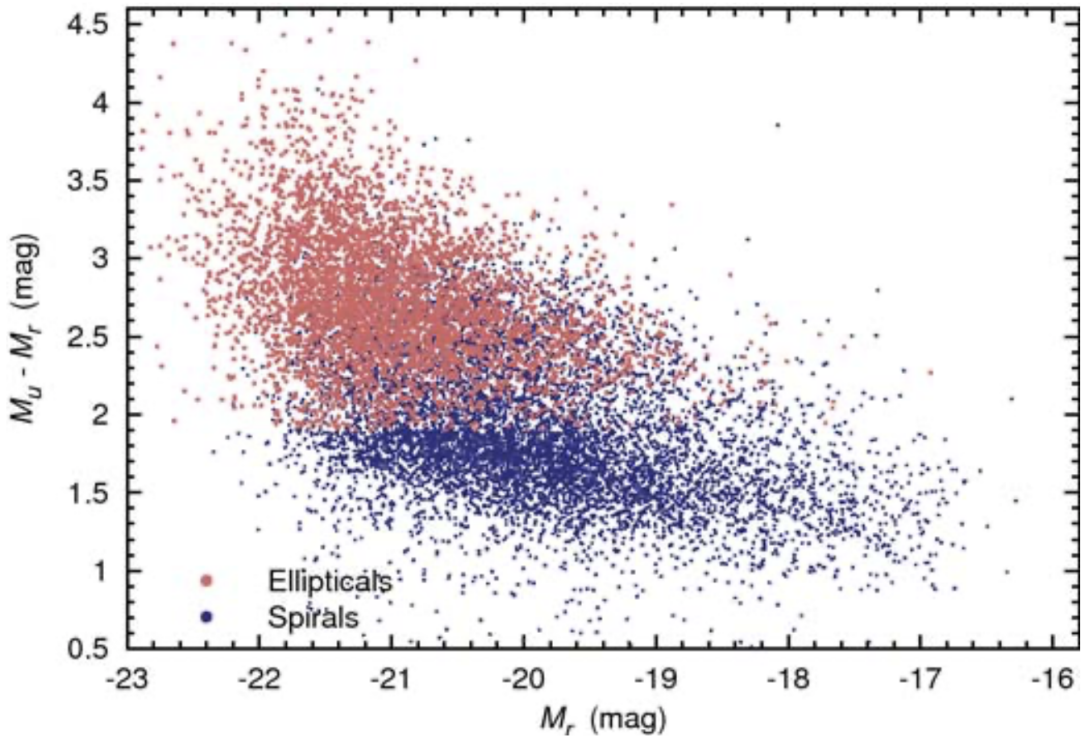

Figure 1.2: Color-magnitude diagram in Tempel et al. (2011). Blue and red points show spiral and elliptical galaxies, respectively.

impact on the galaxy morphology (e.g., Whitmore & Gilmore 1991; Wilman et al. 2009; Tempel et al. 2011; Wilman & Erwin 2012). The role of dense environment in the galaxy evolution is often explained by the dynamic interaction with the hot intergalactic medium (IGM; Gunn & Gott 1972; McCarthy et al. 2008; Kawata & Mulchaey 2008; Bekki 2009), galaxy merger (Darg et al., 2010; Ellison et al., 2010; Jian et al., 2012), and the tidal force (Malumuth & Richstone, 1984; Murante et al., 2004; Willman et al., 2004; Gonzalez et al., 2005). Some of them will directly change the morphology of galaxies, and others will affect them indirectly.

1.3 Morphology and gaseous component

While the relations between the galaxy morphology and its stellar properties like M_*, color, and the distribution of stars are well established, the morphological impact on the gaseous component in a galaxy is still under debate. Because many parameters correlate with each other in galaxy formation, it is not easy to clarify the importance of galaxy morphology within the study of the gas property of galaxies.

Galactic gas mainly consists of hydrogen, which exists in atoms and molecules. The observation in the local universe shows that molecular hydrogen (H_2) is located in the stellar disc of galaxies and that atomic hydrogen (H I) extends over the stellar discs (e.g., Walter et al. 2008; Leroy et al. 2008; Schruba et al. 2011). We can explain this difference of distribution by the simple scenario; some part of rotationally supported H I disc accretes to the stellar disc, gets cold and dense, and changes to the molecular state. Because molecular hydrogen is known to be a material of star-formation, this schematic view agrees with the fact that the cloud of molecular hydrogen inhabits along the star-forming region in the galaxy stellar disc (e.g., Oswalt & Keel 2013; Gusev et al. 2015).

1.3.1 Morphology and molecular hydrogen

Based on the idea that the mass of molecular hydrogen (M_{H_2}) correlates with the formation of young stars (e.g., Kennicutt 1998; Kennicutt & Evans 2012) and that star-formation activity and color of galaxies are related to the morphology, we may analogize the relation between the galaxy morphology and its M_{H_2}. On the other hand,

Martig et al. (2009) suggested the so-called "morphological quenching" scenario, in which the growth of stellar spheroidal in the system will stabilize the gravitational potential and suppress the star-formation. Because "morphological quenching" can stop the star-formation without gas removal, we will not see any morphological impacts on the amount of gas in that scenario. Observations of molecular gas in local galaxies revealed that the star-formation efficiency at the star-forming region indeed depends on the morphology of host galaxies, which is consistent with the morphological quenching scenario (e.g., Young et al. 2011; Martig et al. 2013; Davis et al. 2014). In contrast, by regulating the sample in the narrow M_* and star-formation rate (*SFR*) range, Koyama et al. (2019) demonstrated that there are no morphological impacts on the amount of molecular hydrogen without the effect of different stages of galaxy evolution. Koyama et al. (2019) observed the molecular gas in local bulge-dominant and disk-dominant galaxies and directly compared their M_{H_2}. The result of Koyama et al. (2019) is opposite to the morphological quenching scenario because a galaxy with a prominent bulge should have more gas not used in star-formation in that scenario.

Unfortunately, the number of available extragalactic sources is limited due to the high cost of observing the extended molecular hydrogen. For example, HERA CO-Line Extragalactic Survey (HERACOLES, Leroy et al. 2008) observed the CO emission line of 48 galaxies. Also, CO Legacy Database for GASS (COLDGASS, Saintonge et al. 2011) contains the information of molecular hydrogen for 222 galaxies. The extra COLDGASS (xCOLDGASS, Santini et al. 2017) expanded the number of samples, but it is still 532 galaxies.

1.3.2 Morphology and atomic hydrogen

Past studies have also discussed the relation between the gas mass of atomic hydrogen ($M_{\rm HI}$) and galaxy morphology since the middle of the 20th century (Roberts, 1969; Roberts & Haynes, 1994). The gaseous atomic hydrogen (H I) in the external galaxy has been often observed using H I 21 cm emission line. In the early epoch, authors could find the H I emission line only in the spiral galaxies (Roberts, 1963). Then, thanks to the expansion of the database of observed quantity for the extragalactic objects, we have become able to evaluate the morphological impacts on the H I gas mass. Roberts & Haynes (1994) divided galaxies along the Hubble sequence and studied various

properties of local galaxies. Figure 1.3 summarize the result, which shows that the H I gas mass depends on the morphology and that especially the ratio between the H I gas mass and total mass of the system is monotonically increasing from Elliptical to Irregular. Also, some authors have used the information of galaxy morphology to evaluate the H I deficiency. The H I deficiency parameter is calculated as a difference between the H I gas mass of reference sample ($M_{\mathrm{HI,\ ref}}$) and that of the observed galaxy. Haynes & Giovanelli (1984) calculated $M_{\mathrm{HI,\ ref}}$ by the following equation,

$$\log_{10} M_{\mathrm{HI,\ ref}} = a + b \log_{10} d \tag{1.2}$$

Here d is determined by the 25th B-band isophote radius, and a and b are coefficients correlated to galaxy morphology. Authors often used the H I deficiency parameter to estimate the effect of cluster environment (Gavazzi et al., 2008; Boselli et al., 2010; Hughes et al., 2013), which implicates the potential link between the H I gas mass, morphology, and environment.

Recent large surveys covering the huge area in the sky allowed us to obtain those parameters for many galaxies in the local universe. For example, GALEX Arecibo SDSS Survey (GASS; Catinella et al. 2013) measured ~ 800 extragalactic H I source and the Arecibo Legacy Fast ALFA (ALFALFA) survey (Haynes et al. 2018) provide the information of H I 21 cm line for $> 30,000$ objects. Now we can investigate the morphological dependence of the ratio between M_{HI} and M_* (H I gas fraction, $F_{\mathrm{HI}} = M_{\mathrm{HI}}/M_*$) of local galaxies in a more statistical way.

By using the data of the GASS survey and morphological classifications with optical images of galaxies, Calette et al. (2018) studied the M_*-F_{HI} scaling relation in early-type and late-type galaxies. The left column of Figure 1.4 showed that M_*-F_{HI} scaling relation of late-type galaxies are always beyond that of early-type galaxies at all M_* range. Therefore Calette et al. (2018) concluded late-type galaxies tend to have higher H I gas fraction than early-type galaxies at a given stellar mass. A more recent study by Cook et al. (2019) used extended GALEX Arecibo SDSS Survey (xGASS; Catinella et al. 2010, 2018) to investigate the relation between M_{HI} and the bulge-to-total ratio (measured with the 2-D Bayesian light profile fitting code (ProFit); Robotham et al. 2017) for local galaxies. Figure 1.5 shows that M_{HI} of star-forming galaxies do *not* depend on the bulge-to-total mass ratio, suggesting that the presence of bulge has little

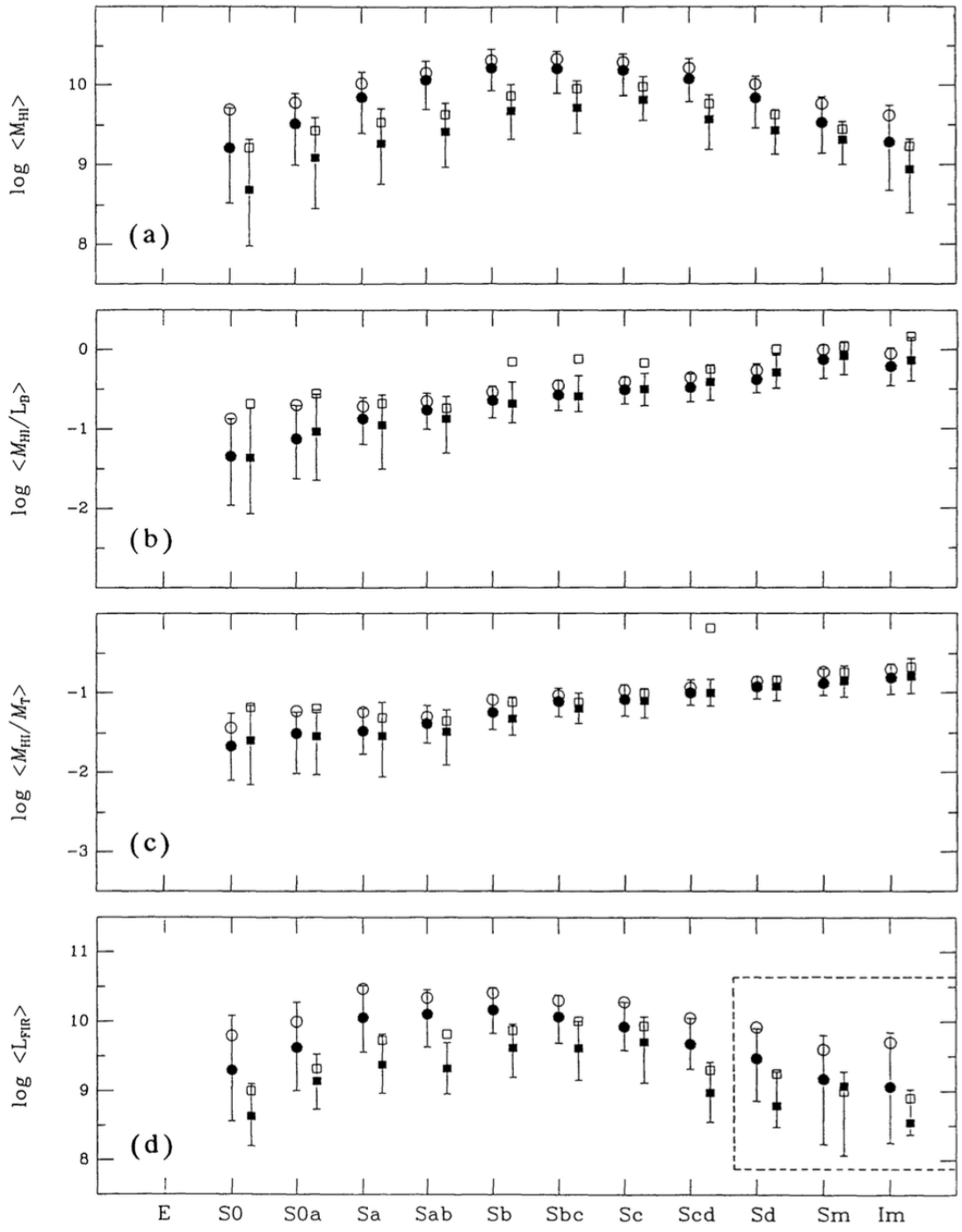

Figure 1.3: Figure 4 in Roberts & Haynes (1994) showing the morphological dependence of (a) H I gas mass (M_{HI}), (b) M_{HI} to blue light ratio, (c) M_{HI} to total mass ratio, and (d) far-InfraRed luminosity in logarithmic form. Horizontal axis is defined by the visual morphology along Hubble's tuning fork.

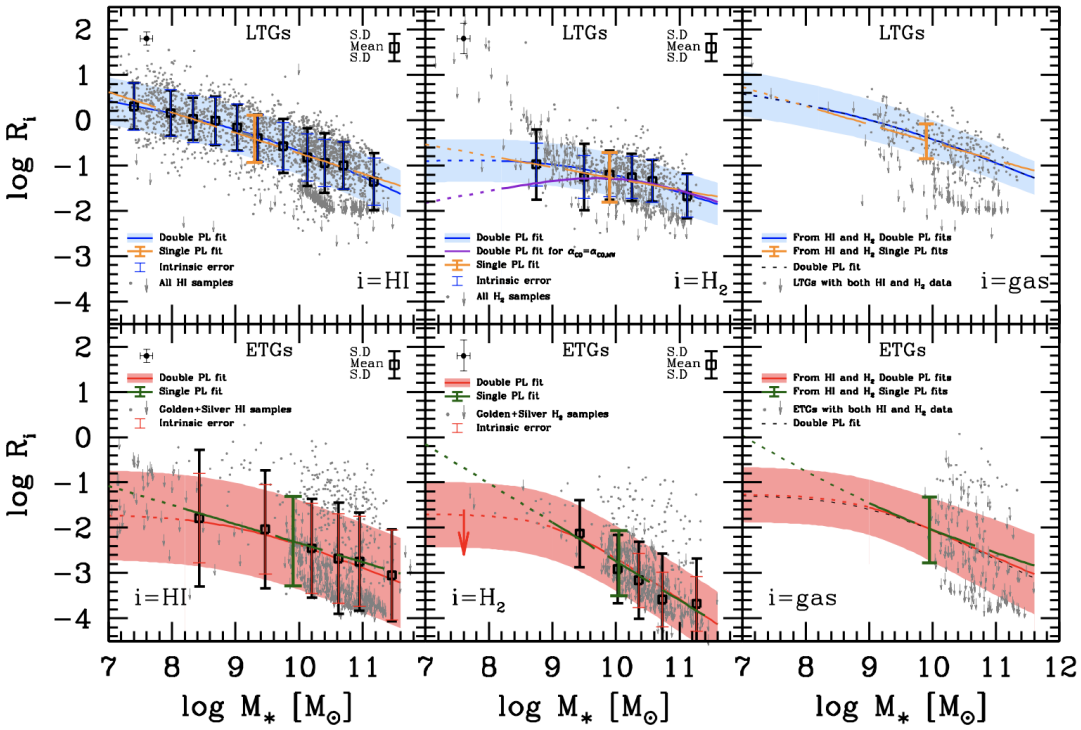

Figure 1.4: Figure 5 in Calette et al. (2018) showing the correlation between M_* and R_i. R_i is the ratio of H I gas mass (left), H_2 gas mass (middle), and total gas mass (right) to M_*. Upper row shows the result for late-type galaxies and lower is that for early-type galaxies. Calette et al. (2018) conducted the double/single power-law fitting to the data points (solid line) and extrapolated the fitting result towards the low-mass end (dashed line).

impact on their H I gas content.

1.4 Effect of stellar mass and *SFR*

While Calette et al. (2018) divided their sample into stellar mass bins, they did not split the sample by *SFR*s. Late-type galaxies are known to have higher *SFR*s than early-type galaxies in general and are expected to have a large gas reservoir. The morphological dependence reported in Calette et al. (2018) might be produced by the different *SFR* of the early- and late-type galaxies. Moreover, some outliers do not follow the general trend between the average star formation activity and gas

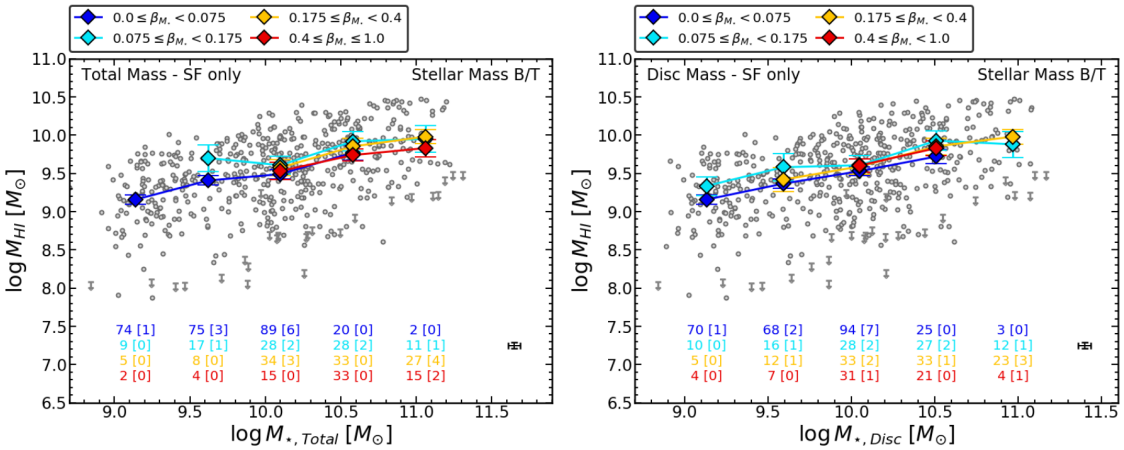

Figure 1.5: The H I gas mass against the total stellar mass (left) and the stellar mass only in the disc component (right). In this figure, Cook et al. (2019) used only star-forming galaxies and divided them into four bins by the bulge-to-total mass ratio (β_{M_*}). The points and lines are colored by β_{M_*}. Numbers in the bottom side show the total number of galaxies and (in bracket) that of H I non-detection in each M_* bin (color of number shows the β_{M_*} bin).

content or galaxy morphology, such as the H I-excess systems (early-type galaxies with large H I reservoirs and negligible star-formation; Geréb et al. 2016, 2018) or passive spirals (e.g., George 2017; Guo et al. 2020 but see also Cortese 2012). In the case of Cook et al. (2019), authors selected star-forming galaxies by simply excluding the quiescent galaxy population based on the distance from the star formation main sequence (Catinella et al., 2018; Janowiecki et al., 2019). Also, their morphological classification is different from that of Calette et al. (2018). In these ways, the sample definition and the morphological classifications vary from study to study, making it difficult to interpret the impact of galaxy morphologies on their H I gas content.

1.5 Origin of morphological impact

Even when morphological impacts on the H I gas exists, it is not easy to understand the background physics. We can consider many physical processes which can change the galaxy morphology and its H I gas content; e.g., change of mass distribution, loss of angular momentum, shut down of star-formation, and merger event. However, it is

difficult to distinguish which process is dominant with the current observations.

Cosmological simulation can give us the hint of dominant physics. The combination of numerical simulation of dark matter halos and hydrodynamical calculation within each halo succeeded in reproducing many trends in the local universe, such as star-formation main sequence and mass-metallicity relation. The advantage of simulation is that we can easily trace the formation history of individual galaxies. For each timestep, much information about galaxies is calculated based on the data one step before, and then it will be used for the following calculation. Because that information is conserved at each timestep, it is possible to look back at the formation history of the simulated galaxy.

In addition, the physical parameters and the images of simulated galaxies are getting similar to real galaxies. Illustris is one of the successful cosmological simulations. Torrey et al. (2015) generated the "observationally realistic" images for simulated galaxies at $z = 0$ in Illustris project (Snyder et al., 2015). The authors used these images to measure the morphology of simulated galaxies and compared them to observed galaxies in the local universe (D'Onofrio et al., 2019; Dickinson et al., 2018). Combining those images and the feature of the simulation technique, we can investigate the relationship between the morphological population of the simulated galaxy and its formation history.

1.6 Our work

So far, we have summarized the importance of understanding the morphology of galaxies and many discussions in the past one hundred years. Now we know that morphology is strongly correlated to the M_*, color, and *SFR*, but how about the gaseous properties? Because the atomic and molecular gas in galaxies is the material of star-formation, it can be related to the morphological type of host galaxies. In general, massive ellipticals are gas-poor while star-forming spirals are gas-rich, but is it the correlation between the morphology and gas properties? Isn't it the effect of different M_* and *SFR* between classical ellipticals and spirals? Even after thirty years of discussion, the connection between the galaxy morphology and its gas content is not brought to light, mainly due to the difficulty of removing the effect of M_* and *SFR* (Catinella et al., 2018; Cook et al., 2019).

In our study, we will revisit this problem -whether the morphological impact on the H I gas mass exists or not after removing the effect of M_* and *SFR*. We divide local galaxies by their M_*, *SFR*, and morphology in order to compare the average gas fraction of galaxies with the same M_*, the same *SFR*, and the different morphology. We also adopt multiple morphological indicators to inspect the dependence on morphological classification. As a result, only the visual morphology can distinguish gas-rich and gas-poor galaxies, while Sérsic index and concentration parameter cannot do that.

In order to investigate the physical origin of different H I properties in the different morphological populations, we then study the formation history of simulated galaxies. Here we use the result of Illustris, a recent cosmological simulation (Vogelsberger et al., 2014a,b; Genel et al., 2014; Nelson et al., 2015a). Torrey et al. (2015) and Snyder et al. (2015) created the synthetic images of simulated galaxies and Dickinson et al. (2018) conducted the morphological classification of those images. We choose simulated smooth and non-smooth galaxies from the sample in Dickinson et al. (2018), divide them by their M_* and *SFR* at $z = 0$, and trace their average formation history. We then consider the possible mechanisms behind the different H I gas property between visually smooth and non-smooth galaxies at the fixed M_* and *SFR*.

Throughout the main body of this thesis, we adopt flat ΛCDM cosmology with $\Omega_m = 0.3$, $\Omega_\lambda = 0.7$, and $H_0 = 67.8$ km s^{-1} Mpc^{-1} and Chabrier Initial mass function (Chabrier, 2003). We also note that we will use "morphology-gas fraction/mass relation" as a meaning of "morphology-gas fraction/mass relation at fixed stellar mass and star-formation rate". The observation part in this thesis is based on Namiki et al. (2021). We also summarize another study completed in the SOKENDAI Ph.D. course in Sec. B (Namiki et al., 2019).

2 Data

To investigate the morphology dependence of H I contents in local galaxies without the effect of M_* and *SFR*, we need not only H I information but also various parameters of the host galaxies. A combination of the large data sets from GALEX-WISE-SDSS Legacy Catalog 2 (GSWLC2, Salim et al. 2018) and Arecibo Legacy Fast ALFA (ALFALFA) survey (Haynes et al., 2018) enables us to study the H I gas properties of galaxies statistically and in an unbiased way.

2.1 GALEX-WISE-SDSS Legacy Catalog

GALEX-WISE-SDSS Legacy Catalog (GSWLC) is developed in Salim et al. (2016) and contains $\sim 700,000$ galaxies with the redshift below 0.3 in SDSS. The physical property of galaxies is derived from the optical and UV image from SDSS and the Galaxy Evolution Explorer (GALEX; Morrissey et al. 2005). Salim et al. (2016) conducted the spectral energy distribution (SED) fitting using CIGALE (Noll et al., 2009), which is a python code designed to create the grid of SEDs including model star-formation history,

dust-attenuation, and emission-line flux. Authors evaluated the modeled optical/UV SEDs with the reduced χ^2 and the correlation of SED-based *SFR* to the mid-IR/Hα-based *SFR*s. Here authors do not include the Near-Infrared band in their SED fitting to keep low reduced χ^2 and good correlation between mid-IR and Hα-derived *SFRs*. The detail of their calculation is summarized in Sec. 5 of Salim et al. (2016).

After the release of GSWLC, Salim et al. (2018) improved the technique of their SED fitting and revised GSWLC to GSWLC2. Authors calibrated the relation between mid-IR flux from the Wide-field Infrared Survey Explorer (WISE; Wright et al. 2010) and total IR luminosity based on the far-IR/sub-mm flux from *Herschel*, 22 μm flux from WISE, and fitting template by Chary & Elbaz (2001). After the calibration, total IR luminosity is calculated for all samples, and it is treated as a new "flux" point in SED fitting (SED+LIR fitting). Their method can make the parameters for dust attenuation free and balance the dust emission in IR and the dust absorption in the UV through near-IR. Please check Salim et al. (2018) for the detail of SED+LIR fitting.

2.2 ALFALFA survey

A hydrogen atom consists of a proton and an electron. Because both of them have a spin quantum number of 1/2, the hydrogen atom has a hyperfine structure by the interaction of magnetic dipoles. When the angular momentum of electron and proton are parallel, hydrogen atoms are at a higher energy state than that with antiparallel spin. Therefore, a transition between these two states generates a line spectrum. Using introductory quantum physics, we can calculate the difference of two energy levels (ΔE). Then we obtain the frequency and wavelength of this emission line, 1.420405751786 GHz and 21.106114 cm, respectively.

Here we use the data of the ALFALFA survey. The ALFALFA survey was carried out with the seven-horn Arecibo L-band Feed Array (ALFA). Its principal science goal is to determine the faint end of the H I mass function in the local Universe ($z < 0.05$). For its purpose, the ALFALFA survey observed nearly 7000 deg^2 of high Galactic latitude sky from 2005 to 2011 and searched for H I 21 cm emission line between 1335 and 1435 MHz. This emission line can be detected in the radio telescope. ALFALFA survey sampled the radio spectra in $1'.05$ declination with a drift scan technique. The technical details of the ALFALFA survey are shown in Haynes et al. (2018).

2.3 Our sample

In our analysis, we use GSWLC2 to obtain the stellar mass and the star formation rate of $\sim 700,000$ galaxies. We cross-matched the GSWLC2 catalog with the MPA-JHU catalog (Abazajian et al., 2009) of SDSS DR7 to obtain the spectroscopic redshift of each target. We then select 32,717 galaxies (with $0.01 < z < 0.05$) located within the footprint of the ALFALFA survey. Here we note that 14,252 galaxies having companions within the cut-out region of radio spectra (4 arcmins; see Sec.3.2) are excluded to avoid overestimating H I gas mass and the effect of galaxy-galaxy interaction. We do not apply any criteria for stellar mass, color, or redshift to identify companions, which increases the number of discarded galaxies that are potentially not accompanied. However, in this study, we conservatively discard all galaxies having any companion within the cut-out region of H I emission line. In the following analysis, we restrict the sample to 18,465 galaxies with M_* and SFR range of $9.0 < \log_{10} M_* < 12.0$ and $-2.0 < \log_{10} SFR < 2.0$. In addition, considering the possible effect of active galactic nuclei (AGN) in our analysis, we conduct AGN diagnosis using BPT diagram (Baldwin et al., 1981; Kauffmann et al., 2003; Kewley et al., 2013). Here we used the [O III], [N II], Hα and Hβ emission line fluxes of individual galaxies from the MPA-JHU catalog. We require our sample to have meaningful flux for all four emission lines.In other words, we eliminate 4106 galaxies for which Abazajian et al. (2009) could not measure their emission lines correctly. Then we check the position of our sample on the BPT diagram (Figure 2.1). We follow Kauffmann et al. (2003) and use Eq. 2.1 and 2.2 to cut the AGN candidates.

$$\log([\mathrm{OIII}]\lambda 5007/\mathrm{H}\beta) = 0.61/(\log([\mathrm{NII}]\lambda 6584/\mathrm{H}\alpha) - 0.05) + 1.3 \tag{2.1}$$

$$\mathrm{NII}]\lambda 6584/\mathrm{H}\alpha < 0.6 \tag{2.2}$$

3472 galaxies are excluded in Figure 2.1 (grey points) and this study uses the remaining 10,887 galaxies as our parent 'star-forming' galaxy sample.

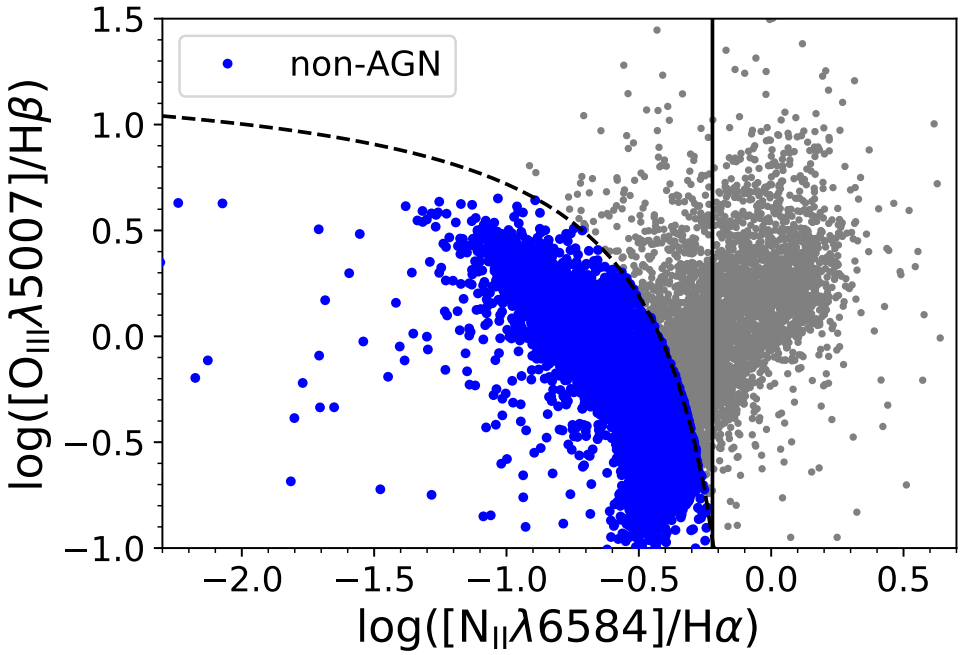

Figure 2.1: The distribution of our sample on BPT diagram (Kauffmann et al., 2003). Grey points shows galaxies exclueded as possible AGN candidates. Blue points shows our 'star-forming' sample. Black dashed and solid lines are the criterion of Eq. 2.1 and 2.2, respectively.

3

Measurement of average H I gas mass in the local universe

3.1 Conversion from H I flux to H I mass

The H I gas mass, $M_{\rm HI}$, is derived from the 21 cm line flux (Roberts, 1963) in this thesis. Although the H I-detected source catalog from the ALFALFA survey is already public (Haynes et al. 2018), directly using the H I-detected source catalog may cause a potential bias towards the H I-rich galaxies due to the detection limit. Therefore we go back to the original radio spectra obtained in the ALFALFA survey and utilize a stacking analysis to include the contribution of the galaxies without the detection of H I 21 cm line.

As we mentioned in Chapter 2.2, H I 21 cm line is originated from the transition between the upper and lower state of the hyperfine structure. Meyer et al. (2017) assumes that 3/4 of hydrogen atoms are in the upper state of hyperfine structure and

derive the following equation,

$$N_{\rm HI} = \frac{L}{\frac{3}{4}A_{\rm HI}\Delta E}, \tag{3.1}$$

where $N_{\rm HI}$ and $A_{\rm HI}$ are the number of H I atoms and the transition rate between two state of hyperfine structure, respectively. Then the H I mass of source is easily given by the following equations,

$$\begin{aligned} M_{\rm HI} &= m_{\rm HI}N_{\rm HI} && (3.2)\\ &= \frac{4m_{\rm HI}L}{3A_{\rm HI}\Delta E} && (3.3)\\ &= \frac{16\pi D_L^2 S_{rest} m_{\rm HI}}{3A_{\rm HI}\Delta E} && (3.4)\\ &\simeq \frac{2.35\times10^5}{(1+z)^2}\left(\frac{D_L}{\rm Mpc}\right)^2\left(\frac{S_{Vobs}}{\rm Jy\ kms^{-1}}\right) && (3.5) \end{aligned}$$

From eq.3.3 to eq.3.4, we use the relation between total luminosity L and flux S_{rest} at the rest frame velocity. Then we change S_{rest} to the observed flux, S_{Vobs}, and insert the value of $m_{\rm HI}$, $A_{\rm HI}$, and ΔE. We use eq.3.5 to calculate the mass of atomic hydrogen from ALFALFA radio spectra. Here, $D_L(z)$ is the luminosity distance, and z is the redshift to the source. The lower limit of detectable H I gas mass depends on the distance to the object. More distant galaxies with less H I gas, therefore, might not be detected through the pipeline of the ALFALFA survey.

To avoid this potential bias, we apply the H I stacking analysis including the non-detected object, following the previous studies (e.g., Fabello et al. 2011, Brown et al. 2015). The radio spectra around H I 21 cm line of our sample ($8' \times 8'$ square) are extracted from the full volume ALFALFA data cubes using R.A., Dec, and cz in the MPA-JHU catalog regardless of the detection of H I 21 cm line. A spectrum of one galaxy has two polarizations and contains velocity, flux, and quality weight w for each velocity bin. The quality weight w evaluates the effect of radiofrequency interference and/or hardware issues, ranging from 0 (unusable data) to 1 (good data). We discard velocity bins with $w < 0.5$ and take the average of two polarizations. If more than 40% of velocity bins have w less than 0.5 in a spectrum, we exclude such spectrum from our

stacking analysis. Forty galaxies are removed through this procedure. After that, the spectrum is rest-frame shifted using the redshift from optical spectroscopy so that the center of H I 21 cm line should be set to 0 km/s. Also the noise level of each spectrum is evaluated using *rms* of the spectrum outside of H I emission from the target galaxy ($-1000 < v$ [km s^{-1}] < -500 and $500 < v$ [km s^{-1}] < 1000, see Sec. 3.2). Because we eliminate the sources having one or more close companions, our sample can be free from the effect of the beam confusion (Jones et al., 2016).

By considering the possible correlations between H I gas properties, stellar mass, and the *SFR*, we aim to study the morphological dependence of H I gas properties *at fixed stellar mass and SFRs*. In the stacking process, we give a weight for each spectrum as $(1+z)^2/D_L(z)^2 M_*$ (see Sec. 3.3 in Fabello et al. 2011). If we stack the radio spectra without any weight, massive or nearby galaxies will significantly contribute to the resulting H I gas fraction ($F_{\rm HI}$). We also note that we perform stacking analysis only for the bins with a sample size of $\geq$10.

After subtracting the baseline of a stacked spectrum by linear fitting, we calculate the average gas fraction in each bin by summing up the flux in the velocity range of $-350 < v$ [km s^{-1}] < 350 (dashed lines in Figure 3.1). This velocity range is determined to cover the broadest emission line after the stacking process to be performed in Sec. 3.2. Adopting a fixed velocity range may lead to an increase in the error of $F_{\rm H_I}$ measurements. However, we decided to adopt this fixed velocity range for all the stacked spectra to estimate the errors and upper limits for H I undetected sources in a consistent manner. The flux error of each velocity component in a stacked spectrum is derived by propagating the *rms* from individual spectra before stacking (the light-green region in Figure 3.1). On the other hand, we adopt the Bootstrap resampling approach when calculating the average gas fractions to consider the sampling errors. In the following analyses, we use the average of gas fraction $F_{\rm HI}$ and its standard deviation from 1000 times Bootstrap resampling as the average gas fraction and its 1σ error. Here we note that the sampling error dominates the total error budget in our analyses.

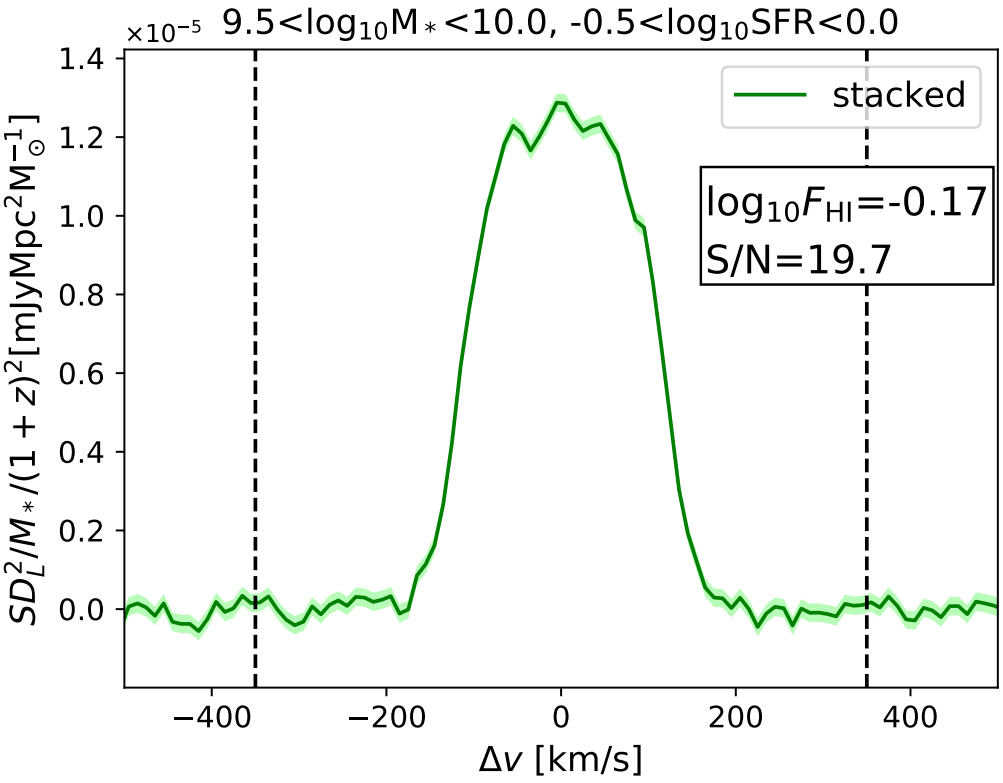

Figure 3.1: An example of the stacked H I spectra obtained in Sec. 3.1. The light-green region shows the error in each velocity bin derived from the *rms* of individual spectra. Vertical dashed lines are shown at ±350 km/s, between which the flux is summed up to calculate the gas fraction ($F_{\rm HI}$). We show the average gas fraction and S/N value calculated in our bootstrap analysis on upper right. Other spectra are summarized in Appendix A.1.

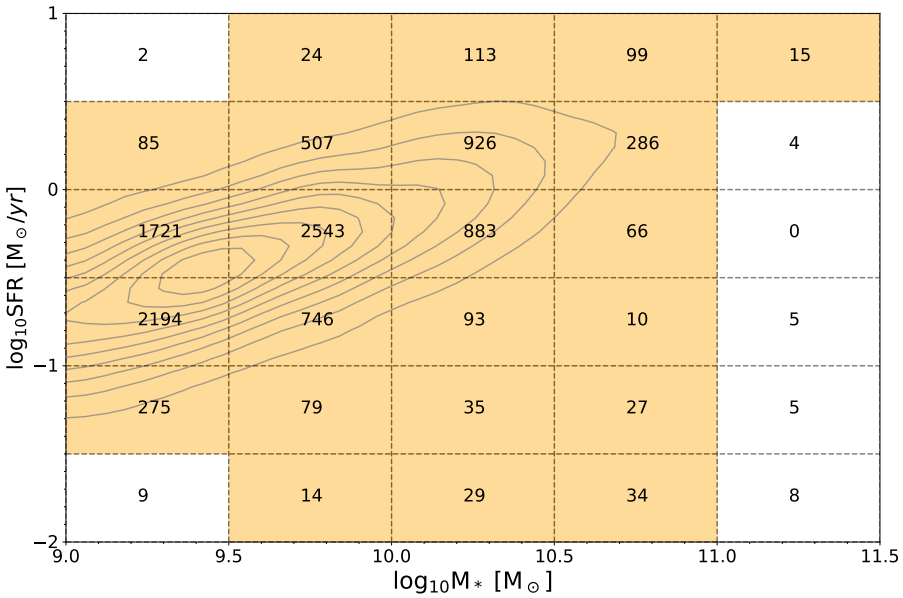

Figure 3.2: The M_*-SFR diagram to show the distribution of all our sample (grey contours) and the number of galaxies used for H I stacking at each (M_*, SFR) bin. The grid size indicates $\Delta M_* = \Delta SFR = 0.5$ dex (see Sec. 3.2 for details). Orange shaded bins are used for the stacking (N≥10).

3.2 Average H I gas fraction across the star-forming main sequence

Firstly, we simply divide our sample by the stellar mass and SFR ($\Delta M_* = \Delta SFR = 0.5$ dex), and carry out the stacking process as explained above. We summarize all stacked spectra in Appendix A.1. Figure 3.2 summarizes the number of galaxies included in each bin. The sample size tends to be small at high M_* and low SFR ends, and we do not perform H I stacking analyses for the bins with the sample size of $N < 10$. We note that the results presented in this thesis mainly focus on galaxies on the star-forming main sequence.

In Figure 3.3, the color-coding indicates the average gas fraction of galaxies at each stellar mass and SFR. Here we include the marginal detection down to $S/N = 3$. It can

be seen that the average gas fraction gradually changes with the stellar mass and the *SFR*. The increasing gas fraction with increasing *SFR* at fixed stellar mass seen in this diagram is consistent with a picture that the rich gas reservoir supports an active star-formation (Tumlinson et al., 2016).

In Figure 3.4, we show the relation between the gas fraction and stellar mass, with the color-coding based on the median *SFR* in each bin. The 3σ upper limits are represented by the triangles and arrows. It is clear from Figure 3.4 that there is a strong correlation between H I gas fraction and stellar mass, consistent with previous studies. The black squares connected by the solid line in Figure 3.4 show the H I gas scaling relation derived by Brown et al. (2015). Our results are in good agreement with the black lines at $M_* < 10^{10.2} M_\odot$, while at the massive end, our results tend to show higher values than the average scaling relation determined by Brown et al. (2015). The distinction of $F_{\rm HI}$ in the massive side is not surprising because we performed the H I stacking analyses only for the bins with the sample size of $N \geq 10$, and most of the bins below the star-formation main sequence are not used in this study. Brown et al. (2015) suggested that star-forming galaxies tend to host more H I gas than quenched galaxies, which can explain the difference between Brown et al. (2015) and our results at $M_* > 10^{10.2} M_\odot$. We emphasize that our stacking analysis shows an excellent agreement with Brown et al. (2015) when we use all SDSS galaxies at each stellar mass bin without considering the *SFR* binning (magenta stars in Figure 3.4).

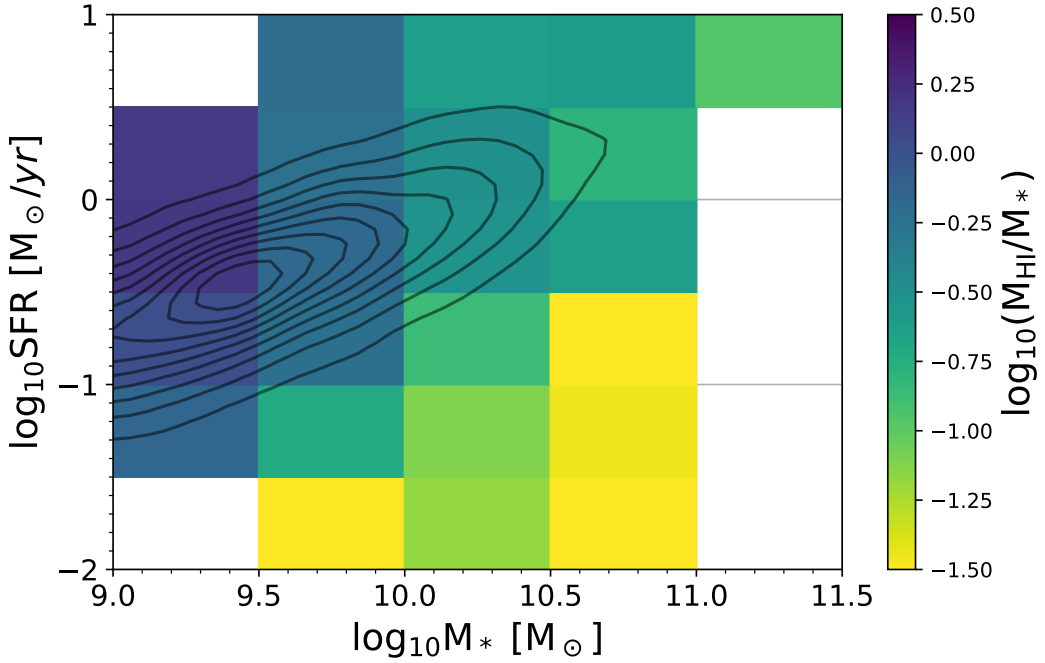

Figure 3.3: The average gas fraction (see color bar) at each position on the stellar mass vs. SFR plane from our ALFALFA stacking analysis. This panel includes the marginal detection ($S/N < 3$). The gas fraction depends both on the stellar mass and *SFR*. The black contours show the distribution of the parent 'star-forming' galaxies.

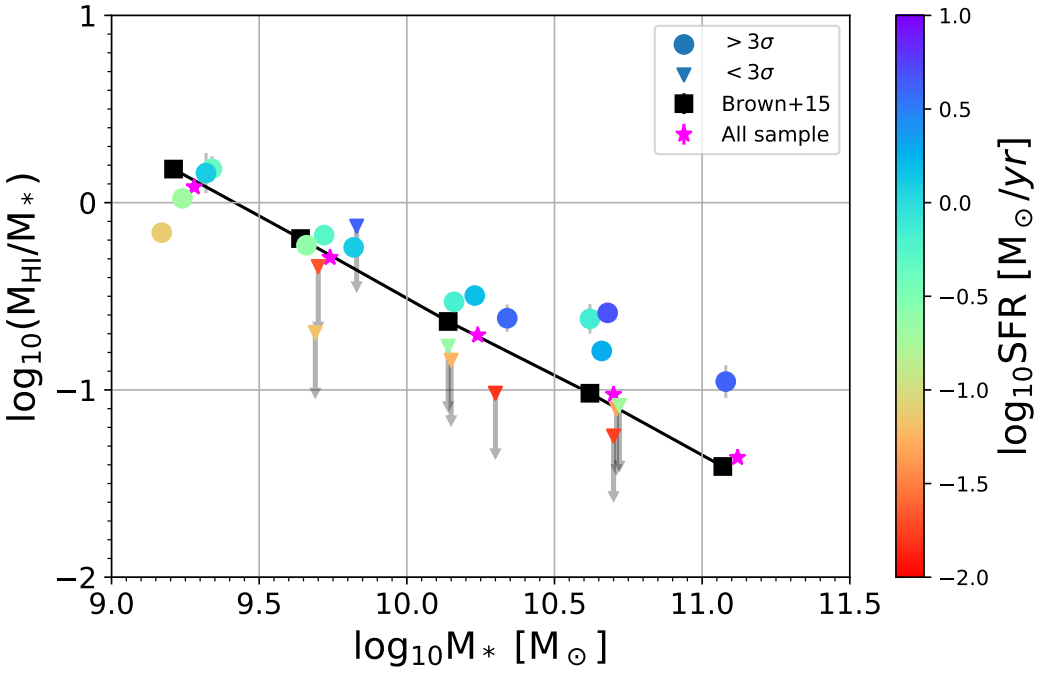

Figure 3.4: The gas fraction plotted against stellar mass. The color-coding of this plot shows the median *SFR* of each bin. Circles are the points with $S/N > 3$, and inverted triangles mean the 3σ upper limit. The magenta stars show the stacking result for all local galaxies by simply dividing our sample into five stellar mass bins (without considering *SFR* difference). Here, we include the galaxies having the potential companion within four arcmins to set the same selection criteria to Brown et al. (2015). The gray error bars are derived from the Bootstrap method (Sec. 3.1). We show the M_*–$F_{\rm H_I}$ scaling relation derived by Brown et al. (2015) as the black squares connected by the solid black line.

4

Morphological dependence of H I gas fraction at fixed M_* and SFR

The primary goal of this study is to investigate the *morphological* dependence of the H I gas fraction of our sample *at fixed stellar mass and SFR*. Here we use three morphological indicators of galaxies; Sérsic n, concentration index (C-index), and visual smoothness from the Galaxy Zoo 2 project (GZ2, Lintott et al. 2008; Willett et al. 2013; Hart et al. 2016).

The Sérsic profile can reproduce the classical surface brightness distribution of early-type galaxies (the de Vaucouleurs profile) when $n \sim 4$, and the exponential disk profile of late-type galaxies when $n = 1$. The C-index is often defined as the ratio of the half-light radii R_{50} and R_{90}, where R_x means the radius enclosing x % of the total flux. It is shown that the C-index has a strong correlation with the dominance of the bulge component in galaxies (e.g., Shimasaku et al. 2001). We also introduce the "visual smoothness" from GZ2 as a proxy for the traditional visual classifications made by human eyes (see Sec. 4.3 for more details).

We cross-matched our sample constructed in Sec.3.2 with the New York University Value-Added Catalog (NYU-VAGC; Blanton et al. 2005) and the full GZ2 catalog (Hart et al., 2016). NYU-VAGC contains multiband photometric information for 343,568 spectroscopically identified sources. Blanton et al. (2005) collected multiband information for objects in NYU-VAGC from the Faint Images of the Radio Sky at Twenty-Centimeters survey (Becker et al., 1995), the Two Micron All Sky Survey (Skrutskie et al., 2006), the Two-degree Field Galaxy Redshift Survey (Folkes et al., 1999), the Infrared Astronomical Satellite Point Source Catalog Redshift Survey (Saunders et al., 2000), and Third Reference Catalogue of Bright Galaxies (de Vaucouleurs et al., 1991). Galaxy catalog by Hart et al. (2016) contains the updated morphological information for 239,695 galaxies in GZ2. Our new cross-matched catalog contains 7712 objects, all of which have measurements of M_*, *SFR*, redshift, ALFALFA radio spectra, Sérsic n, C-index, and visual smoothness (see Table 4.1). We discuss the morphological impacts on the M_*–$F_{\rm HI}$ relation with this new sample in the following sections.

Properties	Catalog	Method & Data
M_*	GSWLC2	SED+LIR fitting
SFR	GSWLC2	SED+LIR fitting
redshift	MPA-JHU	optical spectroscopy
H I 21 cm line	ALFALFA survey	radio spectroscopy
Sérsic n	NYU-VAGC	Sérsic fits
C-index	NYU-VAGC	photometry (petrosian radius)
Visual smoothness	GZ2	votes by citizen scientists

Table 4.1: Parameters of galaxies in our cross-matched catalog and the source of information.

4.1 Sérsic index

Blanton et al. (2005) conducted the Sérsic fits for SDSS images of each objects. Sérsic index n is often considered as a morphological indicator (see Sec. 1.1), and we use n measured in the r-band to distinguish early-type and late-type galaxies.

We select 498 early-type and 2856 late-type galaxies by applying $n > 3.5$ and $n < 1.5$, respectively (cf., de Vaucouleurs's law and exponential profile, see Sec.1.1). Red and blue contours in Figure 4.1 show the distribution of early-type and late-type galaxies

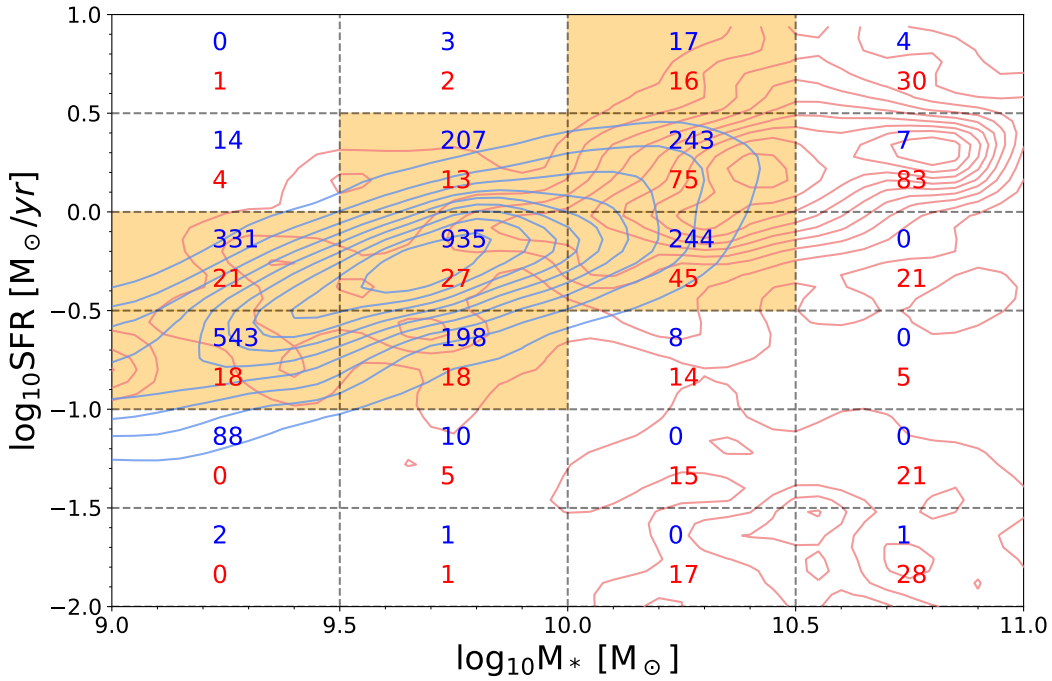

Figure 4.1: Same figure as Figure 3.2 but for late-type (blue) and early-type (red) galaxies divided by the Sérsic n. Blue and red contours show the distribution of late-type and early-type galaxies on this plane, respectively. Here we normalize the contours based on the total number of each population. The width of the grid is $\Delta M_* = \Delta SFR = 0.5$ dex. Here we show the region of $9.0 < \log_{10} M_* < 11.0$ and $-2.0 < \log_{10} SFR < 1.0$ because all other bins have sample sizes of $N < 10$. Orange shaded bins are used for the comparison of $F_{\rm HI}$ in panel (c) of Figure 4.2 ($N \geq 10$ for both populations).

on the M_*-SFR diagram. Here we normalize the contours based on the total number of each population. Because we mainly focus on the galaxies on the star-formation main sequence, the number of late-type galaxies is larger than that of early-type galaxies.

We then conducted the stacking analysis to the early/late-type subsamples in the same way as described in Sec.3.2. Here we use the same bin size for stacking as that in Sec.3.2 ($\Delta M_* = \Delta SFR = 0.5$ dex). The number of early/late-type galaxies in each bin is shown in Figure 4.1. We show all stacked spectra in Appendix A.2.

The left column in Figure 4.2 show the result. Panel (a) and (b) in Figure 4.2 show the relationship between the median stellar mass and the average H I gas fraction when we divide our sample into late-type and early-type by the Sérsic n. As we did in Figure 3.3, we use the bins with $N \geq 10$ for each morphological type. The general

trend does not change from Figure 3.4; the H I gas fraction is anticorrelated with the stellar mass and correlated with the *SFR*.

We compute the difference of H I gas mass between early-type and late-type galaxies with the same stellar mass and *SFR*, and they are plotted in Figure 4.2 (c) as a function of stellar mass. This comparison is performed for the bins in which both populations have more than nine galaxies in Figure 4.1. Here we note that there are two classes of bin types in terms of the H I detection.

1. Both populations have $S/N > 3$ ($\circ$ in Figure 4.2).

2. The $F_{\rm HI}$ of late-type/disk/non-smooth galaxies show $S/N > 3$ while early-type/bulge/smooth galaxies show $S/N < 3$ ($\triangle$ in Figure 4.2),

where disk/bulge and smooth/non-smooth are the morphological population intoruduced in Sec. 4.2 and Sec. 4.3. There are no bins with properties opposite to class 2 for all morphological indicators. In Figure 4.2 (c), we use large circles and normal triangles for the class 1 and 2, respectively. The number of bins in each class are summarized in Table 4.2.

Unfortunately, there are only two bins in class 1, and the remaining bins are class 2 or non-detection ($S/N < 3$). The $F_{\rm HI}$ differences in these two class 1 bins are $-0.09^{\pm 0.10}$ and $0.07^{\pm 0.09}$, suggesting that there is no significant difference in the H I gas mass between late-type and early-type galaxies at fixed M_* and *SFR* in those bins. Outside of these two bins ($\log_{10} M_* < 10.0$ or $\log_{10} M_* > 10.5$), we could not detect H I in the stacked spectra due to the poor statistics, especially for early-type galaxies.

We also conduct the same analysis with the different Sérsic n criteria. Here early/late-type galaxies are defined as those sitting in the top/bottom 20% profile in the distribution of Sérsic n; i.e. $n < 1.25$ for late-types and $n > 2.30$ for early-types. This method enables us to match the total size of subsamples and increase the number of bins in class 1. In the range of $9.5 < \log_{10} M_* < 10.5$ and $-0.5 < \log_{10} SFR < 0.5$, we find that there is no significant difference in the H I gas mass between early- and late-type galaxies. Using this method, however, early-type subsample can include contaminants from "intermediate" morphology ($n \sim 2-3$). It is, therefore, difficult to conclude there is no difference in H I gas mass fraction between early-type and late-type galaxies at fixed stellar mass and *SFR* with this percentile approach.

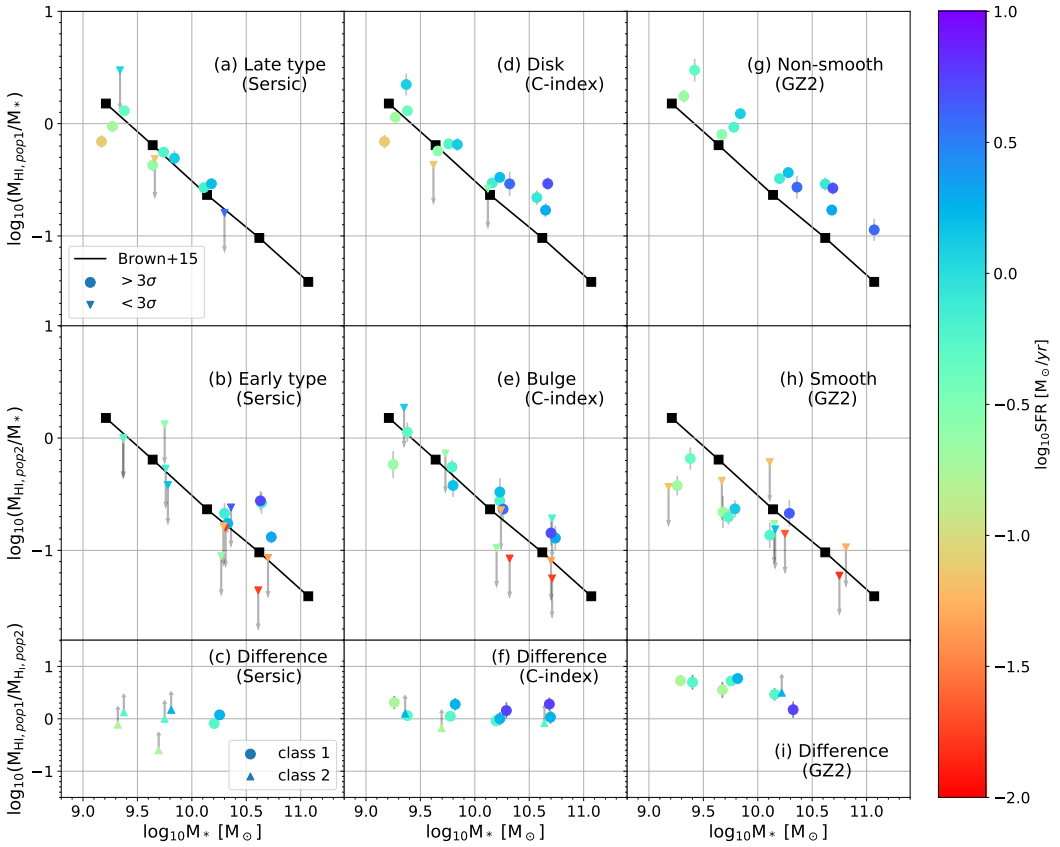

Figure 4.2: The result of our stacking analysis when we divide our sample by Sérsic n (left), C-index (middle), and visual smoothness (right). The top panels (a)/(d)/(g) show the relation between the stellar mass and the average H I gas fraction of late-type/disk/non-smooth populations, respectively. The second row (b)/(e)/(h) is the same as the upper panels but for early-type/bulge/smooth galaxies. The meanings of the large circles and inverted triangles in the top and second row are the same as Figure 3.4. The panels (c)/(f)/(i) show the difference in the amount of H I gas between the above two populations as a function of their stellar mass. The meaning of each symbol is summarized in Sec. 4.1. Colors indicate the median *SFR* of each subsample. The gray error bars are also derived by the Bootstrap method (see Sec.3.1). The black squares connected by the solid line show the scaling relation from Brown et al. (2015) (same as Figure 3.4).

	class 1	class 2
$S/N_{\rm pop.1}(F_{\rm HI})$	> 3	> 3
$S/N_{\rm pop.2}(F_{\rm HI})$	> 3	< 3
Sérsic n	2	5
C-index	9	3
Visual smoothness	7	1

Table 4.2: The "class 1" means that H I is detected at $S/N > 3$ for both of the populations in that bin. The "class 2" indicates the case where the first population shows $S/N(F_{\rm HI}) > 3$, while the second population has $S/N(F_{\rm HI}) < 3$. There are no bins with the properties opposite to those of class 2. In the lower row, we show the number of bins for each class and each morphological index. The class 1 and 2 are shown as circles and triangles in the bottom panels of Figure 4.2, respectively.

4.2 Concentration index

We also retrieve the r-band Petrosian half-light radii R_{50} and R_{90} from the NYU-VAGC catalog, and calculate C-index as a ratio of these two values (R_{90}/R_{50}). While the criteria of C-index used for the morphological classification are different from study to study (e.g., Deng 2013; Koyama et al. 2019), we adopt $C > 2.8$ and $C < 2.5$ for bulge-dominated and disk-dominated galaxies, respectively. We obtain 660 bulge and 5020 disk galaxies in total. Figure 4.3 shows the M_*-*SFR* diagram for bulge/disk galaxies. Binning width is the same as that in Sec. 4.1 ($\Delta M_* = \Delta SFR = 0.5$ dex), and the number of galaxies in each bin is also summarized in Figure 4.3. All stacked spectra in this section are in Appendix A.3.

The middle column of Figure 4.2 shows the results of our H I stacking analysis when we use C-index for morphological classification. The panels (d) and (e) in Figure 4.2 show the scaling relation for disk- and bulge-dominated galaxies. In panel (f), we show the difference between the disk and bulge samples by computing $M_{\rm HI,Disk}/M_{\rm HI,Bulge}$ at each stellar mass and *SFR*. The meanings of the symbols are the same as those in panel (c). The weighted average of $\log_{10}(M_{\rm HI,Disk}/M_{\rm HI,Bulge})$ of the "class 1" bins ($S/N(F_{\rm HI}) > 3$ for both bulge and disk populations) is 0.09 ± 0.10, suggesting that disk galaxies and bulge galaxies at fixed stellar mass and SFR have similar amount of H I gas on the star-formation main sequence ($9.0 < \log_{10} M_* < 11.0$). We verify that our results are unchanged even if we use the upper/lower 20 percentile in the distribution of the C-index to select bulge and disk populations ($C > 2.59$ and $C < 2.07$).

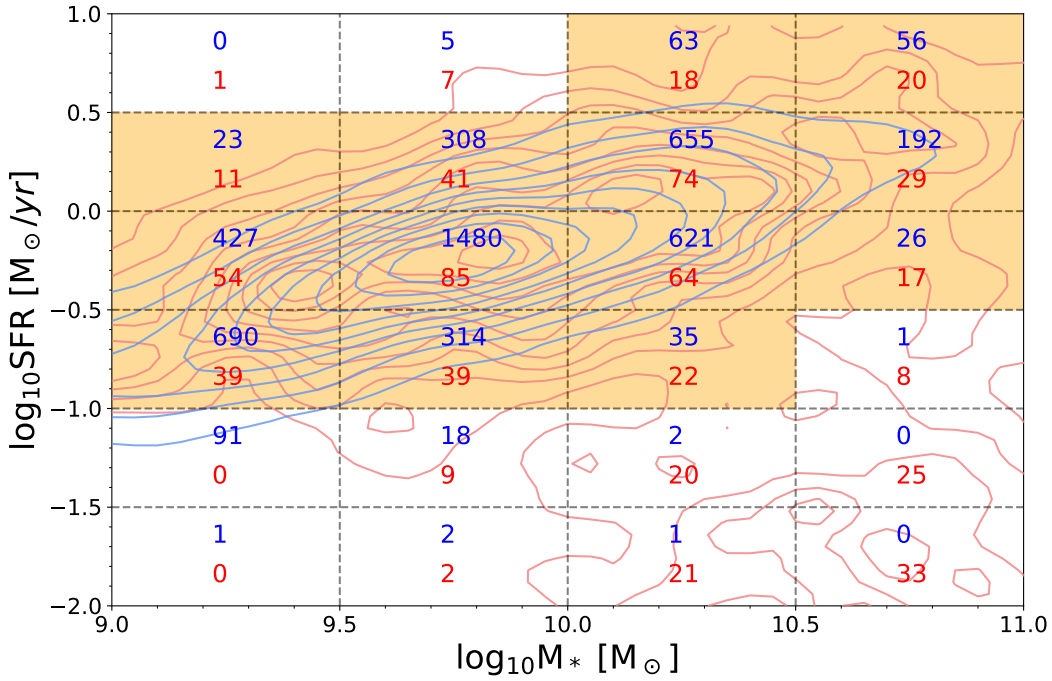

Figure 4.3: Same figure as Figure 4.1 but for disk (blue) and bulge (red) galaxies divided by the C-index.

4.3 Visual classification with GZ2

Galaxy Zoo project (Lintott et al., 2008) provides *visual* classifications of morphologies given by *citizen* scientists for a large number of galaxies observed in SDSS. In the Galaxy Zoo project, citizen scientists are asked to inspect galaxies' images and choose their morphological class (e.g., elliptical, clock-wise spiral). The result of Galaxy Zoo has been utilized to study the relationship between the galaxy morphology and other parameters like luminosity, color, environment, and star-forming activity (e.g., Bamford et al. 2009a; Bernardi et al. 2010; Schawinski et al. 2014).

Following Galaxy Zoo, Galaxy Zoo 2 project (GZ2, Willett et al. 2013) aims to describe more detailed morphological properties using a similar method to that of Galaxy Zoo. We here focus on the first question of GZ2: *"Is the galaxy simply smooth and rounded, with no sign of a disk?"*. All participants of the GZ2 project are asked to choose one answer from "Smooth and rounded", "Features or disk", or "Star or artifact". Then, GZ2 calculates the "vote fraction" for each answer. Willett et al. (2013) mentioned that for most of *clean* spirals in Galaxy Zoo, the vote fraction for "Features or disk" in GZ2 is similar to that for spiral galaxies in Galaxy Zoo.

Hart et al. (2016) revised the vote fraction with the idea that the actual distribution of the vote fraction should be independent of the redshift in the local universe. They remove the effect of size, luminosity, and redshift of galaxies and introduce the *debiased* vote fraction. Both original vote fraction in Willett et al. (2013) and the *debiased* vote fraction by Hart et al. (2016) are used as reliable indicator of galaxy morphology (e.g., Smethurst et al. 2017; Hart et al. 2017; Goulding et al. 2017; Masters et al. 2019; Domínguez Sánchez et al. 2018).

Following the recommendation by the GZ2 project, we use this *debiased* vote fraction from Hart et al. (2016) in this thesis, rather than directly using the original vote fraction provided by Willett et al. (2013). Galaxy catalog by Hart et al. (2016) contains 239,695 galaxies in total and secures enough number of galaxies statistically even after dividing them into small M_* and *SFR* bins. We define "smooth" galaxies as those having the debiased vote fraction of > 0.8 for "Smooth and rounded" in GZ2. On the other hand, we define "non-smooth" galaxies as those with the debiased vote fraction of > 0.8 for "Features or disk". Here we follow the recommendation by Willett et al. (2013) to use the criteria of the debiased vote fraction > 0.8 when performing any

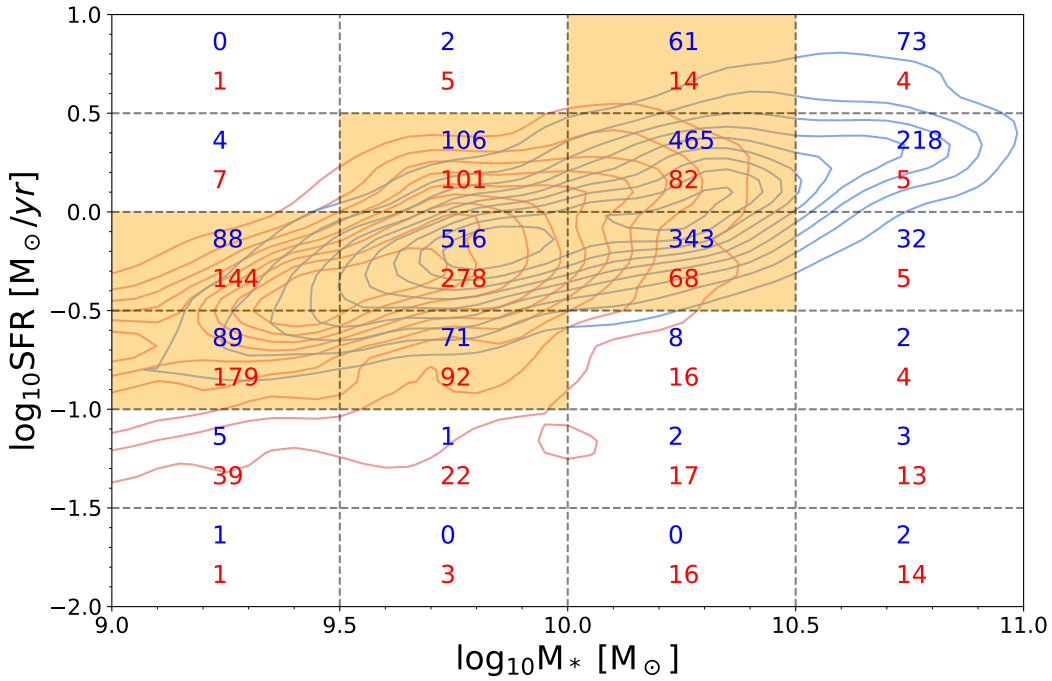

Figure 4.4: Same figure as Figure 4.1 but for non-smooth (blue) and smooth (red) galaxies divided by the visual smoothness.

morphological classification with GZ2. The bin size for our H I stacking analyses is the same as that in Sec 4.1 ($\Delta M_* = \Delta SFR = 0.5$ dex), and Figure 4.4 shows the number of galaxies in each bin. We summarize all stacked spectra in this section in Appendix A.4.

The result is shown in the right column of Figure 4.2. As we performed for Sérsic index and C-index in the previous sections, we show in panels (g) and (h) the scaling relation for non-smooth and smooth galaxies, respectively. Panel (i) shows the difference between these two populations at fixed M_* and SFR. Interestingly, smooth galaxies tend to have significantly lower gas fractions than non-smooth galaxies, and we find that there are six bins where both non-smooth and smooth galaxies are detected at $S/N(F_{\rm HI}) > 3$ (class 1). The weighted average of $\log_{10}(M_{\rm HI,Non-smooth}/M_{\rm HI,Smooth})$ is 0.71 ± 0.11, suggesting a significant difference in H I gas fraction between the smooth and non-smooth galaxies at fixed stellar mass and SFR in the range of $9.0 < \log_{10} M_* < 10.5$. We find no bin where H I is detected only for smooth galaxies. This result is also unchanged even if we use the percentile approach, in which we define smooth and non-smooth as the top and bottom 20% along the debiased vote fraction for "Features

or disk".

5 Discussion

The morphological dependence of the H I gas mass in local galaxies has been discussed for decades (e.g., Roberts & Haynes 1994). The H I gas mass is known to depend on the stellar mass and the *SFR* of host galaxies (e.g., Brown et al. 2015). On the other hand, the morphology of galaxies is also related to the stellar mass and the *SFR* (e.g., Kauffmann et al. 2003). These relationships between multiple parameters make it difficult to understand the real impact of galaxy morphologies on their H I gas mass content.

In our study, we divide our sample into small bins on the M_*-*SFR* plane ($\Delta M_* = \Delta SFR = 0.5$ dex). The galaxies in each bin are further divided by their morphology with three morphological indicators; Sérsic n, C-index, and the visual smoothness. Our study revealed that *visually* smooth galaxies have lower gas fractions than non-smooth galaxies at fixed stellar mass and SFR. Such a morphological trend is not observed when we use C-index (Figure 4.2). Below, we will discuss the potential candidates which may affect the H I gas content of galaxies and why we see morphological dependence only when we use *visual smoothness*.

5.1 Stellar mass, *SFR*, and environment

When investigating the effect of galaxy morphology on the H I gas mass, it is crucial to exclude the impact of other properties of galaxies. Many previous papers show that H I gas mass strongly depends on the stellar mass of host galaxies (M_*-M_{HI} scaling relation, e.g., Fabello et al. 2011; Brown et al. 2015; Healy et al. 2019). A simple approach to remove the stellar mass dependence is to check the H I scaling relations of each subsample. Calette et al. (2018) compared the H I scaling relation of late-type galaxies and early-type galaxies and concluded that late-type galaxies have higher H I gas fraction than early-type galaxies at all stellar mass ranges. However, the stellar mass is not the only parameter that determines the H I gas mass of the host galaxies, and other parameters can also affect the scaling relation (Cortese et al., 2011; Brown et al., 2015; Cook et al., 2019). For example, Cook et al. (2019) studied the impact of the bulge-to-total mass ratio on the H I scaling relation and found no significant effect of the morphology when they limited their sample to the star-forming galaxies. They argue that the morphological dependence of H I scaling relation reported in previous studies originates from the correlation between the star-formation activity and galaxy morphology at fixed stellar mass. On the other hand, the amount of molecular hydrogen in the star-forming galaxy is shown to be approximately fixed in a wide range of bulge-to-total mass ratio, whereas that of H I can change by a factor of 100 (see Figure 10 in Catinella et al. 2018). Morphological independence of molecular hydrogen is also supported by Koyama et al. (2019), who showed similar molecular gas mass fractions for green-valley galaxies with different morphologies (classified by C-index) at fixed stellar mass and *SFR*.

Because all the analyses presented in this work are performed at fixed stellar mass and *SFR*, our results should not be affected by different stellar masses or *SFR*s. There remains a possibility of a slight difference in the distribution of stellar mass and *SFR* *within* the small (M_*, SFR) bin. We calculate the median M_* and *SFR* for smooth and non-smooth galaxies in each bin (δM_* and δSFR), and confirm that the difference is very small for all the bins used in Figure 4.2 (i) ($\delta M_* \leq 0.08$, and $\delta SFR \leq 0.11$). By recalling Figure 3.4, the small difference existing in each bin cannot explain 0.71 dex difference in the gas fraction between smooth and non-smooth galaxies.

5.2 Environmental effect

Although we consider that the stellar mass and the star-formation activity are the primary parameters that determine the H I gas content of galaxies, their surrounding environments may also affect the H I scaling relation. Observations revealed that late-type galaxies in dense environments tend to have less H I gas than those in the general field (e.g., Haynes & Giovanelli 1984; Solanes 2001), likely due to environmental processes such as galaxy-galaxy interactions or ram pressure stripping (Moore et al., 1998; Gunn & Gott, 1972; Cortese et al., 2021). It is also true that early-type galaxies in the traditional Hubble sequence (ellipticals/S0s) tend to be located in cluster environments in the local universe (e.g., Dressler 1980, Bamford et al. 2009b).

To check the environment of smooth and non-smooth galaxies, we investigate the halo mass of smooth and non-smooth galaxies. By cross-matching our sample with the SDSS DR7 group catalog from Yang et al. (2007), we obtain the halo mass of galaxies. We then divide these galaxies into small bins of stellar mass and *SFR* as used for our stacking analysis ($\Delta M_* = \Delta SFR = 0.5$ dex), and carry out the Kolmogorov–Smirnov (KS) test on the halo mass distribution of two populations. We find that p-values are >0.05 for most of the bins, suggesting that we cannot rule out the null hypothesis that the two populations are drawn from the same parent population.

We also conducted the same analysis to the subsample of early-/late-type and bulge/disk galaxies. The result is almost the same; for most of the bins, p-values in the KS test are more than 0.05. Therefore, it is unlikely that our results shown in Figure 4.2 are affected by the dense environment (Figure 5.1). At the beginning of our analyses (see Sec. 2), we excluded galaxies having one or more companions within the ALFA beam size. Those galaxies with a close companion(s) tend to be located in a group/cluster environment with a large halo mass. We, therefore, caution that we are not suggesting that H I gas mass of galaxies is not affected by their surrounding environment with Figure 5.1.

We note again that the morphological difference in the H I gas fraction is visible only when we use *visual smoothness* for the morphological classification. We do not see the difference when we use C-index (Figure 4.2 (f)), consistent with the conclusion of Cook et al. (2019). A question here is—what is the *visual smoothness*? We will discuss this in Sec. 5.5, and attempt to identify reasons responsible for the different behavior

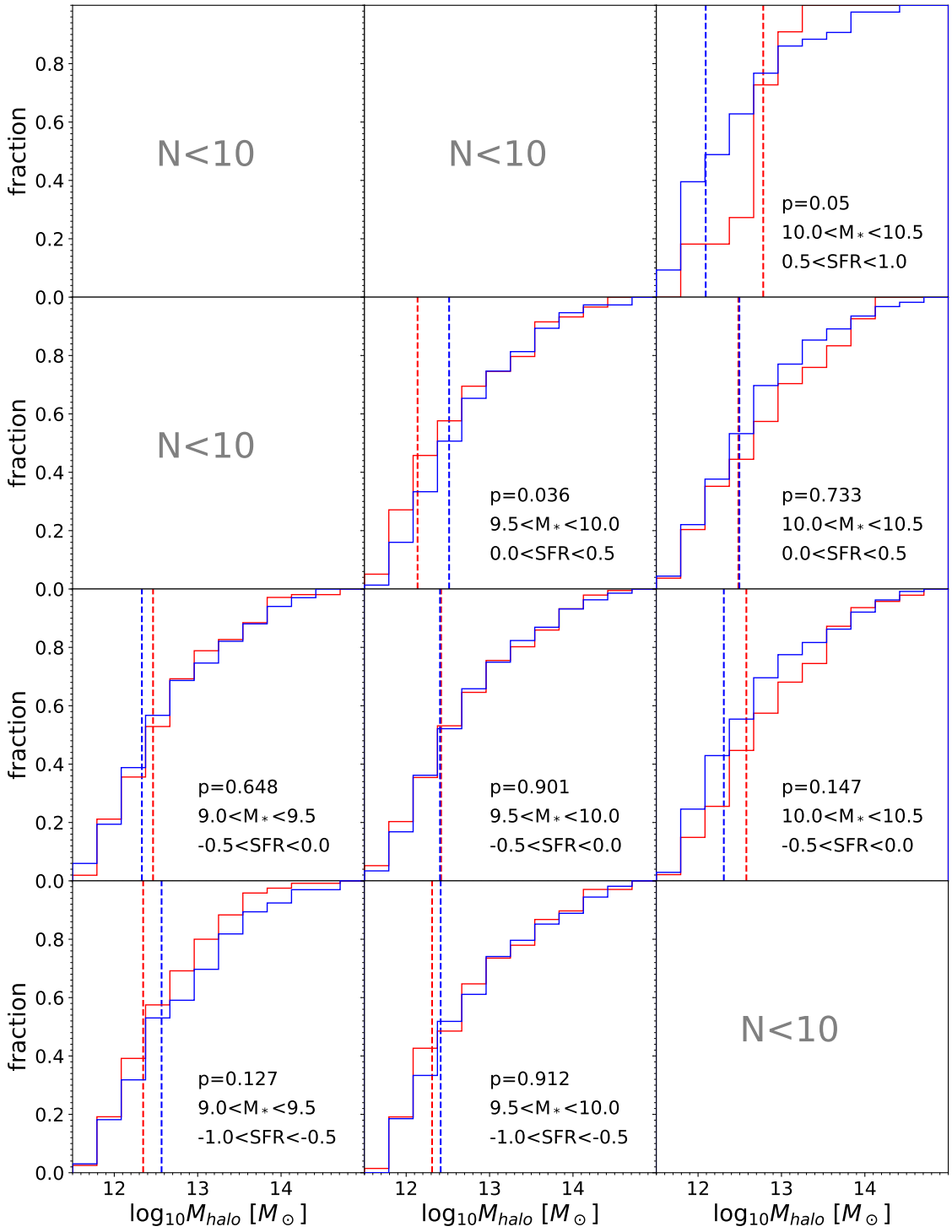

Figure 5.1: The cumulative halo mass distribution of our smooth (red) and non-smooth (blue) galaxies for each stellar mass and *SFR* bin. The median value of halo mass in each bin is plotted as dashed vertical lines. The p-value from the KS test is shown at the bottom right corner of each panel. We note that we request a minimum sample size of 10 for both smooth and non-smooth subsamples to compute the p-value. The panels with $\log_{10}(M_*/M_\odot) > 10.5$, $\log_{10}(SFR/M_\odot yr^{-1}) < -1.0$, or $\log_{10}(SFR/M_\odot yr^{-1}) > 1.0$ are not shown because none of the bins outside the plotted M*/SFR range satisfy the requirement of $N \geq 10$.

when we use *smoothness* as a morphological indicator.

5.3 Visual smoothness and other morphological indicators

We introduce the *visual smoothness* as a parameter describing the appearance of galaxies. In our analysis, smooth and non-smooth galaxies are determined by the debiased vote fraction of each answer to the first question in GZ2 (Willett et al., 2013), *"Is the galaxy simply smooth and rounded, with no sign of a disk?"* This unique classification distinguishes between H I-rich and H I-poor population at fixed M_* and SFR, but what determines the visual smoothness of galaxies? To interpret the visual smoothness, we investigate how the visual smoothness correlates with the other two morphological parameters used in this study (Sérsic n and C-index; see Figure 5.2).

From Figure 5.2, we realize that both smooth and non-smooth galaxies are distributed over a wide range in Sérsic n and C-index. The distribution of smooth galaxies has a peak around $n \sim 1$, corresponding to a pure exponential disk, and there are non-smooth galaxies at $n \sim 4$, which corresponds to the de Vaucouleurs profile. For C-index, smooth galaxies and non-smooth galaxies have a different distribution in the bottom panel of Figure 5.2, but the distribution of the smooth galaxies is peaked at $C \sim 2.5$, which is actually used to select "disk" galaxies in Sec.4.2. Figure 5.2 suggests that the visual smoothness judged by the citizen scientists is not simply identifying early/late-type or bulge/disk-like morphologies.

We also check the relationship between visual smoothness and other morphological indicators, Asymmetry index A, Clumpiness parameter S, Gini coefficient G, and the second-order moment parameter M_{20}. Asymmetry index A evaluates how asymmetric galaxy is after rotating 180° around its center. The intensity difference before and after the rotation can be calculated for each position on a galaxy image. We can calculate A by summing up the flux difference and removing the background effect (Abraham et al., 1996; Conselice et al., 2000; Conselice, 2003; Hernández-Toledo et al., 2008; Conselice, 2014; Pawlik et al., 2016). Clumpiness parameter S describes the fraction of light that does not follow the simple Gaussian profile. S is often defined as the normalized sum of the absolute value of residuals from Gaussian fitting for all pixels (Takamiya, 1999;

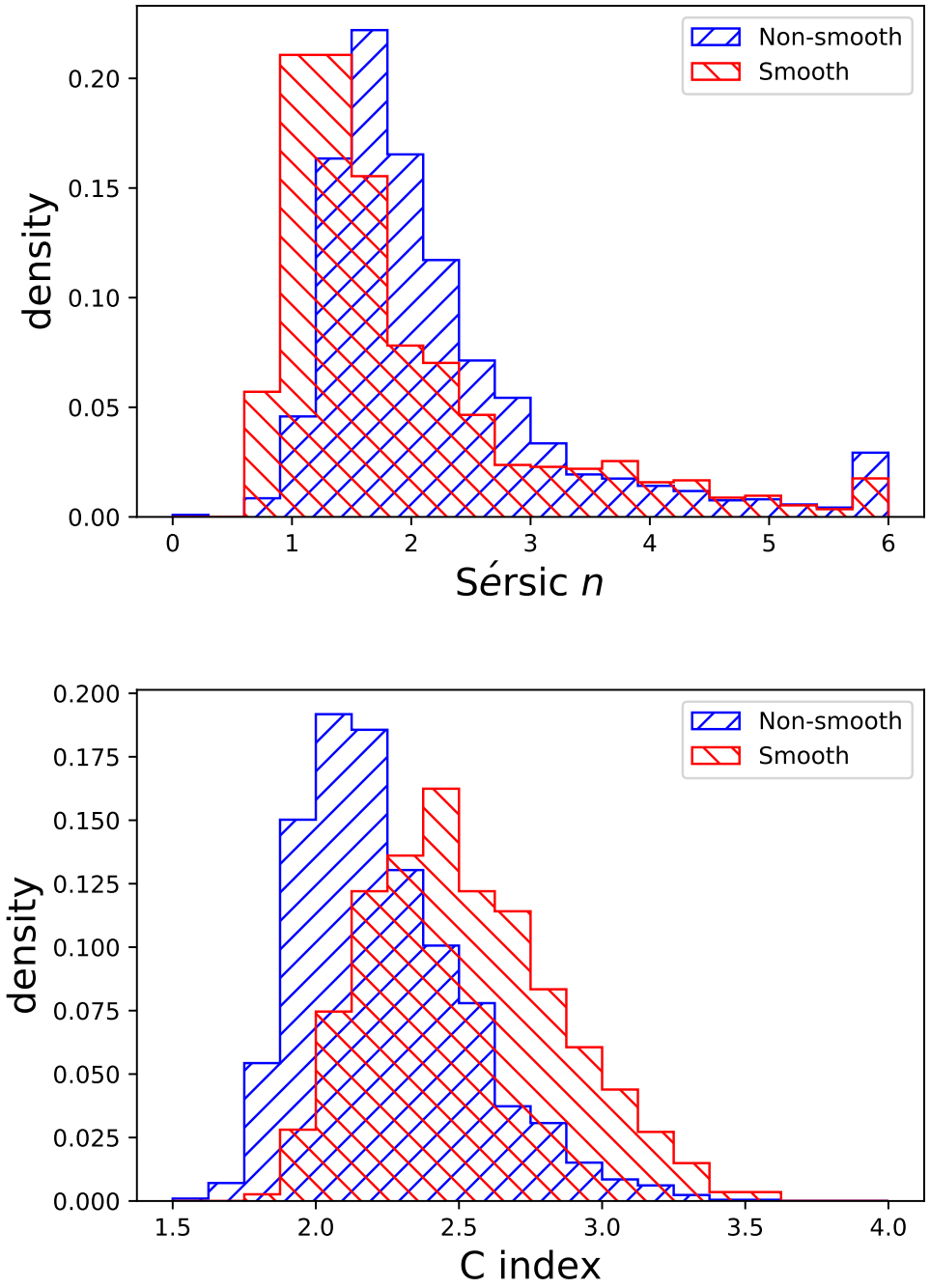

Figure 5.2: Number distribution of non-smooth (blue) and smooth (red) galaxies for Sérsic n (upper) and C-index (lower). We normalized the number distribution by the total number of each population.

Conselice, 2003, 2014; Pawlik et al., 2016). Conselice (2003) summarized the typical value of A and S along Hubble's Tuning fork. Gini coefficient G is sometimes used to visualize the wealth disparity in economics. In galactic astronomy, we first arrange the pixels in a galaxy from the lowest to the highest intensity. When we sum up the intensity from the lowest pixel, we can draw a curve between the number of summed pixels (x) and summed intensity (y). This curve should be $y = x$ if the light profile is flat. If we fix the total intensity and concentrate the light at several pixels, the middle of this curve will drop from $y = x$ ($y = f(x)$). When we write the area of the region surrounded by $y = x$ and $y = f(x)$ as S_1 and the integral of $f(x)$ as S_2, $G = S_1/(S_1 + S_2)$ (Abraham et al., 2003; Lotz et al., 2004, 2008b). Thus $G = 0$ for flat light profile and $G = 1$ in the case that all light concentrate in one pixel. The second-order moment parameter M_{20} is computed with the 20% brightest pixels and its distance from the intensity-weighted center (Lotz et al., 2004, 2008b). Negatively large M_{20} shows the light concentration, but it is not necessary to locate at the center of galaxies.

Because we do not have such information for our 'star-forming' sample, we use only galaxies included in the PawlikMorph catalog of SDSS DR16 (Ahumada, 2020). This catalog contains A, S, G, and M_{20} for 4,824 local galaxies targetted in Mapping Nearby Galaxies at APO (MaNGA; Bundy et al. 2014). Pawlik et al. (2016) measured those parameters with the SDSS DR7 images, which is also used in GZ2. We cross-match the PawlikMorph catalog and GZ2 catalog by Hart et al. (2016). Then we select 'star-forming' smooth and non-smooth in the same manner as Sec. 2.3 and 4.3.

Figure 5.3 and 5.4 show the distribution of smooth (red) and non-smooth (blue) galaxies in A, S, G, and M_{20}, respectively. We can see that smooth and non-smooth galaxies have similar A and S (Figure 5.3). On the other hand, Figure 5.4 suggest that G and M_{20} are different between smooth and non-smooth galaxies, which implies that non-smooth galaxies have more light-concentrated regions than smooth galaies have. Considering the similar A in the top panel of Figure 5.3, we can infer that non-smooth galaxies have small-scale sturcture in the disk region, such as spiral arms and star-forming clumps. Although S parameters can capture such a feature in principle, we cannot see the difference in the bottom panel of Figure 5.3. Conselice (2014) pointed out that G and M_{20} are free from the subtraction of background, which would affect the detection of faint structures.

We show examples of the optical images of our non-smooth and smooth galaxies

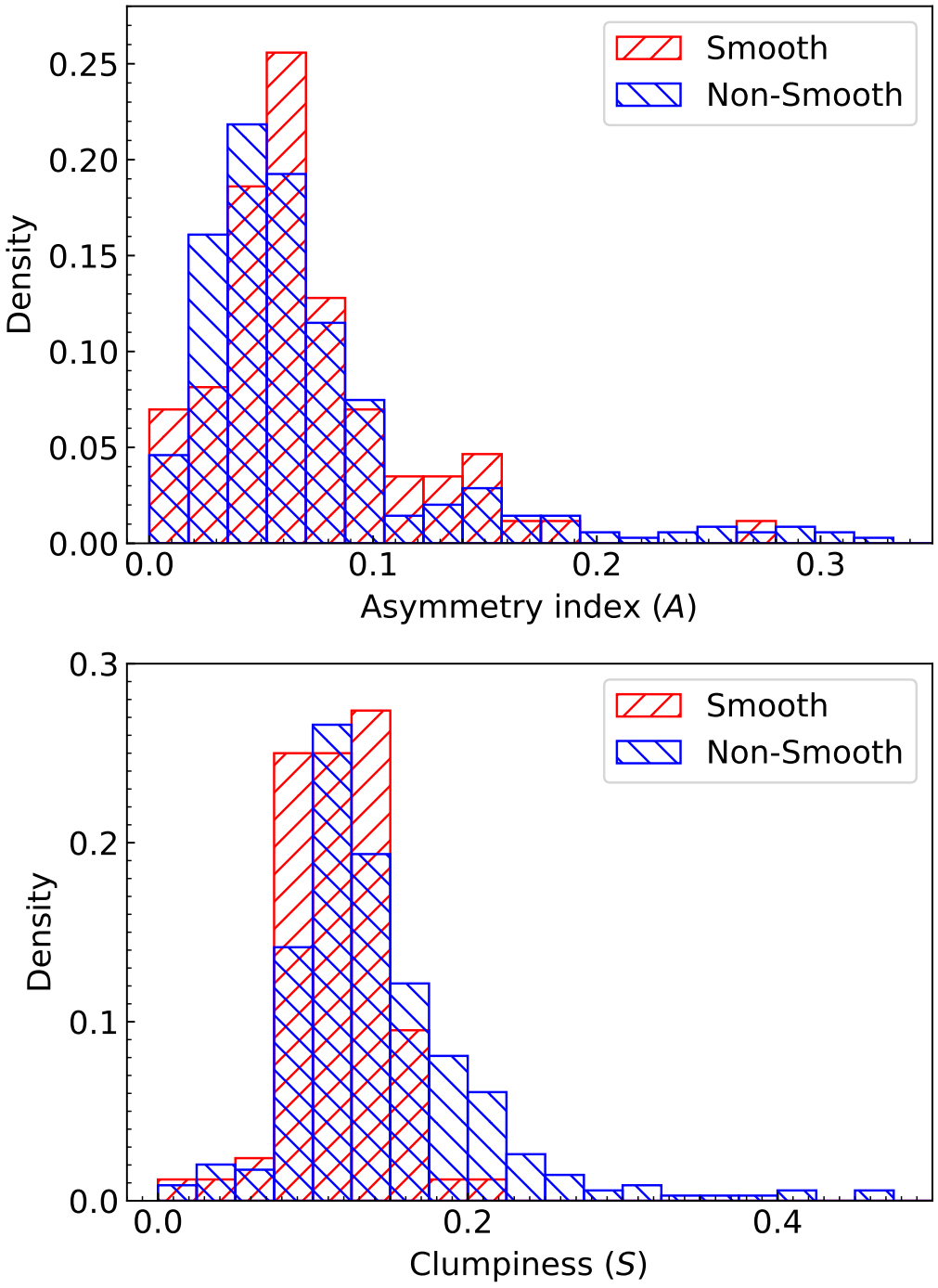

Figure 5.3: Number distribution of non-smooth and smooth galaxies for Asymmetry index A (top) and Clumpiness parameter C (bottom). Color and normalization is same as Figure 5.2.

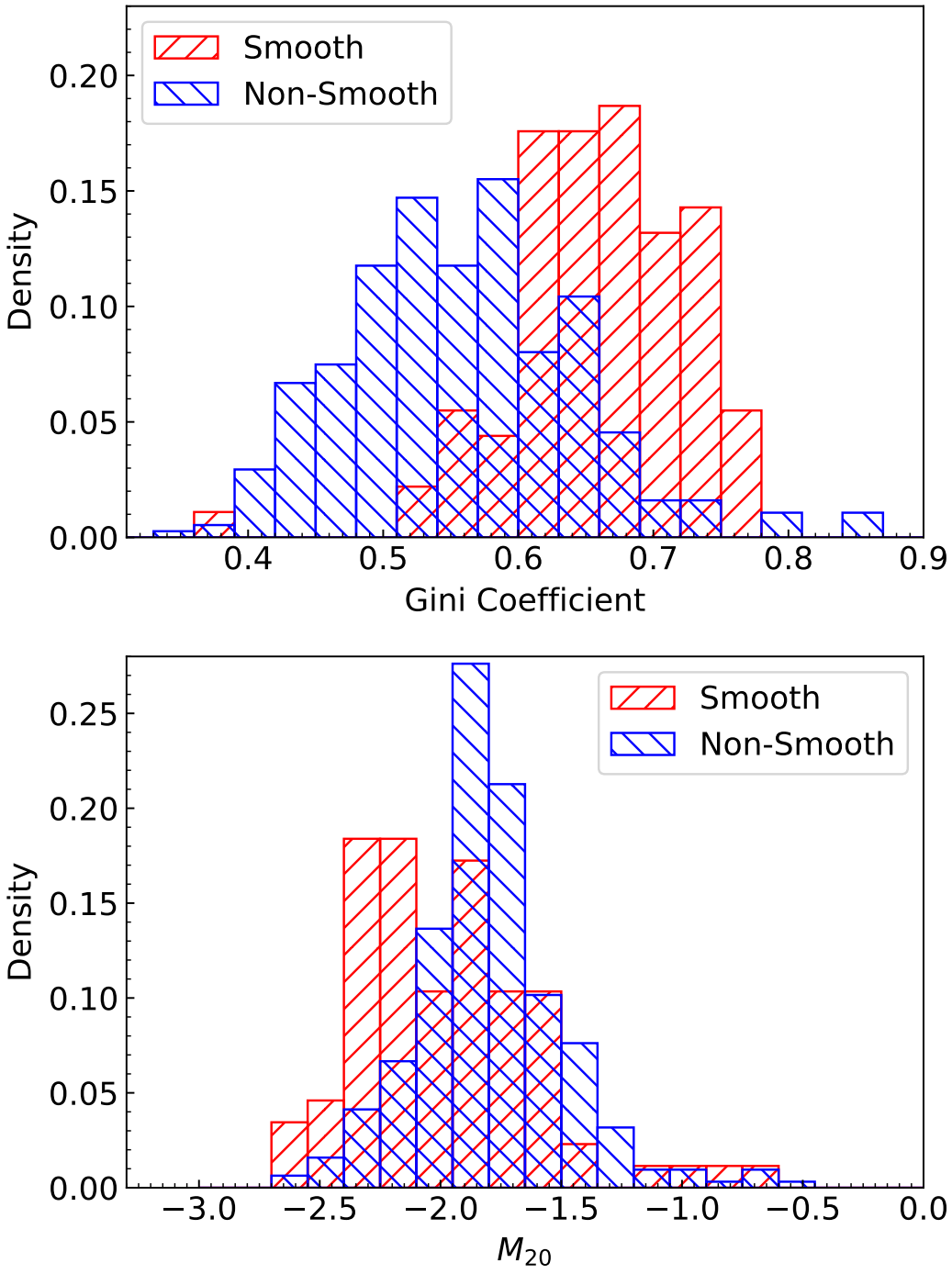

Figure 5.4: Number distribution of non-smooth and smooth galaxies for Gini coefficient G (top) and the second-order moment parameter M_{20} (bottom). Color and normalization is same as Figure 5.2.

from SDSS DR12 in Figure 5.5 and Figure 5.6. The stellar mass, *SFR*, Sérsic n, and C-index of these galaxies are fixed at $10.0 < \log_{10} M_* < 10.5$, $0.0 < \log_{10} SFR < 0.5$, $1.0 < n < 1.5$, and $2.0 < C < 2.5$. In other words, only visual smoothness is different between Figure 5.5 and Figure 5.6. By visually inspecting the optical images in Figure 5.5 and Figure 5.6, we realize that many of the smooth galaxies show prominent bulge and disk structure. It is likely that the citizen scientists' critical features to identify *non-smoothness* would be the small structures like spiral arms or prominent bar structures within the galaxies. Indeed, non-smooth galaxies in Figure 5.5 seem to have spiral arms or prominent bar structures, while smooth galaxies do not have such a small-scale structure. Our visual inspection is consistent to the result in Figure 5.3 and Figure 5.4. Although the Sérsic n and C-index are the morphological indicators commonly used to describe the overall light profile from the core to the outskirts of galaxies, it would not be possible to identify such small-scale structures by those automated parameters.

Our results suggest that galaxy morphologies defined by Sérsic n and C-index are not identical to the classification made by human eyes. We note that we are not discussing which is the best indicator of galaxy morphologies. We suggest that the visual smoothness can better distinguish gas-rich and gas-poor populations at fixed stellar mass and *SFR*. We should also note that our sample is limited to the local universe ($0.01 < z < 0.05$), so that the physical resolution is high (typically 0.94 kpc at $z = 0.033$). This might help citizen scientists to identify small structures in the galaxies.

5.4 Effect of redshift

It would also be essential to understand the effect (or bias) produced by the redshift of galaxies on the visual classification of the citizen scientists in GZ2. As shown in Figure 4 of Willett et al. (2013), the fraction of smooth galaxies increases with redshift, while the non-smooth population decreases. This trend is not surprising because the physical resolution becomes poorer for more distant galaxies, and thus it becomes more challenging to identify small-scale structures within more distant galaxies. Hart et al. (2016) corrected the vote fraction by removing the bias produced by the different redshifts. Because we use the debiased vote fraction derived by Hart et al. (2016), our results would not be affected by the redshift effects. Figure 5.7 shows the redshift

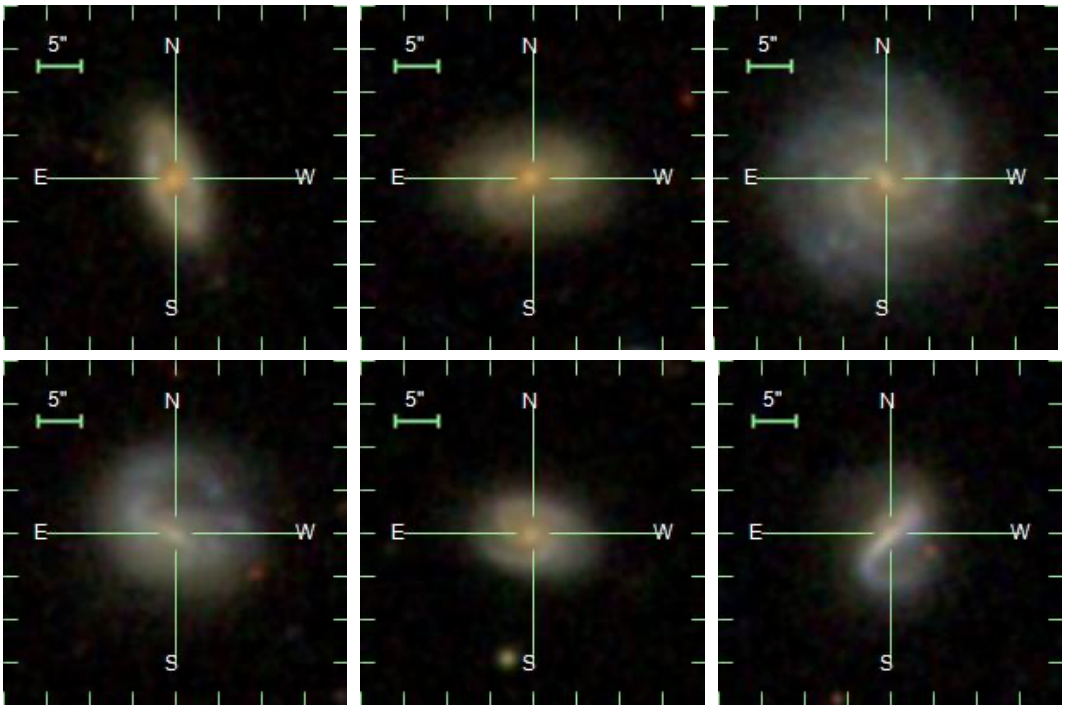

Figure 5.5: Examples of optical images of non-smooth galaxies from SDSS DR12. We note that all these galaxies listed here have fixed stellar mass, *SFR*, Sérsic n, and C-index ($10.0 < \log_{10} M_* < 10.5$, $0.0 < \log_{10} SFR < 0.5$, $1.0 < n < 1.5$, $2.0 < C < 2.5$).

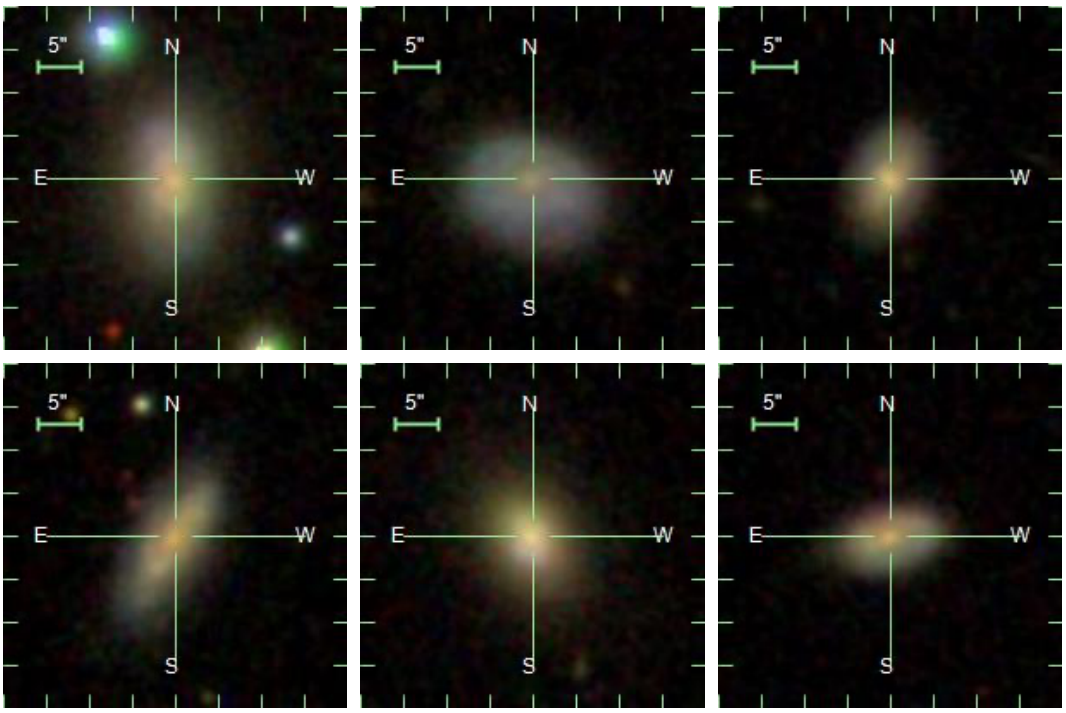

Figure 5.6: Examples of optical images of smooth galaxies from SDSS DR12. The ranges of stellar mass, *SFR*, Sérsic *n*, and C-index are the same to Figure 5.5

distributions of our smooth and non-smooth galaxies in each (M_*, SFR) bin. This plot suggests that smooth galaxies tend to have higher redshifts than non-smooth galaxies below the star-formation main sequence, while this trend is often reversed for galaxies located above the main sequence. The H I mass discrepancy between smooth and non-smooth galaxies reported in Figure 4.2 (i) is seen regardless of the stellar mass or *SFR* of galaxies. Therefore it is unlikely that the different redshift distribution within each (M_*, SFR) bin has significant impacts on the elevated H I mass excess in non-smooth galaxy population. In addition, even if redshift potentially affects our result, our smooth subsample will be contaminated by non-smooth and intermediate population, which makes the difference in Figure 4.2 (i) small.

5.5 Visual smoothness

Our results suggest that the existence of small-scale structures in the galaxies (e.g., spiral arms) would be the key to determining the H I gas fraction. These small-scale structures might be missed by the C-index and Sèrsic n because they are roughly tracing the overall light profile. In contrast, human eyes are more sensitive to such internal structures, and this would be the leading cause of the different morphological dependence of H I gas mass when we use C-index or visual smoothness for the morphological classification. Considering the fact that the amount of molecular hydrogen is almost constant (Catinella et al., 2018; Koyama et al., 2019), our result suggests that non-smooth galaxies have a more significant amount of H I that is not involved in the star-formation than smooth galaxies, even at the same stellar mass and *SFR*. More detailed theoretical approaches and observations of atomic gas kinematics within the galaxies are necessary to understand the missing link between the small structures likely caused by the local instability (e.g., Toomre 1977) and the global properties of H I gas in galaxies. It is expected that simulations will allow one to trace the motion of gaseous and stellar components within galaxies.

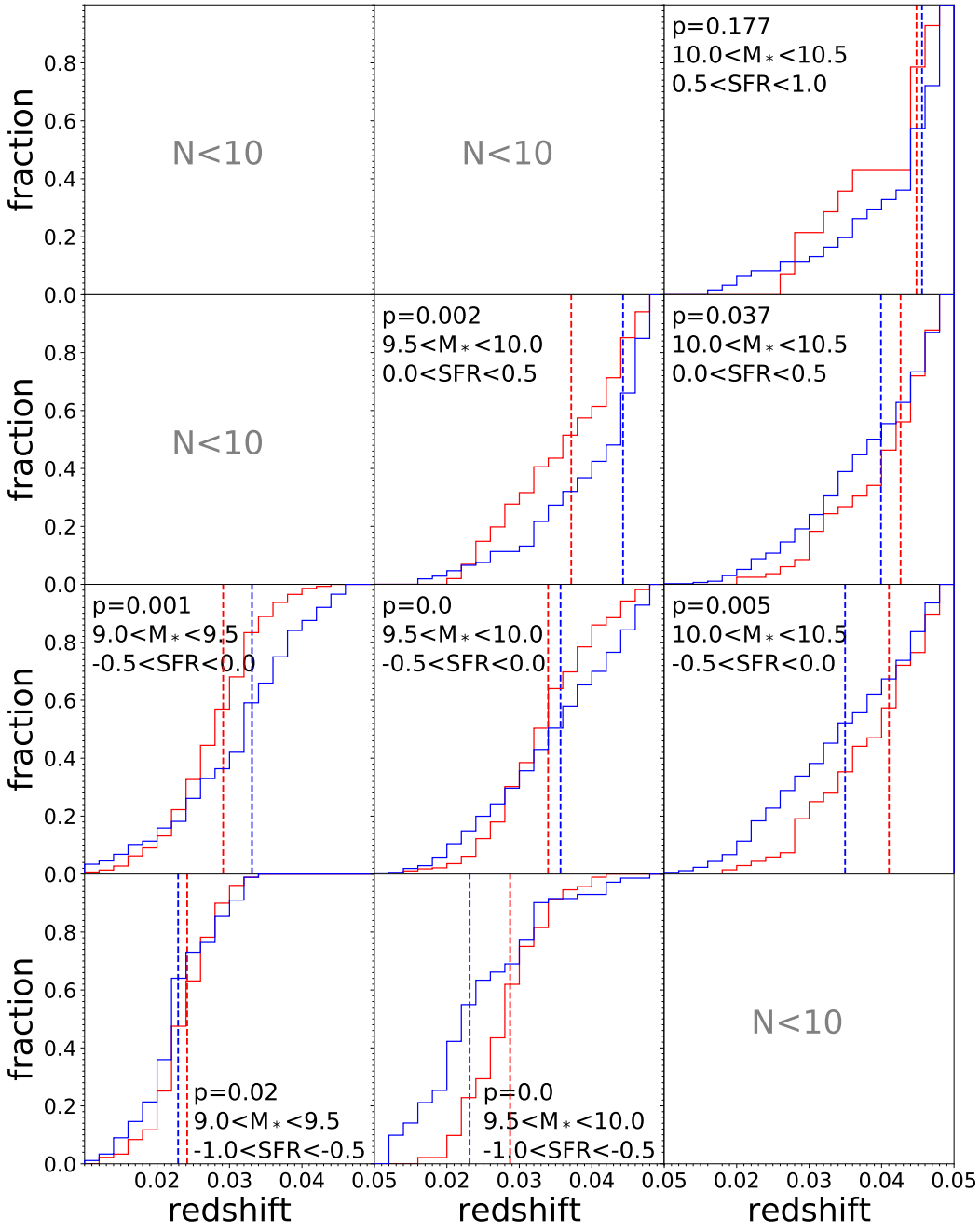

Figure 5.7: The cumulative redshift distribution of our non-smooth (blue) and smooth (red) galaxies for each stellar mass and *SFR* bin. The median value of the redshift in each bin is plotted as dashed vertical lines. The stellar mass range, *SFR* range (log scale), and the p-value from the KS test are shown in each panel. We note that we require a minimum sample size of 10 for both smooth and non-smooth galaxy subsamples to compute the p-value.

6 Interpretation with Illustris simulation

We finally discuss the background physics connecting the H I content of galaxy and its small-scale structure. Because we compared the smooth and non-smooth galaxies at the same M_* and *SFR*, the candidate of background physics should produce galaxies having the different $F_{\rm HI}$ and morphology with making the same M_* and *SFR* at $z = 0$. Here we introduce three possible scenarios which can explain the morphological impact on the $F_{\rm HI}$ of galaxies with satisfying the constraint about M_* and *SFR*.

6.1 Possible mechanisms

Firstly, we consider the gravitationally unstable disk. As Toomre (1964) discussed, losing a local balance between the self-gravity, thermal pressure, and disk rotation will lead to the formation of a giant clump structure. This condition of the unstable disk is often described by Toomre's Q parameter, $Q < 1$. In the case of thin and non-uniformly rotating disk, Q is calculated from the local gas velocity dispersion (σ), epicyclic frequency (κ), and gas surface density (Σ). Eq.6.1 shows the relation of those

parameters (Toomre, 1964; Larson, 1985; Binney & Tremaine, 1987, 2008; Escala & Larson, 2008).

$$Q_{gas} \propto \frac{\sigma\kappa}{\Sigma} \tag{6.1}$$

Suppose $Q < 1$, a gas disk can fall into the gravitational instability and start the clump formation. Based on Eq.6.1 and the condition of instability ($Q < 1$), we can consider that gas-rich turbulent disk with large Σ will easily reach the formation of giant star-forming region (Daddi et al., 2008; Tacconi et al., 2008). Therefore, the difference of $F_{\rm HI}$ in smooth and non-smooth galaxies in Figure 4.2 can be explained by the past gas-richness and gravitational instability.

Secondly, we introduce the effect of the merger. Mergers are known to trigger the bursty star-formation and change the morphology of galaxies, which has been pointed out from both observations (Schweizer, 1982; Lotz et al., 2008a,b) and numerical simulations (Mihos & Hernquist, 1996; Cox et al., 2006; Hayward et al., 2013). Therefore, the merger between two disk-dominant galaxies would create a bulge-dominant, spheroidal galaxy which has lost most of its gas (Toomre, 1977; Hopkins et al., 2008; Sparre et al., 2021), which can explain our morphology-$F_{\rm HI}$ relation.

Thirdly, we expect that the re-excitation of star-formation activity in the passive and smooth galaxy can reproduce our result in Figure 4.2 (rejuvenation, Pandya et al. 2017; Chauke et al. 2019). Here we assume that morphology and $F_{\rm HI}$ of galaxies depend on only their M_* and *SFR*. Then, galaxies on the star-forming main sequence (Peng et al., 2010; Whitaker et al., 2014; Renzini & Peng, 2015) would be gas-rich and have a morphology like typical spirals. At the same time, galaxies below the star-formation main sequence would be gas-poor ellipticals. The rejuvenation can move such gas-poor elliptical galaxies to the upper side on the M_*-*SFR* diagram. Because we divide galaxies by the 0.5 dex grid of M_* and *SFR*, in that case, we will choose original gas-rich spiral galaxies as non-smooth and "rejuvenated" elliptical galaxies as smooth. Also, Figure 3.3 shows > 0.5 dex difference between below and along the star-formation main sequence. It looks hard to cause > 0.5 dex change in $F_{\rm HI}$ by a single rejuvenation event so that the rejuvenated smooth galaxies will still have lower $F_{\rm HI}$ than non-smooth galaxies.

6.2 Illustris simulation

In order to distinguish these scenarios, we need the past formation history of smooth/non-smooth galaxies. Thus we use the result of Illustris simulation (Vogelsberger et al., 2014a,b; Genel et al., 2014; Nelson et al., 2015a) and Dickinson et al. (2018), who conducted morphological classification in the same manner as GZ2 (see Sec. 4.3). Illustris is a large volume hydrodynamical simulation of galaxy formation using a moving-mesh code AREPO (Springel, 2010) to follow the dynamics of dark matter and gas. It calculates the gravity, hydrodynamics, and necessary astrophysical models to reproduce the local universe. For example, gas cooling, supernova feedback, AGN feedback, and recycling are included (see Vogelsberger et al. 2014a for detail). The simulation starts from the redshift of $z = 127$ and traces the evolution of dark matter particles, gas resolution elements, stellar particles, and supermassive black holes in the box of 106.5^3 Mpc^3. As a result, Illustris simulation successfully reproduced the observational trend in the local and high-z universe (Genel et al., 2014; Sijacki et al., 2015). For example, Figure 6.1 shows the panel (c) of Figure 2 in Genel et al. (2014), which shows the excellent agreement of Illustris data (solid black lines) and observations (dots) in cosmic *SFR* density.

After the data release of Illustris (Nelson et al., 2015b), the Illustris team updated their simulation and introduced IllustrisTNG (Springel et al., 2018; Pillepich et al., 2018; Naiman et al., 2018; Nelson et al., 2018; Marinacci et al., 2018; Nelson et al., 2019). In this thesis, however, we refer to the result of the original Illustris simulation because only simulated galaxies in Illustris have the information of visual smoothness determined by the same method as GZ2.

6.2.1 Visual smoothness of simulated galaxies

The photometric images of simulated galaxies were generated by Torrey et al. (2015). They created the 'mini-snapshot' for each simulated galaxy at $z = 0$, including all relevant particles and their information. These mini-snapshots were used to determine the spectrum of each stellar particle, added the dust obscuration and nebular emission, and generated the images of a simulated galaxy from 16 angles (see Torrey et al. 2015 and Snyder et al. 2015 for the detail). After that, images were re-scaled to imitate SDSS

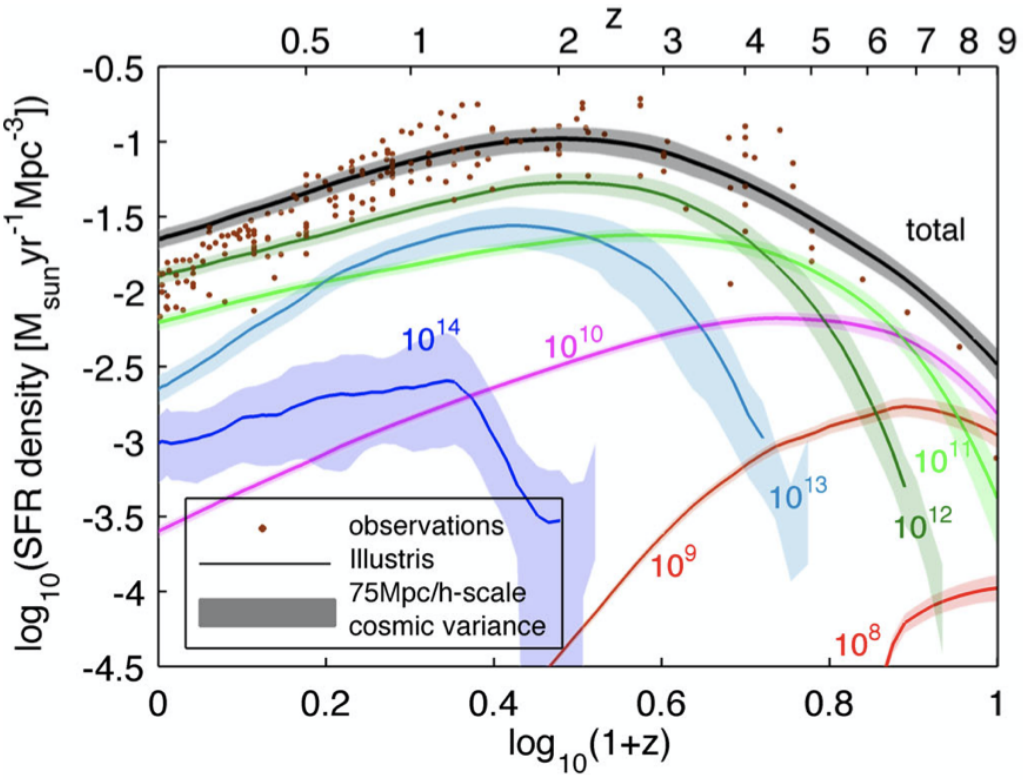

Figure 6.1: Panel (c) of Figure 2 in Genel et al. (2014) showing a comparison of Illustris simulation (solid lines) and observations (dots). Color lines show the contribution from halos with different halo mass. Observational data points are collected from various studies.

images used in GZ2 and convolved with a nominal Point Spread Function with Full Width of Half Maximum (FWHM) of 1.0 arcsec. Then simulated galaxies were put onto the background randomly selected from authentic SDSS images. These procedures made simulated galaxies as if they were located at $z = 0.05$ distance from the earth, which is the far side of the observational limit with the ALFALFA survey (see Sec. 2.2). Including the snapshots from different angles for the same object, the total number of generated images is 110,256.

Dickinson et al. (2018) conducted the visual inspection of those simulated images with the same method in GZ2 (see Sec. 4.3). Volunteers visit the GZ2 website, see the images generated by Illustris, and answer questions about its morphological features. As a result, Dickinson et al. (2018) obtained the reliable information of visual smoothness for 27,611 images (more than 40 votes). We calculate the vote fractions to "Smooth and rounded" and "Features or disk" ($f_{\rm smooth}$ and $f_{\rm non-smooth}$), and require the "smooth" and "non-smooth" simulated galaxies having $f_{\rm smooth} > 0.8$ and $f_{\rm non-smooth} > 0.8$, respectively. Our final subsamples in Illustris simulation are 8905 smooth and 1104 non-smooth galaxies.

Here we note the discrepancy of visual smoothness between the simulated galaxies and observed galaxies. Dickinson et al. (2018) reported that the Illustris and SDSS galaxies have different distributions of vote fraction to the answer "Features or disk" for the first question in GZ2, "Is the galaxy simply smooth and rounded, with no sign of a disk?" ($f_{1\rightarrow \rm F}$). Figure 6.2 shows the normalized distribution of the $f_{1\rightarrow \rm F}$ for simulated and observed galaxies as a blue line and green shade, respectively (Figure 4 in Dickinson et al. 2018). Vote fraction close to 1.0 means that most participants recognized a galaxy having a "Features or disk" component. On the other hand, vote fraction ~ 0 is the result that most participants chose "Smooth and rounded" or "Star or artifact" here. Dickinson et al. (2018) selected SDSS galaxies within the redshift range of $0.045 < z < 0.055$ and set their distribution along M_* by bootstrap resampling for the fair comparison between simulated galaxies and observed galaxies. Because the simulated galaxies are moved from $z = 0$ to $z = 0.05$ in creating synthetic images, Figure 6.2 compares simulated galaxies at $z = 0$ and observed galaxies at $z \sim 0.05$. Dickinson et al. (2018) expected that the evolution of galaxy morphology between $z = 0.05$ and $z = 0$ is slight and that the effect of the displacement should be negligible. Figure 6.2 clearly shows that SDSS galaxies have two peaks at both ends of the x-axis

while Illustris galaxies have peaked around $f_{1\to \mathrm{F}} \sim 0.1$ and ~ 0.6. Dickinson et al. (2018) mentioned the possible contribution of massive non-smooth ($M_* > 10^{10.5} M_\odot$) often observed in local universe. Authors have reported that such a population is rare in the simulated universe (Toth & Ostriker, 1992; Quinn et al., 1993; Velazquez & White, 1999; Kazantzidis et al., 2008; Stinson et al., 2010). Although Illustris simulation produces massive non-smooth galaxies, their fraction to the total number of the galaxy could be smaller than that in the local universe. In addition, Torrey et al. (2015) omitted the modeling of dust emission/absorption when they generated the synthetic images of simulated galaxies, which made a mismatch of absolute magnitude between Illustris and SDSS galaxies in five SDSS filters (Dickinson et al., 2018). Although such discrepancy between the simulated and observed universe would make the different morphological distribution (Figure 6.2), we believe that Illustris reproduced the local universe well, at least for galaxies with the vote fraction of > 0.8.

6.2.2 Morphological impact on F_{HI} in simulated galaxies

Before tracing the formation history of simulated smooth/non-smooth galaxies, we confirm if Illustris simulation reproduces the morphological impact on F_{HI} shown in Figure 4.2. Figure 6.3 shows the distribution of smooth/non-smooth galaxies on M_*-*SFR* plane as red/blue contours, respectively. Here we use the total M_* and *SFR* in the dark matter halo, which is the sum of the mass for all stellar components and the sum of the *SFR* for all gaseous cells, respectively. Again, we show the number of smooth and non-smooth galaxies in each grid by red and blue numbers.

Compared to Figure 4.4, we have large number of smooth galaxies with $0.5 - 1$ dex lower *SFR* than star-forming main sequence. We again decide to conduct F_{HI} comparison only for the bins with ≥ 10 smooth and ≥ 10 non-smooth galaxies (orange shade in Figure 6.3). After the same analysis as Sec. 4.3, we obtained Figure 6.4. Most points are above the line of 0 in the bottom panel, which means that visually smooth galaxies have a lower gas fraction than non-smooth galaxies at the same M_* and *SFR* in the simulated universe. This trend is significant for galaxies with $M_* < 10^{11} M_\odot$, which is consistent with our observational result in Sec.4.3.

We note that $0.55^{\pm 0.28}$ dex median difference of F_{gas} in Illustis is smaller than that with observations (~ 0.75 dex in Sec. 4.3). We can consider several origins of this

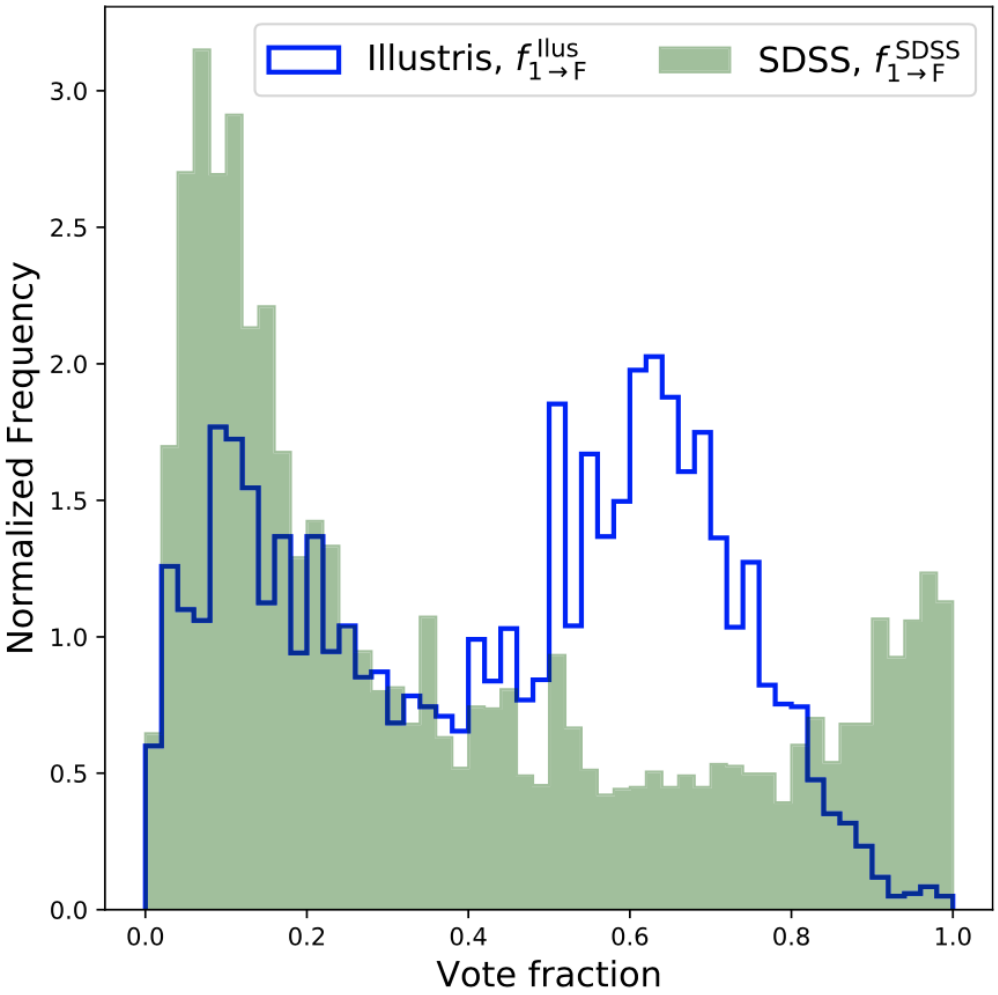

Figure 6.2: Figure 4 in Dickinson et al. (2018) showing a comparison of the vote fraction to the answer "Features or disk" for Illustris and SDSS galaxies (blue line and green shade, respectively).

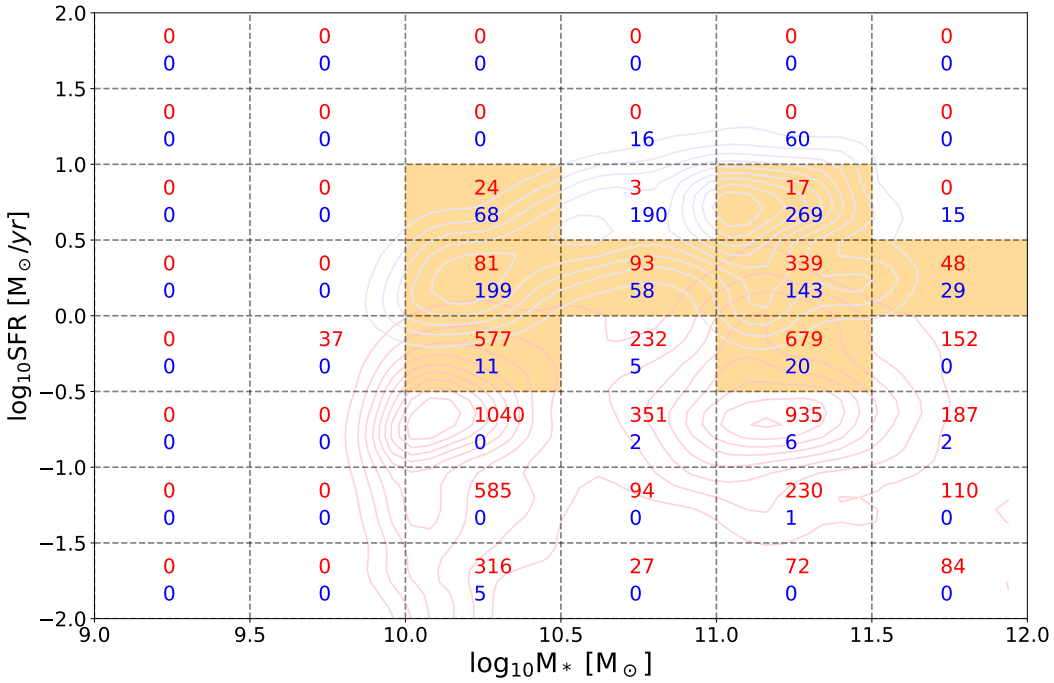

Figure 6.3: Same as Figure 4.4 but for Illustris galaxies. Red and blue contours are the distribution of smooth and non-smooth galaxies, respectively. Numbers in each grid mean the number of smooth (red) and non-smooth (blue) galaxies in that M_* and *SFR* bin.

discrepancy. For example, observations do not cover the massive end of the trend in Figure 6.4. Thus the Illustris simulation might predict the decreasing difference of F_{gas} along M_*. Also, some parts of smooth galaxies in Illustris simulation can be contaminated from the intermediate population ($f_{1\to \mathrm{F}} \sim 0.2 - 0.8$). Figure 6.2 shows the possible shift of vote fraction for intrinsically high $f_{1\to \mathrm{F}}$ galaxies to the left side, which can cause misclassification of essentially intermediate population as smooth galaxies. Therefore, we have to keep this possible pollution in our minds when interpreting the result from the Illustris simulation.

6.3 Formation history of simulated smooth/non-smooth galaxies

Hereafter we study the formation history of smooth/non-smooth galaxies in Illustris simulation. Illustris-1 simulation includes the time evolution of various parameters, and they are publically released to researchers (Nelson et al., 2015a,b).

Firstly, we focus on the evolution of total M_* and *SFR* in the dark matter halo of smooth/non-smooth galaxies. After we divide simulated galaxies by their M_*, *SFR*, and visual smoothness at $z = 0$, we calculate average formation histories in each bin. Because Illustris has records of various parameters for all dark matter halos at each timestep, we take a median of M_* and *SFR* for smooth/non-smooth galaxies at each timestep. This procedure is repeated from the birth of the simulated universe (number of the snapshot, $N_{\mathrm{snap}} = 0$) to $z = 0$ ($N_{\mathrm{snap}} = 135$) to produce the median formation history of simulated galaxies. The Illustris simulation changes the time interval between snapshots at every calculation. We briefly summarize the time intervals between snapshots in Table 6.1.

Figure 6.5 and 6.6 show the median M_* and *SFR* history, respectively. Each panel corresponds to the grid in Figure 6.3. As a result, red and blue lines in Figure 6.5 and 6.6 draw almost the same evolution of M_* and *SFR* for most bins. For some bins in Figure 6.5, the stellar mass of smooth galaxies evolves more rapidly than non-smooth galaxies. However, the difference of median M_* at the same snapshot is always within 0.5 dex, except for the bin of $11.0 < \log_{10} M_*\ [M_\odot] < 11.5$ and $-0.5 < \log_{10} SFR\ [M_\odot/yr] < 0.0$. Our result in Figure 3.4 shows that > 0.5 dex diffference is necessary to explain ~ 0.55

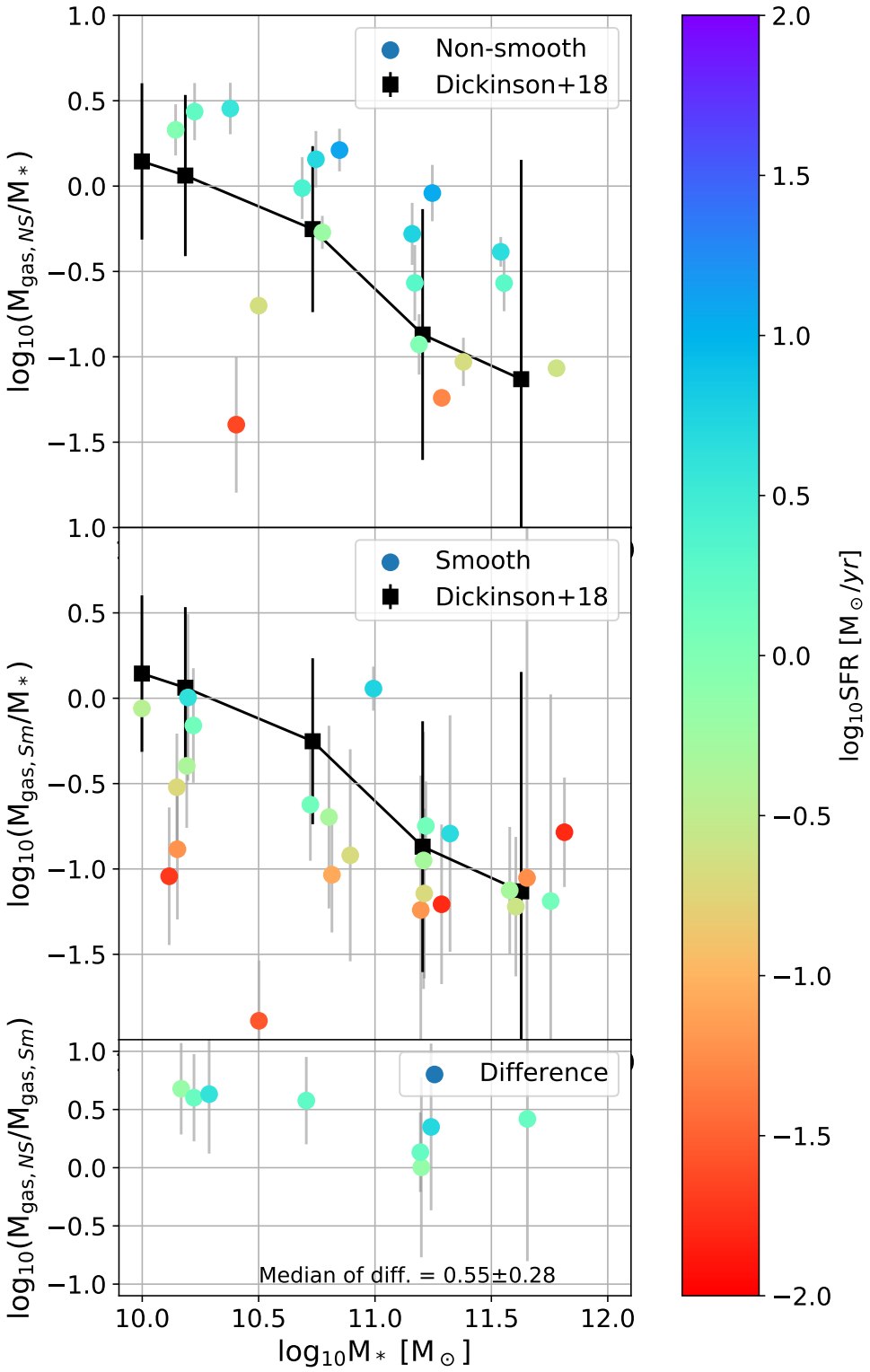

Figure 6.4: Same as the right column of Figure 4.2 but for Illustris smooth/non-smooth galaxies. The black points and solid line show the stacking result for all galaxies from Dickinson et al. (2018) by simply dividing them into five stellar mass bins (similar as magenta stars in Figure 3.4).

$N_{\rm snap}$	Lookback time [Gyr]	redshift	time interval [Gyr]
0	13.698	46.77	0.004
20	13.537	17.96	0.015
40	13.002	7.24	0.040
60	11.556	3.01	0.075
80	8.542	1.21	0.150
100	5.581	0.58	0.172
120	2.399	0.20	0.180
135	0.000	0.00	0.068

Table 6.1: Time intervals in Illustris simulation

dex difference in F_{gas}. Therefore, we guess that the slightly different M_* evolution is hard to produce the different F_{gas} in the bottom panel of Figure 6.4. In addition, from Figure 6.6, we can deny the rejuvenation scenario in Sec. 6.1. Rejuvenated smooth galaxies must show the recent rise of *SFR*, which is not seen in most panels of Figure 6.6. The width of the timestep in Illustris is enough to capture the sign of rejuvenation if it exists ($\Delta t_{\rm look} \sim 70$ Myr around $z = 0$).

On the other hand, Figure 6.7 suggests the different evolution of gas mass ($M_{\rm gas}$) between simulated smooth and non-smooth galaxies. From the combination of Figure 6.5 and 6.7, we can estimate that the different F_{gas} have appeared since 4-6 Gyr ago. The discrepancy between the $M_{\rm gas}$ and *SFR* history is consistent with the observational result by Catinella et al. (2018), which again implies that non-smooth galaxies contain a significant amount of H I not used in the star-formation (Sec. 5.5).

Figure 6.8 also implies that black hole mass ($M_{\rm BH}$) of smooth and non-smooth galaxies would have different evolutionary paths. For some bins, smooth galaxies show the rapid increase of $M_{\rm BH}$ around $t_{\rm lookback} \sim 10$ Gyr and keep that difference from non-smooth galaxies until now. However, this trend is observed most clearly in the bin with $11.0 < \log_{10} M_* \ [M_\odot] < 11.5$ and $-0.5 < \log_{10} SFR \ [M_\odot/yr] < 0.0$, in which we can not see the significant difference of $F_{\rm gas}$ (the bottom panel of Figure 6.4). Thus we consider that the different $M_{\rm BH}$ is hardly related to the different $F_{\rm gas}$ at $z = 0$.

Among three scenarios in Sec. 6.1, the galaxy-galaxy merger and gravitational instability are appropriate to connect the different $F_{\rm gas}$ history and different morphology at $z = 0$ of smooth and non-smooth galaxies.

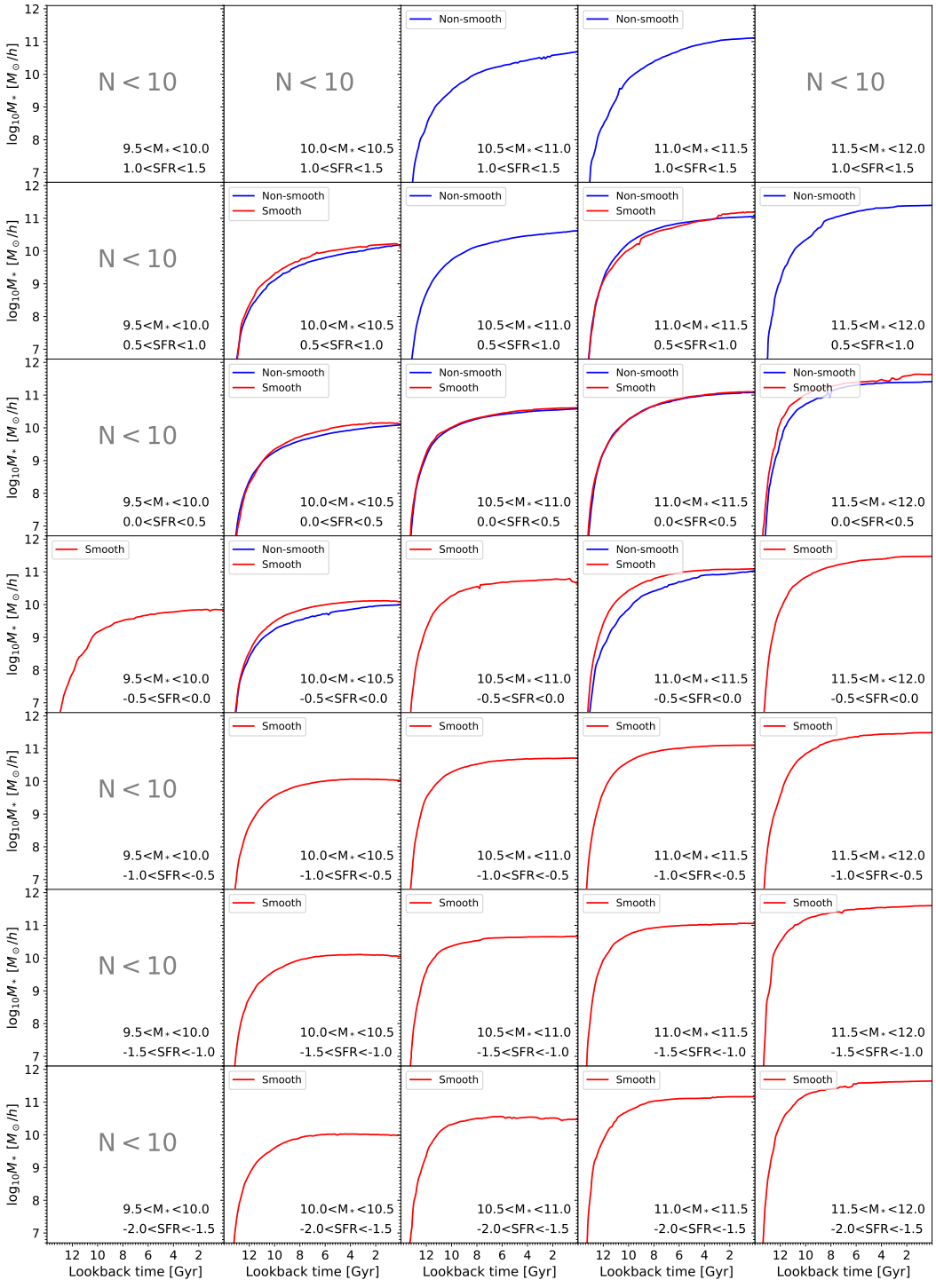

Figure 6.5: Average evolution of M_* in simulated galaxies. Panels are divided by the M_* and *SFR* at $z = 0$ as shown by dashed grids in Figure 6.3. Red and blue lines correspond to smooth and non-smooth galaxies, respectively.

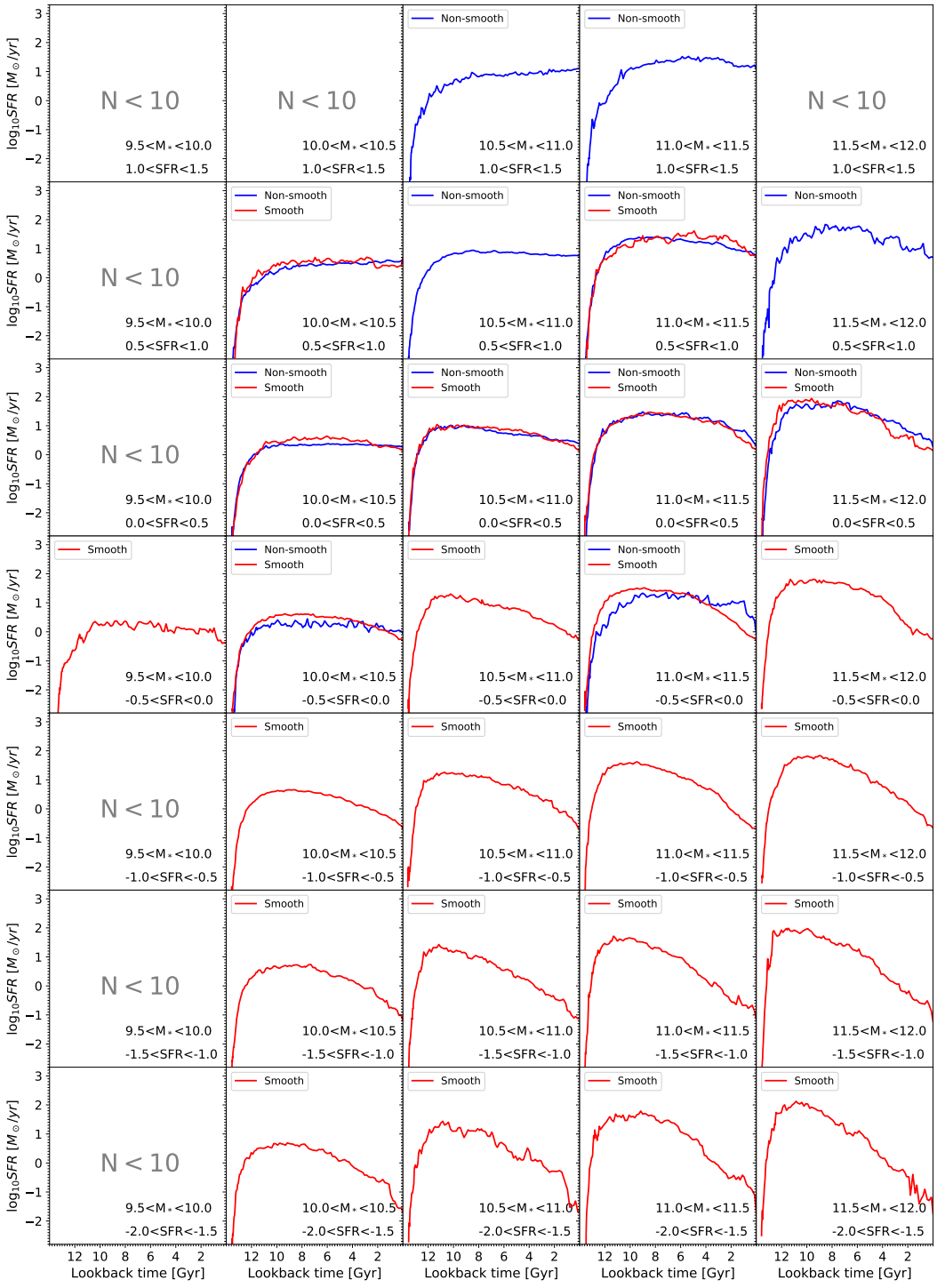

Figure 6.6: Average evolution of *SFR* in simulated galaxies. Panels and lines are the same as Figure 6.5.

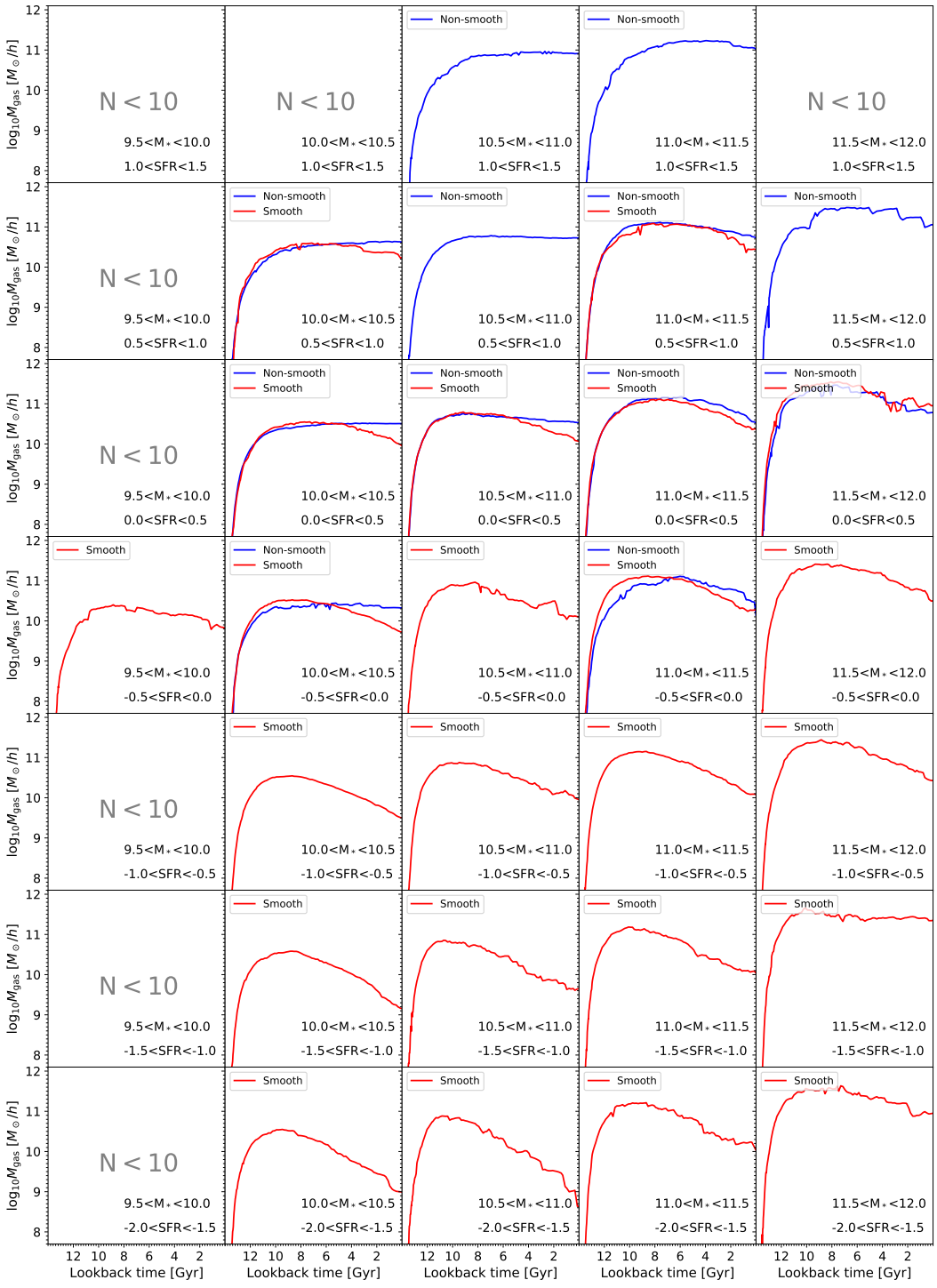

Figure 6.7: Average evolution of gas mass ($M_{\rm gas}$) in simulated galaxies. Panels and lines are the same as Figure 6.5.

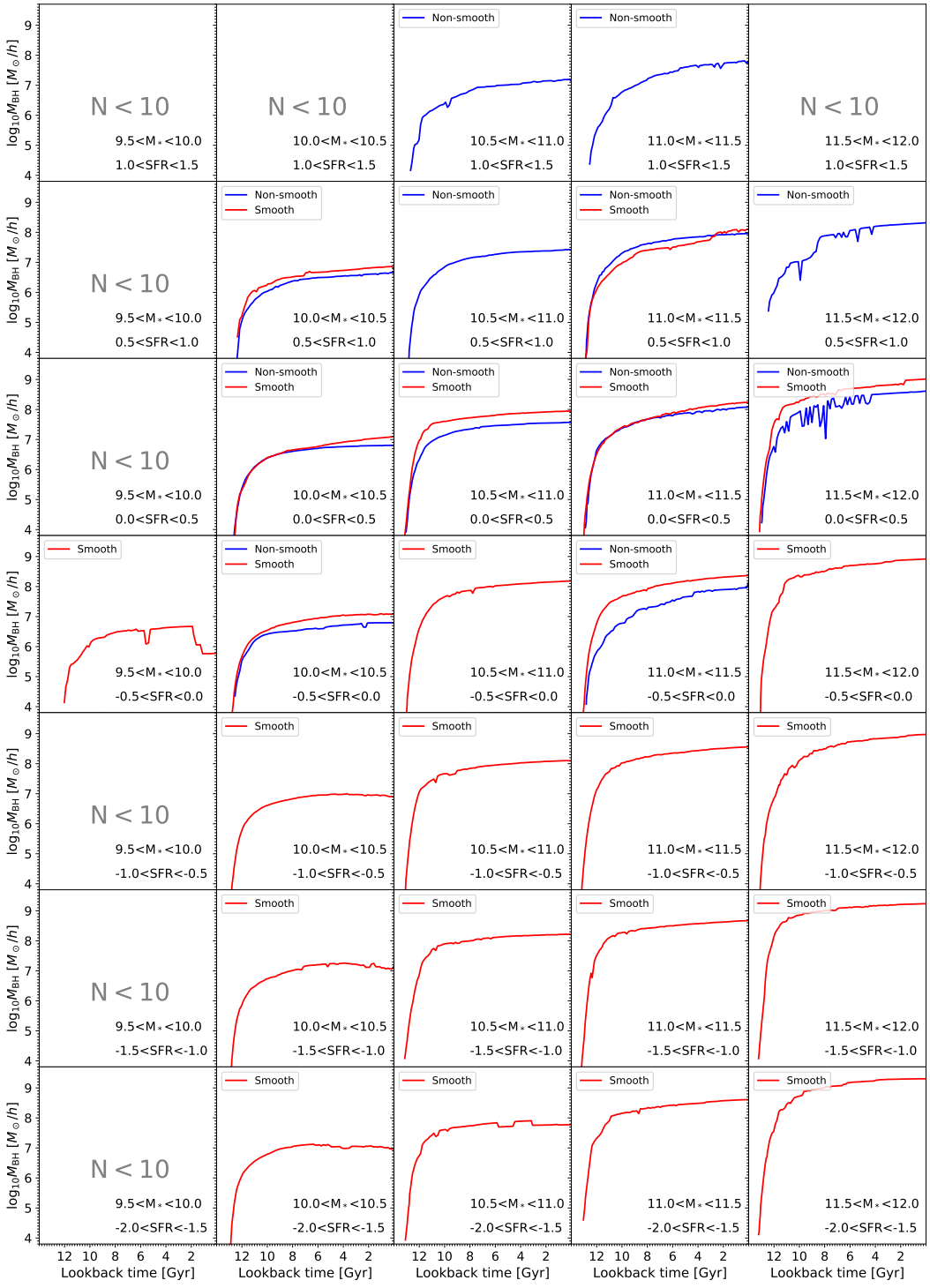

Figure 6.8: Average evolution of black hole mass ($M_{\rm BH}$) in simulated galaxies. Panels and lines are the same as Figure 6.5.

6.4 Merger history of Illustris galaxies

Our analysis in Sec. 6.3 implicates the importance of past mergers in the relation of visual morphology and gas fraction of galaxies. Thus, this section will study the merger history of smooth/non-smooth galaxies in a simulated universe. The Sublink algorithm picks out the merger history of $z = 0$ dark matter halo in Illustris project (Rodriguez-Gomez et al., 2015). This algorithm supplies us with much information, e.g., halo mass at that snapshot and the progenitor of a halo at one step before. Here we focus on galaxy-galaxy mergers in the main progenitor branch, the most massive history of that $z = 0$ halo. We find the mergers at each timestep and divide them by the mass ratio of merging halos ($r = M_{\mathrm{halo,A}}/M_{\mathrm{halo,B}}$, $0 < r < 1$). Mergers with $r > 0.3$ is defined as major mergers, $0.1 < r < 0.3$ as minor mergers, and $r < 0.1$ as very small mergers.

Here we note that, for the snapshots where more than one mergers occur, we define the mass of the most massive merging halo as a denominator of r. Then we count the number of mergers in two different ways. Firstly, we count the number of all individual merging halos as the number of mergers ($N_{\mathrm{individual}}$). In other words, we consider that merging halos accrete in order even if more than two halos have merged between two consecutive snapshots. Figure 6.9, 6.10, and 6.11 show the result with this method for major, minor, and very small mergers, respectively. We show the median number as vertical dashed lines for each population. In addition, we conduct the K-S test for seven bins containing enough smooth and non-smooth galaxies ($N_{\mathrm{obj}} \geq 10$). The p-value from the K-S test is written on the right middle of each panel. The number distributions of major mergers in smooth/non-smooth galaxies are similar for all M_* and *SFR* range (Figure 6.9). On the other hand, some bins of Figure 6.10 suggest the different distribution of $N_{\mathrm{minor,individual}}$ between smooth and non-smooth galaxies (p<0.05). Especially for massive bins ($M_* > 10^{11} M_\odot$), smooth galaxies have experienced more minor mergers in the past. However, this trend is not clear in the less-massive side ($M_* < 10^{11} M_\odot$), where the morphology-F_{gas} relation is consistent with the observation. We consider that the different history for minor mergers in massive galaxies can affect their morphologies, but it would not correlate to the gas fraction of galaxies.

Figure 6.11 then suggests that less-massive non-smooth galaxies ($M_* < 10^{11.0} M_\odot$)

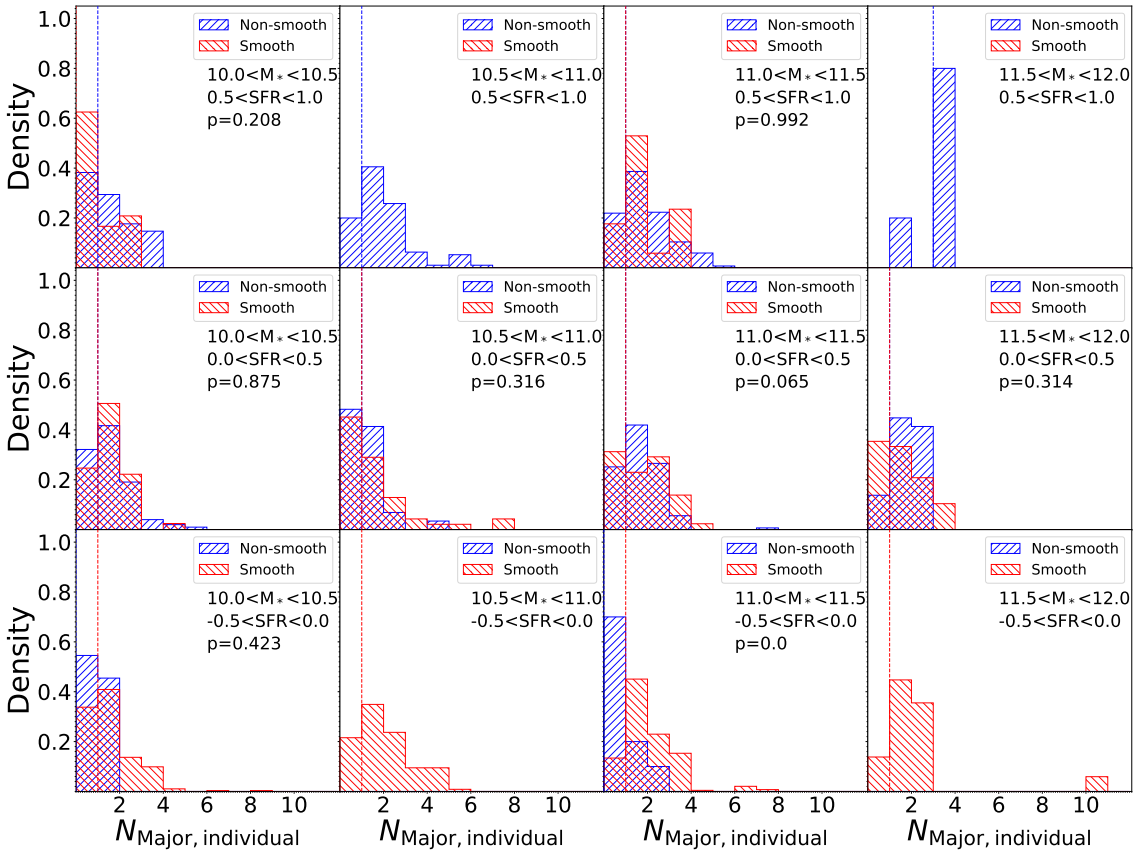

Figure 6.9: Red and blue histograms show the number distribution of major mergers in each M_* and *SFR* bin for smooth and non-smooth galaxies, respectively. Y-axis is normalized by the total number of major mergers in that bin.

have experienced slightly more very small mergers than smooth galaxies have while massive bins show opposite trend ($M_* > 10^{11} M_\odot$). Here we note that the x-axis of panels is different in each column. Because the mass ratio between two galaxies is less than 10%, very small mergers cannot directly contribute to the different gas fractions at $z = 0$. Nevertheless, very small mergers might have a role in keeping the turbulent gravitational potential where structures can be born (Sec. 6.1), especially in less-massive galaxies. Such turbulence will hardly occur in a massive halo. Thus we conclude that the different histories with very small mergers can contribute to the morphology-$F_{\rm gas}$ relation at $z = 0$ for the galaxies with $M_* < 10^{11} M_\odot$.

Secondly, we count the number of all snapshots where a merger event happens ($N_{\rm snapshot}$). This analysis does not distinguish simultaneous mergers by more than

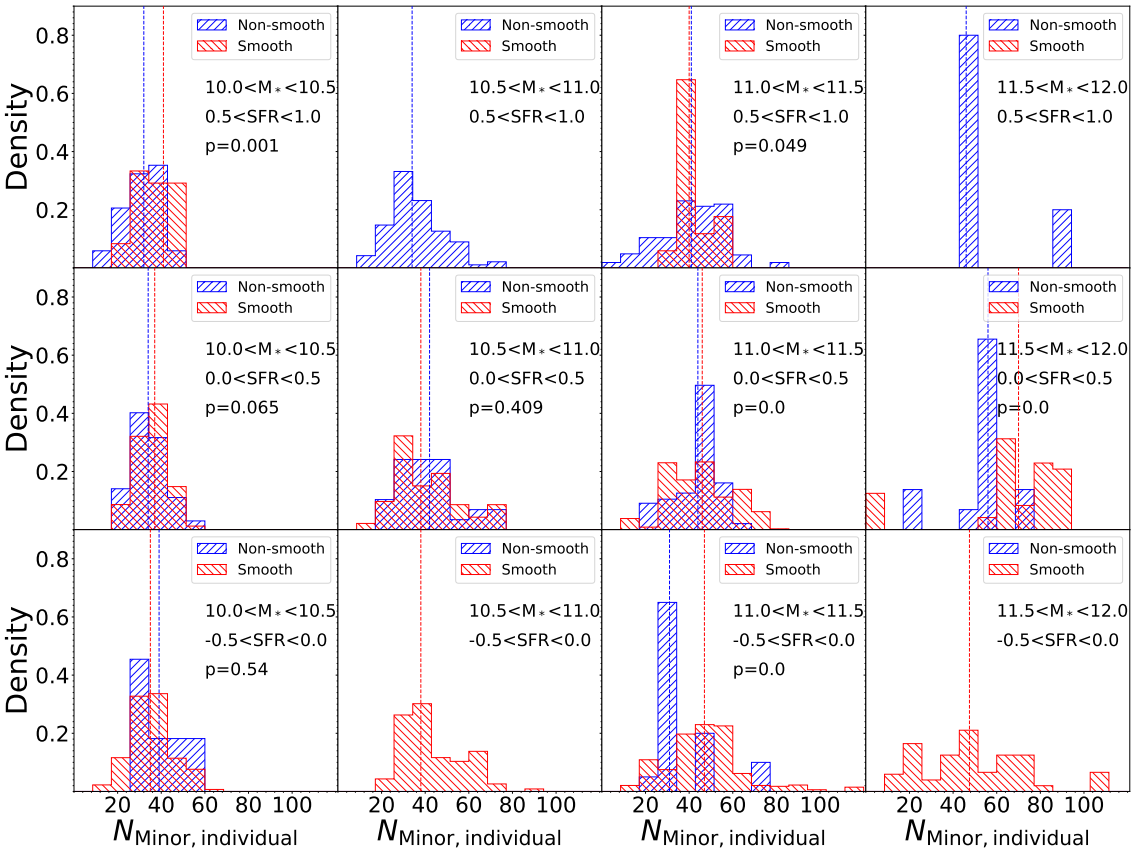

Figure 6.10: Same as Figure 6.9 but for minor mergers.

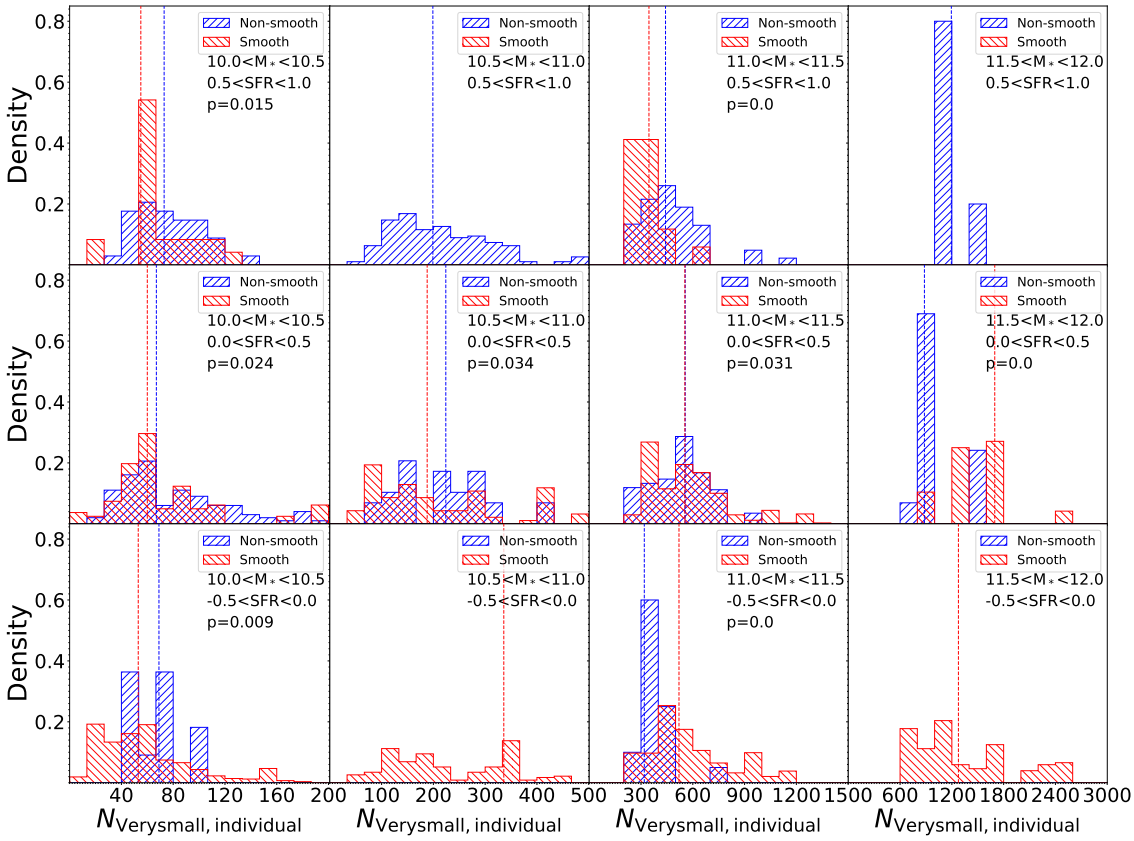

Figure 6.11: Same as Figure 6.9 but for very small mergers. We use different ranges of x-axis for each column because of large number of very small mergers in massive bins ($M_* > 10^{11} M_\odot$).

two halos but counts how often mergers occur. Again we divide mergers into the major, minor, and very small, and count $N_{\rm snapshot}$ for each $z = 0$ halo. The number of mergers in smooth and non-smooth galaxies are summarized at each M_* and *SFR* bin and compared in Figure 6.12, 6.13, and 6.14. We can see that there is no clear discrepancy in the number of snapshots hosting major/minor mergers between smooth and non-smooth galaxies. The median number of mergers is similar, and the p-value is larger than 0.05 for most M_* and *SFR* bins. On the other hand, Figure 6.14 suggests that less-massive non-smooth galaxies have experienced very-small mergers more frequently than smooth galaxies have ($M_* < 10^{11} M_\odot$). While continuous mergers in less massive non-smooth are consistent with the gravitational instability scenario (Sec. 6.1), massive bins do not show such a trend. Therefore, we consider that the different $F_{\rm gas}$ and morphology in massive smooth and non-smooth ($M_* > 10^{11} M_\odot$) is not a result of different merger history.

6.5 Summary of this chapter

In this chapter, we study the origin of visual smoothness and its connection to H I gas content with the result of Illustris, recent cosmological simulation. Because Illustris contains the records of various parameters of simulated galaxies from the start of its calculations to $z = 0$, we can look back at the formation history of $z = 0$ galaxies. In addition, Torrey et al. (2015) and Snyder et al. (2015) created the photometric images of simulated galaxies in Illustris, and Dickinson et al. (2018) conducted the visual classification of their morphology in the same manner as GZ2 (Willett et al., 2013). We connected the information of visual smoothness and past formation history of simulated galaxies to study the possible mechanisms behind the morphology-$F_{\rm HI}$ relation observed in the local universe.

After checking the consistency between simulated galaxies and observed result (Figure 6.4), we investigate the evolution history of M_*, *SFR*, $M_{\rm gas}$, and $M_{\rm BH}$ of smooth/non-smooth galaxies at $z = 0$ (Figure 6.5, 6.6, 6.7, and 6.8). The evolution history of M_* and *SFR* is similar between smooth and non-smooth galaxies at most M_* and *SFR* bins, which suggests that there is no signature of rejuvenation in smooth galaxies. On the other hand, the evolution of $M_{\rm gas}$ gives us a hint of background physics. Figure 6.7 shows that smooth galaxies decrease the amount of gas from

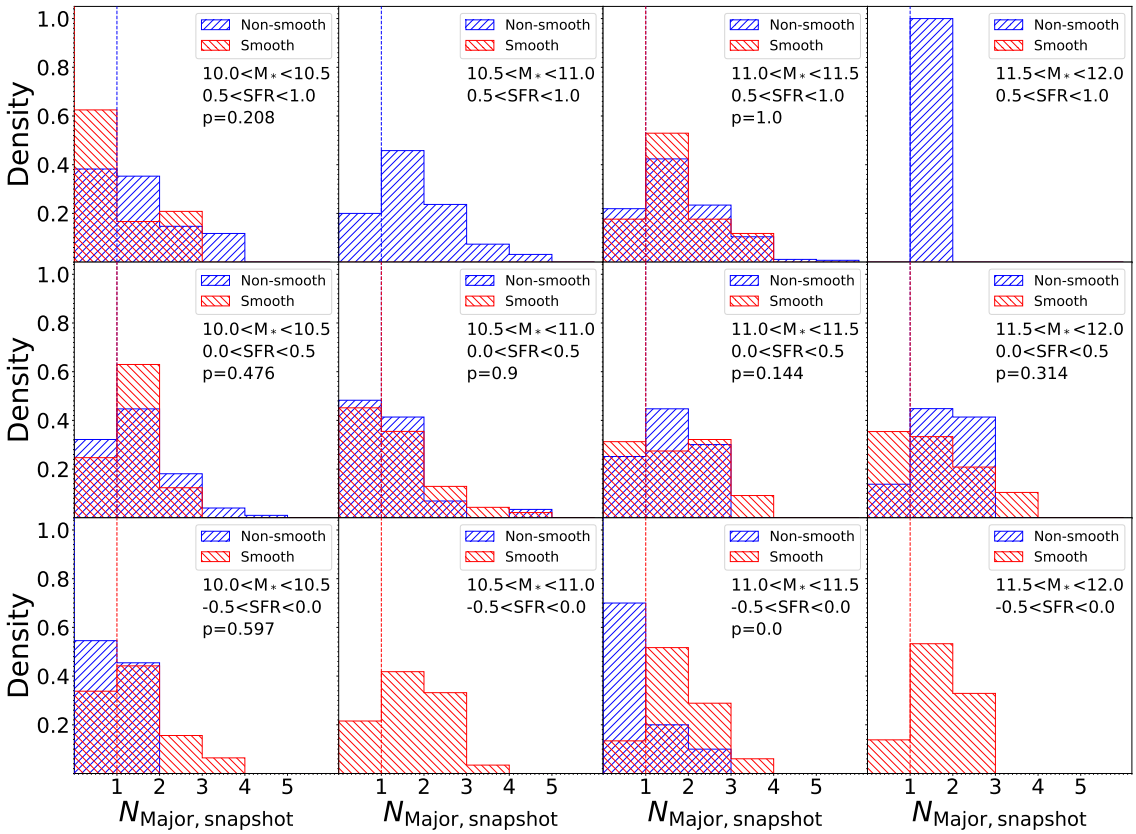

Figure 6.12: Red and blue histograms show the number distribution of major mergers in each M_* and *SFR* bin for smooth and non-smooth galaxies, respectively. Y-axis is normalized by the total number of major mergers in that bin.

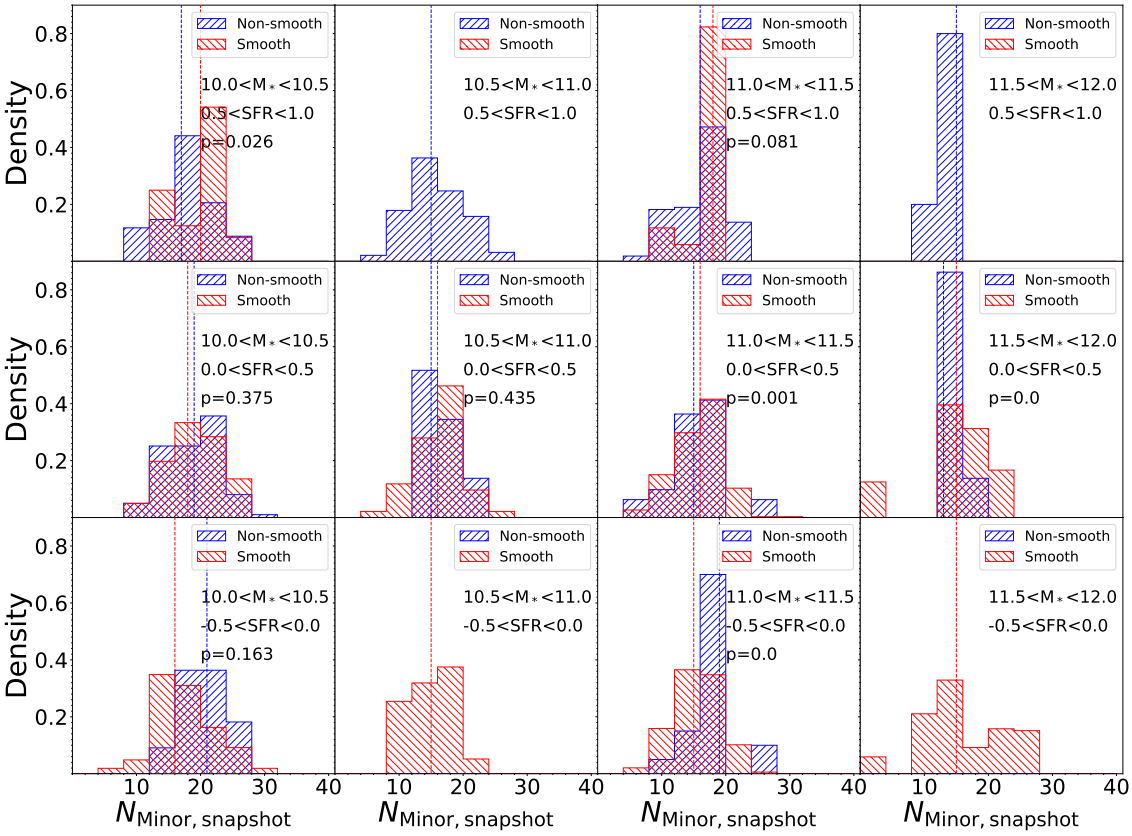

Figure 6.13: Same as Figure 6.12 but for minor mergers.

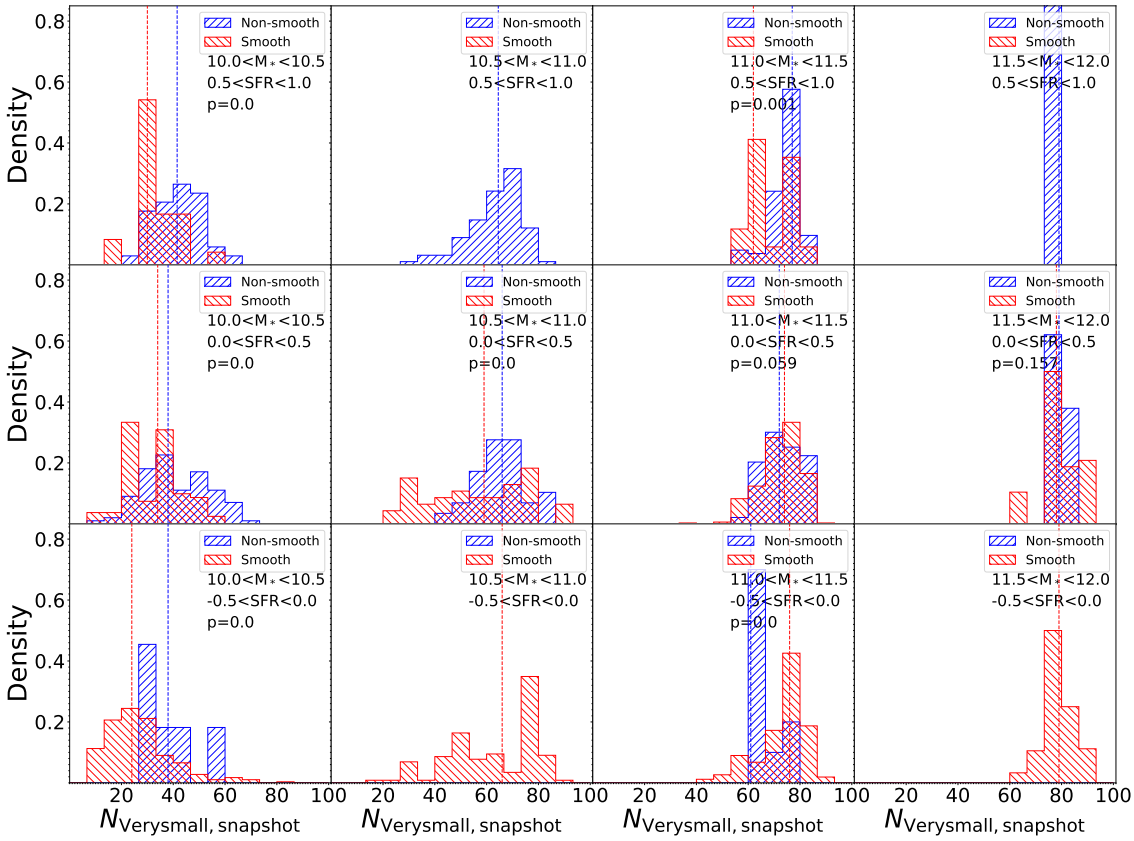

Figure 6.14: Same as Figure 6.12 but for very small mergers.

$t_{\rm look} = 4 - 6$ to 0 Gyr. The decrease of $M_{\rm gas}$ only in smooth galaxies can be explained by different gas accretion or stripping of gas. We can demonstrate the former by comparing the merger history of simulated galaxies. However, the latter is still difficult to verify even with the simulation because we need the information of individual gas components in a dark matter halo.

Figure 6.8 shows that smooth galaxies have higher $M_{\rm BH}$ from $t_{\rm look} = 10$ to 0 Gyr in some bins. Although the different $M_{\rm BH}$ history would imply the different mass accretion, we can see the largest difference in the bin where we cannot see the difference in $F_{\rm gas}$. Therefore we consider that the different evolution of $M_{\rm BH}$ would not correlate with the different $F_{\rm gas}$ evolution.

Then We investigate the merger history of smooth/non-smooth galaxies in Illustris simulation. Here we divide mergers into three types by the halo mass ratio of merging galaxies, major merger ($M_{\rm halo,A}/M_{\rm halo,B} > 0.3$), minor merger ($0.1 < M_{\rm halo,A}/M_{\rm halo,B} < 0.3$), and very small merger ($M_{\rm halo,A}/M_{\rm halo,B} < 0.1$). Also, we count those mergers in two different ways; the number of individual mergers ($N_{\rm individual}$) and the number of snapshots where those merger events happened ($N_{\rm snapshot}$). The former means how many mergers happened in total, and the latter shows the continuity of merger events. The results are summarized in Figure 6.9 to 6.14. We can see that the number of major and minor mergers is the same between smooth and non-smooth galaxies in both methods. On the other hand, both $N_{\rm individual}$ and $N_{\rm snapshot}$ of very small mergers suggest the correlation with the visual morphology of galaxies in less-massive bins ($M_* < 10^{11} M_\odot$ in Figure 6.11 and 6.14). Continuous merger events can sustain the turbulent mode of gravitational potential and the formation of small-scale structures (Irwin, 1994; Elmegreen et al., 1995; Renaud et al., 2014). Keeping such turbulence in the gas-rich disk will cause different visual morphology at $z = 0$. Thus we expect that the smooth galaxies had similar properties as non-smooth galaxies until $t_{\rm look} = 4 - 6$ Gyr and failed to keep the turbulent disk by the decreasing gas and lack of consecutive mergers.

Unfortunately, we could not reach a clear conclusion in massive smooth/non-smooth galaxies. Other possible scenarios are, for example, different properties of mergers, galaxy harassment, or other indirect physics. While wet mergers cause a bursty star-formation, dry mergers are believed as a way of quiescent mass accumulation onto the brightest cluster galaxies (Sanders et al., 1988; Tran et al., 2008). Also, we cannot

obtain the information when smooth and non-smooth get a different appearance. Figure 6.7 gives us a hint that $M_{\rm gas}$ have differed since 6-8 Gyr ago, corresponding to $z = 0.65 - 1.0$. We will be able to make it clear by a detailed morphological classification with high-quality images and the future H I survey by the Square Kilometre Array (SKA; Dewdney et al. 2009; Yahya et al. 2015).

7 Summary

In this thesis, we demonstrate the morphological impact on the H I gas mass of galaxies by removing the effect of M_* and *SFR*. Using the ALFALFA survey data, we performed H I spectral stacking analysis for local star-forming galaxies (selected from SDSS) with a wide range in stellar mass, *SFR*, and morphological types. Following the same stacking method presented by Fabello et al. (2011) and Brown et al. (2015), we show the scaling relation between the stellar mass and the H I gas fraction (Figure 3.4). Figure 3.4 also suggests that the H I gas mass depends not only on the stellar mass but also on the star-formation activity of the host galaxies. This result is consistent with Brown et al. (2015), who concluded that the star-formation activity is a primary driver of the H I gas content in a galaxy.

We then divide our sample by their M_*, *SFR*, and morphologies using three morphological parameters; Sérsic n, C-index, and visual smoothness. The number of galaxies in each bin is summarized in Figure 4.1, 4.3, and 4.4. We perform the stacking analysis of the radio spectra in all bins with ≥ 10 objects. Our study revealed that *at fixed stellar mass and SFR*, H I gas mass fraction ($F_{\rm HI}$) does not significantly depend on

their morphologies when we use C-index for morphological classification. On the other hand, we do find a significant morphological difference (~0.7 dex) when we use visual smoothness as a morphological indicator (Figure 4.2). Unfortunately, we could not obtain any clear trend from our analysis with Sèrsic index due to the small number of early-type galaxies in our sample. Because we fixed the stellar mass and the *SFR* of two morphological populations when comparing the H I gas mass, our result is free from any bias originating from the stellar mass and the *SFR*. We also investigate the environmental impact on our results. We performed the K-S test and found p-values of >0.05 for most of the (M_*, *SFR*) bins. Therefore, we conclude that dense environments like galaxy clusters do not affect our results.

We study how the visual smoothness correlates with the other morphological indicators. Figure 5.2 shows that the visual smoothness judged by the citizen scientists is different from the traditional automated distinction between early/late-type or bulge/disk morphologies, at least in the local universe (Figure 5.2). Similarly, we find that the asymmetry index (A) and the clumpiness parameter (S) are also different from the visual smoothness determined by the citizen scientists, while the Gini coefficient (G) and the second-order moment parameter (M_{20}) tend to distinguish smooth and non-smooth galaxies better. We also compare the optical images of non-smooth and smooth galaxies in Figure 5.5 and Figure 5.6. We notice that only non-smooth galaxies have small-scale structures within the galaxies. We argue that the existence of small-scale structures would contribute to the scatter of the $M_* - SFR - F_{\rm H_I}$ relationship in the local universe. Because Sérsic n and C-determining the indicators that describe the overall (1-D) light profile from the center of the galaxies to the outskirts, those parameters would likely miss the small-scale structure. A and S can also overlook such faint systems due to the background noise. On the other hand, G and M_{20} are free from the background subtraction and better to capture faint structures Conselice 2014.

To identify the physics that determines galaxies' smoothness, we investigate the formation history of smooth and non-smooth galaxies in the Illustris simulation. Here we use simulated smooth and non-smooth galaxies divided by Dickinson et al. (2018) who conducted the visual classification in the same manner as GZ2. We first compare $F_{\rm gas}$ of smooth and non-smooth galaxies from the simulation as we performed for the observational data in Sec. 4. Figure 6.4 shows that the Illustris simulation reproduces the observational trend that smooth galaxies show the diminishment of $F_{\rm gas}$ at the

same M_* and *SFR*, especially in the $M_* < 10^{11} M_\odot$. Then we trace the average evolution histories of M_*, *SFR*, $M_{\rm gas}$, and $M_{\rm BH}$ in simulated galaxies. Figure 6.5 and 6.6 show that smooth and non-smooth galaxies have similar evolution history of M_* and *SFR* in all M_* and *SFR* bin. On the other hand, the evolution of $M_{\rm gas}$ is different between smooth and non-smooth galaxies (Figure 6.7). Some bins in Figure 6.8 also show the discrepancy of $M_{\rm BH}$ evolution between smooth and non-smooth. However, we cannot see the significant $F_{\rm gas}$ difference in the bin where we see the most significant difference in the $M_{\rm BH}$ evolution. Likely, the different $M_{\rm BH}$ is not related to the primary physics working behind the morphology-$F_{\rm gas}$ relation at $z = 0$.

Because the past merger history is deeply correlated to the morphology and $F_{\rm gas}$, hereafter, we focus on the merger history of simulated smooth and non-smooth galaxies. We divide mergers by the mass ratio of two merging galaxies into major, minor, and very small mergers. We count the number of mergers in the two methods; we first distinguish the individual mergers and calculate the total numbers (Figure 6.9, 6.10, and 6.11). Second, we count the number of snapshots hosting each type of merger (Figure 6.12, 6.13, and 6.14). Our analysis suggests that smooth and non-smooth have had a similar number of major and minor mergers in most M_* and *SFR* bins. In contrast, non-smooth galaxies have experienced more very small mergers than smooth galaxies at the same M_* and *SFR* in the M_* range of $< 10^{11} M_\odot$. Because continuous merger can maintain turbulent disks, we consider that the combination of gas-richness and gravitational stability is an origin of current morphology-$F_{\rm gas}$ relation at the fixed M_* and *SFR*. In other words, present smooth galaxies would have failed to keep their disk gas-rich and in the turbulent mode, resulting in the morphology-$F_{\rm HI}$ relation at $z = 0$.

While the result in the $M_* < 10^{11} M_\odot$ side is consistent with a scenario of different merger histories and gravitational instability (Sec. 6.1), $M_* > 10^{11} M_\odot$ galaxies have similar experiences of the very small merger between smooth and non-smooth galaxies regardless of the type of mergers. The different behavior in massive bins may indicate that the dominant mechanism in galaxy evolution will change around $M_* \sim 10^{10.5} M_\odot$, as pointed out by previous studies on the luminosity function of galaxies (Silk & Mamon, 2012).

In our study, we revealed the existence of morphology-$F_{\rm gas}$ relation at the fixed M_* and *SFR* and attempted to identify its background physics with both observations and simulation. However, our study has opened new questions to be unraveled by

future studies. For example, we cannot identify *when* such physics has worked on the galaxies with our current observation/simulation dataset. In the Illustris simulation, we find that the difference in $F_{\rm gas}$ between smooth and non-smooth appeared around $z = 0.65 - 1.0$. H I 21 cm lines at this redshift range are undetectable with any of the existing facilities. Still, their detection will become possible by the future observations with SKA (Dewdney et al., 2009; Yahya et al., 2015), which we believe can confirm our results shown in Figure 6.7 in this thesis. In addition, the mechanism(s) responsible for the reduction of gas in smooth galaxies is still unclear (Figure 6.7). Simulations have the potential to investigate the issue deeper—for example, by tracing the individual gaseous components in a dark matter halo, we may be able to confirm the effect of gas stripping. Furthermore, a detailed classification of galaxy morphology in the more distant universe is necessary to figure out the evolution of morphology-$F_{\rm gas}$ relation. We believe that the Hyper Suprime-Cam Subaru Strategic Program (HSC-SSP; Aihara et al. 2018) will provide us with good-quality imaging data for a statistical sample of galaxies. The recent collaboration with citizen science for visual classification of galaxy morphologies in HSC-SSP data—GALAXY CRUISE[1]—or other morphological studies using machine learning techniques will also lead us to the birthplace of morphology-$F_{\rm HI}$ relation.

[1]https://galaxycruise.mtk.nao.ac.jp/

Bibliography

Abazajian, K. N., Adelman-McCarthy, J. K., Agüeros, M. A., et al. 2009, The Astrophysical Journal Supplement Series, 182, 543, doi: 10.1088/0067-0049/182/2/543

Abraham, R. G., Tanvir, N. R., Santiago, B. X., et al. 1996, Monthly Notices of the Royal Astronomical Society, 279, L47, doi: 10.1093/mnras/279.3.L47

Abraham, R. G., van den Bergh, S., & Nair, P. 2003, The Astrophysical Journal, 588, 218, doi: 10.1086/373919

Ahumada, R. 2020, The Astrophysical Journal Supplement Series, 21

Aihara, H., Armstrong, R., Bickerton, S., et al. 2018, Publications of the Astronomical Society of Japan, 70, doi: 10.1093/pasj/psx081

Baldwin, J. A., Phillips, M. M., & Terlevich, R. 1981, Publications of the Astronomical Society of the Pacific, 93, 5, doi: 10.1086/130766

Balogh, M. L., Baldry, I. K., Nichol, R., et al. 2004, The Astrophysical Journal, 615, L101, doi: 10.1086/426079

Bamford, S. P., Nichol, R. C., Baldry, I. K., et al. 2009a, Monthly Notices of the Royal Astronomical Society, 393, 1324, doi: 10.1111/j.1365-2966.2008.14252.x

—. 2009b, Monthly Notices of the Royal Astronomical Society, 393, 1324, doi: 10.1111/j.1365-2966.2008.14252.x

Becker, R. H., White, R. L., & Helfand, D. J. 1995, The Astrophysical Journal, 450, 559, doi: 10.1086/176166

Bekki, K. 2009, Monthly Notices of the Royal Astronomical Society, 399, 2221, doi: 10.1111/j.1365-2966.2009.15431.x

Bernardi, M., Shankar, F., Hyde, J. B., et al. 2010, Monthly Notices of the Royal Astronomical Society, doi: 10.1111/j.1365-2966.2010.16425.x

Binney, J., & Tremaine, S. 1987, Galactic Dynamics

—. 2008, Galactic Dynamics, 2nd edn., Princeton Series in Astrophysics (Princeton: Princeton University Press)

Blanton, M. R., Schlegel, D. J., Strauss, M. A., et al. 2005, The Astronomical Journal, 129, 2562, doi: 10.1086/429803

Boselli, A., Eales, S., Cortese, L., & of the …, B. G. 2010, Publications of the …

Bothwell, M., Maiolino, R., Kennicutt, R., et al. 2013, Mon Not R Astron Soc, 433, 1425, doi: 10.1093/mnras/stt817

Brinchmann, J., Charlot, S., White, S., et al. 2004, Mon Not R Astron Soc, 351, 1151, doi: 10.1111/j.1365-2966.2004.07881.x

Brown, T., Catinella, B., Cortese, L., et al. 2015, Monthly Notices of the Royal Astronomical Society, 452, 2479, doi: 10.1093/mnras/stv1311

Buat, V. 2003, The Extinction in Galaxies. Analysis in the Ultraviolet and Far-Infrared Future Observations of the GALEX Satellite, 235

Bundy, K., Bershady, M. A., Law, D. R., et al. 2014, The Astrophysical Journal, 798, 7, doi: 10.1088/0004-637X/798/1/7

Butcher, H., & Oemler, Jr., A. 1984, The Astrophysical Journal, 285, 426, doi: 10.1086/162519

Calette, A. R., Avila-Reese, V., Rodrıguez-Puebla, A., Hernandez-Toledo, H., & Papastergis, E. 2018, 54, 443

Caon, N., Capaccioli, M., & D'Onofrio, M. 1993, Monthly Notices of the Royal Astronomical Society, 265, 1013, doi: 10.1093/mnras/265.4.1013

Catinella, B., Schiminovich, D., Kauffmann, G., et al. 2010, Monthly Notices of the Royal Astronomical Society, 403, 683, doi: 10.1111/j.1365-2966.2009.16180.x

Catinella, B., Schiminovich, D., Cortese, L., et al. 2013, Monthly Notices of the Royal Astronomical Society, 436, 34, doi: 10.1093/mnras/stt1417

Catinella, B., Saintonge, A., Janowiecki, S., et al. 2018, Monthly Notices of the Royal Astronomical Society, 476, 875, doi: 10.1093/mnras/sty089

Chabrier, G. 2003, Publications of the Astronomical Society of the Pacific, 115, 763, doi: 10.1086/376392

Chary, R., & Elbaz, D. 2001, The Astrophysical Journal, 556, 562, doi: 10.1086/321609

Chauke, P., van der Wel, A., Pacifici, C., et al. 2019, The Astrophysical Journal, 877, 48, doi: 10.3847/1538-4357/ab164d

Conselice, C. J. 2003, The Astrophysical Journal Supplement Series, 147, 1, doi: 10.1086/375001

—. 2014, Annual Review of Astronomy and Astrophysics, 52, 291, doi: 10.1146/annurev-astro-081913-040037

Conselice, C. J., Bershady, M. A., & Jangren, A. 2000, The Astrophysical Journal, 529, 886, doi: 10.1086/308300

Cook, R. H. W., Cortese, L., Catinella, B., & Robotham, A. S. G. 2019, arXiv:1909.10202 [astro-ph]. https://arxiv.org/abs/1909.10202

Cooper, M. C., Tremonti, C. A., Newman, J. A., & Zabludoff, A. I. 2008, 390, 245, doi: 10.1111/j.1365-2966.2008.13714.x

Cortese, L. 2012, Astronomy & Astrophysics, 543, A132, doi: 10.1051/0004-6361/201219443

Cortese, L., Catinella, B., Boissier, S., Boselli, A., & Heinis, S. 2011, Monthly Notices of the Royal Astronomical Society, 415, 1797, doi: 10.1111/j.1365-2966.2011.18822.x

Cortese, L., Catinella, B., & Smith, R. 2021, Publications of the Astronomical Society of Australia, 38, e035, doi: 10.1017/pasa.2021.18

Cox, T. J., Jonsson, P., Primack, J. R., & Somerville, R. S. 2006, Monthly Notices of the Royal Astronomical Society, 373, 1013, doi: 10.1111/j.1365-2966.2006.11107.x

Daddi, E., Cimatti, A., Renzini, A., et al. 2004, Astrophysical J, 617, 746, doi: 10.1086/425569

Daddi, E., Dannerbauer, H., Elbaz, D., et al. 2008, The Astrophysical Journal, 673, L21, doi: 10.1086/527377

Darg, D. W., Kaviraj, S., Lintott, C. J., et al. 2010, Monthly Notices of the Royal Astronomical Society, 401, 1552, doi: 10.1111/j.1365-2966.2009.15786.x

Davé, R., Finlator, K., & Oppenheimer, B. 2011, Mon Not R Astron Soc, 416, 1354, doi: 10.1111/j.1365-2966.2011.19132.x

—. 2012, Mon Not R Astron Soc, 421, 98, doi: 10.1111/j.1365-2966.2011.20148.x

Davé, R., Oppenheimer, B. D., & Sivanandam, S. 2008, Monthly Notices of the Royal Astronomical Society, 391, 110, doi: 10.1111/j.1365-2966.2008.13906.x

Davis, T. A., Young, L. M., Crocker, A. F., et al. 2014, Monthly Notices of the Royal Astronomical Society, 444, 3427, doi: 10.1093/mnras/stu570

de Vaucouleurs, G. 1959, Handbuch der Physik, 53, 275, doi: 10.1007/978-3-642-45932-0_7

de Vaucouleurs, G., de Vaucouleurs, A., Corwin, Jr., H. G., et al. 1991, Third Reference Catalogue of Bright Galaxies

Dekel, A., Birnboim, Y., Engel, G., Freundlich, J., & Nature, G. T. 2009, Nature, doi: 10.1038/nature07648

Deng, X.-F. 2013, Research in Astronomy and Astrophysics, 13, 651, doi: 10.1088/1674-4527/13/6/004

Dewdney, P., Hall, P., Schilizzi, R., & Lazio, T. 2009, Proceedings of the IEEE, 97, 1482, doi: 10.1109/JPROC.2009.2021005

Dickinson, H., Fortson, L., Lintott, C., et al. 2018, The Astrophysical Journal, 853, 194, doi: 10.3847/1538-4357/aaa250

Dokkum, P., Franx, M., Fabricant, D., Illingworth, G., & Kelson, D. 2000, doi: 10.1086/309402

Domínguez Sánchez, H., Huertas-Company, M., Bernardi, M., Tuccillo, D., & Fischer, J. L. 2018, Monthly Notices of the Royal Astronomical Society, 476, 3661, doi: 10.1093/mnras/sty338

D'Onofrio, M., Sciarratta, M., Cariddi, S., Marziani, P., & Chiosi, C. 2019, The Astrophysical Journal, 875, 103, doi: 10.3847/1538-4357/ab1134

Dressler, A. 1980, The Astrophysical Journal, 236, 351, doi: 10.1086/157753

Ellison, S., Simard, L., Cowan, N., et al. 2009, Mon Not R Astron Soc, 396, 1257, doi: 10.1111/j.1365-2966.2009.14817.x

Ellison, S. L., Mendel, T. J., Patton, D. R., & Scudder, J. M. 2013, Mon Not R Astron Soc, 435, 3627, doi: 10.1093/mnras/stt1562

Ellison, S. L., Patton, D. R., Simard, L., et al. 2010, Monthly Notices of the Royal Astronomical Society, 407, 1514, doi: 10.1111/j.1365-2966.2010.17076.x

Elmegreen, D. M., Kaufman, M., Brinks, E., Elmegreen, B. G., & Sundin, M. 1995, The Astrophysical Journal, 453, 100, doi: 10.1086/176374

Erb, D. K., Shapley, A. E., Pettini, M., et al. 2006, The Astrophysical Journal, 644, 813, doi: 10.1086/503623

Escala, A., & Larson, R. B. 2008, The Astrophysical Journal, 685, L31, doi: 10.1086/592271

Fabello, S., Kauffmann, G., Catinella, B., et al. 2011, arXiv:1104.0414 [astro-ph]. https://arxiv.org/abs/1104.0414

Ferrarese, L., Cote, P., Jordan, A., et al. 2006, The Astrophysical Journal Supplement Series, 164, 334, doi: 10.1086/501350

Finlator, K., & Davé, R. 2008, Mon Not R Astron Soc, 385, 2181, doi: 10.1111/j.1365-2966.2008.12991.x

Folkes, S., Ronen, S., Price, I., et al. 1999, Monthly Notices of the Royal Astronomical Society, 308, 459, doi: 10.1046/j.1365-8711.1999.02721.x

Gavazzi, G., Giovanelli, R., Haynes, M. P., et al. 2008, Astronomy & Astrophysics, 482, 43, doi: 10.1051/0004-6361:200809382

Genel, S., Vogelsberger, M., Springel, V., et al. 2014, Monthly Notices of the Royal Astronomical Society, 445, 175, doi: 10.1093/mnras/stu1654

Genzel, R., Schreiber, N., Rosario, D., et al. 2014, Astrophysical J, 796, 7, doi: 10.1088/0004-637X/796/1/7

George, K. 2017, Astronomy & Astrophysics, 598, A45, doi: 10.1051/0004-6361/201629667

Geréb, K., Catinella, B., Cortese, L., et al. 2016, Monthly Notices of the Royal Astronomical Society, 462, 382, doi: 10.1093/mnras/stw1675

Geréb, K., Janowiecki, S., Catinella, B., Cortese, L., & Kilborn, V. 2018, Monthly Notices of the Royal Astronomical Society, doi: 10.1093/mnras/sty214

Gomez, P. L., Nichol, R. C., Miller, C. J., et al. 2003, The Astrophysical Journal, 584, 210, doi: 10.1086/345593

Gonzalez, A. H., Zabludoff, A. I., & Zaritsky, D. 2005, The Astrophysical Journal, 618, 195, doi: 10.1086/425896

Goto, T., Yamauchi, C., Fujita, Y., et al. 2003, Monthly Notices of the Royal Astronomical Society, 346, 601, doi: 10.1046/j.1365-2966.2003.07114.x

Goulding, A. D., Matthaey, E., Greene, J. E., et al. 2017, The Astrophysical Journal, 843, 135, doi: 10.3847/1538-4357/aa755b

Graham, A. W., & Guzmn, R. 2003, The Astronomical Journal, 125, 2936, doi: 10.1086/374992

Gunn, J. E., & Gott, III, J. R. 1972, The Astrophysical Journal, 176, 1, doi: 10.1086/151605

Guo, R., Hao, C.-N., Xia, X., et al. 2020, The Astrophysical Journal, 897, 162, doi: 10.3847/1538-4357/ab9b75

Gusev, A. S., Sakhibov, F., & Efremov, Y. N. 2015, Astronomische Nachrichten, 336, 401, doi: 10.1002/asna.201512170

Hart, R. E., Bamford, S. P., Willett, K. W., et al. 2016, Monthly Notices of the Royal Astronomical Society, 461, 3663, doi: 10.1093/mnras/stw1588

Hart, R. E., Bamford, S. P., Hayes, W. B., et al. 2017, Monthly Notices of the Royal Astronomical Society, 472, 2263, doi: 10.1093/mnras/stx2137

Haynes, M. P., & Giovanelli, R. 1984, The Astronomical Journal, 89, 758, doi: 10.1086/113573

Haynes, M. P., Giovanelli, R., Kent, B. R., et al. 2018, Astrophysical J, 861, 49, doi: 10.3847/1538-4357/aac956

Hayward, C. C., Narayanan, D., Kereš, D., et al. 2013, Monthly Notices of the Royal Astronomical Society, 428, 2529, doi: 10.1093/mnras/sts222

Healy, J., Blyth, S.-L., Elson, E., et al. 2019, Monthly Notices of the Royal Astronomical Society, 487, 4901, doi: 10.1093/mnras/stz1555

Hernández-Toledo, H. M., Vázquez-Mata, J. A., Martínez-Vázquez, L. A., et al. 2008, The Astronomical Journal, 136, 2115, doi: 10.1088/0004-6256/136/5/2115

Hopkins, A., & Beacom, J. 2006, Astrophysical J, 651, 142, doi: 10.1086/506610

Hopkins, P. F., Hernquist, L., Cox, T. J., & Kereš, D. 2008, The Astrophysical Journal Supplement Series, 175, 356, doi: 10.1086/524362

Hubble, E. 1958, The Realm of the Nebulae

Hubble, E. P. 1936, Realm of the Nebulae

Hughes, T. M., Cortese, L., Boselli, A., Gavazzi, G., & Davies, J. I. 2013, Astronomy & Astrophysics, 550, A115, doi: 10.1051/0004-6361/201218822

Ichikawa, T., Suzuki, R., Tokoku, C., et al. 2006, in SPIE Astronomical Telescopes + Instrumentation, ed. I. S. McLean & M. Iye, Orlando, Florida , USA, 626916, doi: 10.1117/12.670078

Irwin, J. A. 1994, The Astrophysical Journal, 429, 618, doi: 10.1086/174349

Janowiecki, S., Catinella, B., & Cortese, L. 2019, 233, 429.04

Jian, H.-Y., Lin, L., & Chiueh, T. 2012, The Astrophysical Journal, 754, 26, doi: 10.1088/0004-637X/754/1/26

Jones, M. G., Haynes, M. P., Giovanelli, R., & Papastergis, E. 2016, Monthly Notices of the Royal Astronomical Society, 455, 1574, doi: 10.1093/mnras/stv2394

Kacprzak, G. G., Yuan, T., Nanayakkara, T., et al. 2015, 802, L26, doi: 10.1088/2041-8205/802/2/L26

Kauffmann, G., Heckman, T. M., Tremonti, C., et al. 2003, Monthly Notices of the Royal Astronomical Society, 346, 1055, doi: 10.1111/j.1365-2966.2003.07154.x

Kawata, D., & Mulchaey, J. S. 2008, The Astrophysical Journal, 672, L103, doi: 10.1086/526544

Kazantzidis, S., Bullock, J. S., Zentner, A. R., Kravtsov, A. V., & Moustakas, L. A. 2008, The Astrophysical Journal, 688, 254, doi: 10.1086/591958

Kennicutt, J. 1998, Annual Review of Astronomy and Astrophysics, 36, 189, doi: 10.1146/annurev.astro.36.1.189

Kennicutt, R. C., & Evans, N. J. 2012, Annual Review of Astronomy and Astrophysics, 50, 531, doi: 10.1146/annurev-astro-081811-125610

Kennicutt, Jr., R. C. 1992, The Astrophysical Journal, 388, 310, doi: 10.1086/171154

Kewley, L., Maier, C., Yabe, K., et al. 2013, Astrophysical J Lett, 774, L10, doi: 10.1088/2041-8205/774/1/L10

Kormendy, J., Fisher, D. B., Cornell, M. E., & Bender, R. 2009, The Astrophysical Journal Supplement Series, 182, 216, doi: 10.1088/0067-0049/182/1/216

Koyama, S., Koyama, Y., Yamashita, T., et al. 2019, The Astrophysical Journal, 874, 142, doi: 10.3847/1538-4357/ab0e75

Koyama, Y., Kodama, T., Tadaki, K.-i., et al. 2014, Astrophysical J, 789, 18, doi: 10.1088/0004-637X/789/1/18

—. 2013, Mon Not R Astron Soc, 428, 1551, doi: 10.1093/mnras/sts133

Koyama, Y., Kodama, T., Hayashi, M., et al. 2015, Mon Not R Astron Soc, 453, 879, doi: 10.1093/mnras/stv1599

Kulas, K., Ian, M., Shapley, A., et al. 2013, Astrophysical J, 774, 130, doi: 10.1088/0004-637X/774/2/130

Lange, R., Driver, S. P., Robotham, A. S. G., et al. 2015, Monthly Notices of the Royal Astronomical Society, 447, 2603, doi: 10.1093/mnras/stu2467

Larson, R. B. 1985, Monthly Notices of the Royal Astronomical Society, 214, 379, doi: 10.1093/mnras/214.3.379

Leroy, A. K., Walter, F., Brinks, E., et al. 2008, The Astronomical Journal, 136, 2782, doi: 10.1088/0004-6256/136/6/2782

Li, I. H., Glazebrook, K., Gilbank, D., et al. 2011, Monthly Notices of the Royal Astronomical Society, 411, 1869, doi: 10.1111/j.1365-2966.2010.17816.x

Lintott, C. J., Schawinski, K., Slosar, A., et al. 2008, Monthly Notices of the Royal Astronomical Society, 389, 1179, doi: 10.1111/j.1365-2966.2008.13689.x

Lotz, J. M., Jonsson, P., Cox, T. J., & Primack, J. R. 2008a, Monthly Notices of the Royal Astronomical Society, 391, 1137, doi: 10.1111/j.1365-2966.2008.14004.x

Lotz, J. M., Primack, J., & Madau, P. 2004, The Astronomical Journal, 128, 163, doi: 10.1086/421849

Lotz, J. M., Davis, M., Faber, S. M., et al. 2008b, The Astrophysical Journal, 672, 177, doi: 10.1086/523659

Maier, C., Hayashi, M., Ziegler, B. L., & Kodama, T. 2019, Astronomy & Astrophysics, 626, A14, doi: 10.1051/0004-6361/201935522

Maiolino, R., Nagao, T., Grazian, A., & & …, C. F. 2008, Astronomy & …, doi: 10.1051/0004-6361:200809678

Malumuth, E. M., & Richstone, D. O. 1984, The Astrophysical Journal, 276, 413, doi: 10.1086/161626

Mannucci, F., Cresci, G., Maiolino, R., Marconi, A., & Gnerucci, A. 2010, Mon Not R Astron Soc, 408, 2115, doi: 10.1111/j.1365-2966.2010.17291.x

Marinacci, F., Vogelsberger, M., Pakmor, R., et al. 2018, Monthly Notices of the Royal Astronomical Society, doi: 10.1093/mnras/sty2206

Martig, M., Bournaud, F., Teyssier, R., & Dekel, A. 2009, The Astrophysical Journal, 707, 250, doi: 10.1088/0004-637X/707/1/250

Martig, M., Crocker, A. F., Bournaud, F., et al. 2013, Monthly Notices of the Royal Astronomical Society, 432, 1914, doi: 10.1093/mnras/sts594

Masters, K. L., Lintott, C. J., Hart, R. E., et al. 2019, Monthly Notices of the Royal Astronomical Society, 487, 1808, doi: 10.1093/mnras/stz1153

McCarthy, I. G., Frenk, C. S., Font, A. S., et al. 2008, Monthly Notices of the Royal Astronomical Society, 383, 593, doi: 10.1111/j.1365-2966.2007.12577.x

Meyer, M., Robotham, A., Obreschkow, D., et al. 2017, Publications of the Astronomical Society of Australia, 34, e052, doi: 10.1017/pasa.2017.31

Mihos, J. C., & Hernquist, L. 1996, The Astrophysical Journal, 464, 641, doi: 10.1086/177353

Miyazaki, S., Komiyama, Y., Sekiguchi, M., et al. 2002, Publications of the Astronomical Society of Japan, 54, 833, doi: 10.1093/pasj/54.6.833

Moore, B., Lake, G., & Katz, N. 1998, The Astrophysical Journal, 495, 139, doi: 10.1086/305264

Morgan, W. W. 1958, Publications of the Astronomical Society of the Pacific, 70, 364, doi: 10.1086/127243

—. 1962, The Astrophysical Journal, 135, 1, doi: 10.1086/147243

Morrissey, P., Schiminovich, D., Barlow, T. A., et al. 2005, The Astrophysical Journal Letters, 619, L7, doi: 10.1086/424734

Murante, G., Arnaboldi, M., Gerhard, O., et al. 2004, The Astrophysical Journal, 607, L83, doi: 10.1086/421348

Naiman, J. P., Pillepich, A., Springel, V., et al. 2018, Monthly Notices of the Royal Astronomical Society, 477, 1206, doi: 10.1093/mnras/sty618

Namiki, S. V., Koyama, Y., Koyama, S., et al. 2021, The Astrophysical Journal, 918, 68, doi: 10.3847/1538-4357/abfe08

Namiki, S. V., Koyama, Y., Hayashi, M., et al. 2019, The Astrophysical Journal, 877, 118, doi: 10.3847/1538-4357/ab1b6c

Nelson, D., Pillepich, A., Genel, S., et al. 2015a, Astronomy and Computing, 13, 12, doi: 10.1016/j.ascom.2015.09.003

—. 2015b, Astronomy and Computing, 13, 12, doi: 10.1016/j.ascom.2015.09.003

Nelson, D., Pillepich, A., Springel, V., et al. 2018, Monthly Notices of the Royal Astronomical Society, 475, 624, doi: 10.1093/mnras/stx3040

Nelson, D., Springel, V., Pillepich, A., et al. 2019, Computational Astrophysics and Cosmology, 6, 2, doi: 10.1186/s40668-019-0028-x

Noll, S., Burgarella, D., Giovannoli, E., et al. 2009, Astronomy & Astrophysics, 507, 1793, doi: 10.1051/0004-6361/200912497

Onodera, M., Carollo, C., Lilly, S., & Astrophysical …, R. A. 2016, The Astrophysical …, 822, 42, doi: 10.3847/0004-637X/822/1/42

Oswalt, T. D., & Keel, W. C., eds. 2013, Planets, Stars and Stellar Systems (Dordrecht: Springer Netherlands), doi: 10.1007/978-94-007-5609-0

Pandya, V., Brennan, R., Somerville, R. S., et al. 2017, Monthly Notices of the Royal Astronomical Society, 472, 2054, doi: 10.1093/mnras/stx2027

Pawlik, M. M., Wild, V., Walcher, C. J., et al. 2016, Monthly Notices of the Royal Astronomical Society, 456, 3032, doi: 10.1093/mnras/stv2878

Peng, Y.-j., Lilly, S., Kovač, K., et al. 2010, Astrophysical J, 721, 193, doi: 10.1088/0004-637X/721/1/193

Pettini, M., & Pagel, B. 2004, Mon Not R Astron Soc, 348, L59, doi: 10.1111/j.1365-2966.2004.07591.x

Pillepich, A., Nelson, D., Hernquist, L., et al. 2018, Monthly Notices of the Royal Astronomical Society, 475, 648, doi: 10.1093/mnras/stx3112

Quinn, P. J., Hernquist, L., & Fullagar, D. P. 1993, The Astrophysical Journal, 403, 74, doi: 10.1086/172184

Renaud, F., Bournaud, F., Kraljic, K., & Duc, P.-A. 2014, Monthly Notices of the Royal Astronomical Society: Letters, 442, L33, doi: 10.1093/mnrasl/slu050

Renzini, A., & Peng, Y.-j. 2015, The Astrophysical Journal, 801, L29, doi: 10.1088/2041-8205/801/2/L29

Rix, H.-W., & Zaritsky, D. 1995, The Astrophysical Journal, 447, 82, doi: 10.1086/175858

Roberts, M. S. 1963, Annual Review of Astronomy and Astrophysics, vol. 1, p.149, 1, 149, doi: 10.1146/annurev.aa.01.090163.001053

—. 1969, The Astronomical Journal, 74, 859, doi: 10.1086/110874

Roberts, M. S., & Haynes, M. P. 1994, Annual Review of Astronomy and Astrophysics, 32, 115, doi: 10.1146/annurev.aa.32.090194.000555

Robotham, A. S. G., Taranu, D. S., Tobar, R., Moffett, A., & Driver, S. P. 2017, Monthly Notices of the Royal Astronomical Society, 466, 1513, doi: 10.1093/mnras/stw3039

Rodriguez-Gomez, V., Genel, S., Vogelsberger, M., et al. 2015, Monthly Notices of the Royal Astronomical Society, 449, 49, doi: 10.1093/mnras/stv264

Saintonge, A., Kauffmann, G., Wang, J., et al. 2011, Monthly Notices of the Royal Astronomical Society, 415, 61, doi: 10.1111/j.1365-2966.2011.18823.x

Salim, S., Boquien, M., & Lee, J. 2018

Salim, S., Lee, J., Janowiecki, S., et al. 2016, Astrophysical J Suppl Ser, 227, 2, doi: 10.3847/0067-0049/227/1/2

Salmon, B., Papovich, C., Finkelstein, S. L., et al. 2015, The Astrophysical Journal, 799, 183, doi: 10.1088/0004-637X/799/2/183

Salpeter, E. E. 1955, The Astrophysical Journal, 121, 161, doi: 10.1086/145971

Sanders, D. B., Soifer, B. T., Elias, J. H., et al. 1988, The Astrophysical Journal, 325, 74, doi: 10.1086/165983

Sanders, R. L., Shapley, A. E., Kriek, M., et al. 2018, The Astrophysical Journal, 858, 99, doi: 10.3847/1538-4357/aabcbd

Santini, P., Fontana, A., Castellano, M., et al. 2017, The Astrophysical Journal, 847, 76, doi: 10.3847/1538-4357/aa8874

Saunders, W., Sutherland, W. J., Maddox, S. J., et al. 2000, Monthly Notices of the Royal Astronomical Society, 317, 55, doi: 10.1046/j.1365-8711.2000.03528.x

Schawinski, K., Urry, C. M., Simmons, B. D., et al. 2014, Monthly Notices of the Royal Astronomical Society, 440, 889, doi: 10.1093/mnras/stu327

Schruba, A., Leroy, A. K., Walter, F., et al. 2011, The Astronomical Journal, 142, 37, doi: 10.1088/0004-6256/142/2/37

Schweizer, F. 1982, The Astrophysical Journal, 252, 455, doi: 10.1086/159573

Seifert, W., Appenzeller, I., Baumeister, H., et al. 2003, in Astronomical Telescopes and Instrumentation, ed. M. Iye & A. F. M. Moorwood, Waikoloa, Hawai'i, United States, 962, doi: 10.1117/12.459494

Sérsic, J. L. 1963, Boletin de la Asociacion Argentina de Astronomia La Plata Argentina, 6, 41

Shimakawa, R., Kodama, T., & of . . . , T. K. 2015, Monthly Notices of . . . , doi: 10.1093/mnras/stv051

Shimasaku, K., Fukugita, M., Doi, M., et al. 2001, The Astronomical Journal, 122, 1238, doi: 10.1086/322094

Sijacki, D., Vogelsberger, M., Genel, S., et al. 2015, Monthly Notices of the Royal Astronomical Society, 452, 575, doi: 10.1093/mnras/stv1340

Silk, J., & Mamon, G. A. 2012, Research in Astronomy and Astrophysics, 12, 917, doi: 10.1088/1674-4527/12/8/004

Skrutskie, M. F., Cutri, R. M., Stiening, R., et al. 2006, The Astronomical Journal, 131, 1163, doi: 10.1086/498708

Smethurst, R. J., Lintott, C. J., Bamford, S. P., et al. 2017, Monthly Notices of the Royal Astronomical Society, 469, 3670, doi: 10.1093/mnras/stx973

Snyder, G. F., Torrey, P., Lotz, J. M., et al. 2015, Monthly Notices of the Royal Astronomical Society, 454, 1886, doi: 10.1093/mnras/stv2078

Sobral, D., Best, P., Matsuda, Y., et al. 2012, Mon Not R Astron Soc, 420, 1926, doi: 10.1111/j.1365-2966.2011.19977.x

Sobral, D., Smail, I., Best, P., et al. 2013, Mon Not R Astron Soc, 428, 1128, doi: 10.1093/mnras/sts096

Solanes, J. M. 2001, arXiv:astro-ph/0106207. https://arxiv.org/abs/astro-ph/0106207

Sparre, M., Whittingham, J., Damle, M., et al. 2021, Monthly Notices of the Royal Astronomical Society, stab3171, doi: 10.1093/mnras/stab3171

Springel, V. 2010, Monthly Notices of the Royal Astronomical Society, 401, 791, doi: 10.1111/j.1365-2966.2009.15715.x

Springel, V., Pakmor, R., Pillepich, A., et al. 2018, Monthly Notices of the Royal Astronomical Society, 475, 676, doi: 10.1093/mnras/stx3304

Stinson, G. S., Bailin, J., Couchman, H., et al. 2010, Monthly Notices of the Royal Astronomical Society, 408, 812, doi: 10.1111/j.1365-2966.2010.17187.x

Stott, J. P., Sobral, D., Bower, R., et al. 2013, 436, 1130, doi: 10.1093/mnras/stt1641

Strateva, I., Ivezić, Ž., Knapp, G. R., et al. 2001, The Astronomical Journal, 122, 1861, doi: 10.1086/323301

Suzuki, R., Tokoku, C., Ichikawa, T., et al. 2008, Publ Astron Soc Jpn, 60, 1347, doi: 10.1093/pasj/60.6.1347

Tacconi, L. J., Genzel, R., Smail, I., et al. 2008, The Astrophysical Journal, 680, 246, doi: 10.1086/587168

Tadaki, K.-i., Kodama, T., Tanaka, I., et al. 2013, Astrophysical J, 778, 114, doi: 10.1088/0004-637X/778/2/114

Takamiya, M. 1999, The Astrophysical Journal Supplement Series, 122, 109, doi: 10.1086/313216

Tanaka, I., Breuck, D. C., & of the …, K. J. 2011, Publications of the …

Tanaka, M., Goto, T., Okamura, S., Shimasaku, K., & Brinkmann, J. 2004, The Astronomical Journal, 128, 2677, doi: 10.1086/425529

Tempel, E., Saar, E., Liivamägi, L. J., et al. 2011, Astronomy & Astrophysics, 529, A53, doi: 10.1051/0004-6361/201016196

Tomczak, A. R., Quadri, R. F., Tran, K.-V. H., et al. 2016, The Astrophysical Journal, 817, 118, doi: 10.3847/0004-637X/817/2/118

Toomre, A. 1964, The Astrophysical Journal, 139, 1217, doi: 10.1086/147861

—. 1977, Annual Review of Astronomy and Astrophysics, 15, 437, doi: 10.1146/annurev.aa.15.090177.002253

Torrey, P., Cox, T., Kewley, L., & Hernquist, L. 2012, 746, 108, doi: 10.1088/0004-637X/746/1/108

Torrey, P., Snyder, G. F., Vogelsberger, M., et al. 2015, Monthly Notices of the Royal Astronomical Society, 447, 2753, doi: 10.1093/mnras/stu2592

Toth, G., & Ostriker, J. P. 1992, The Astrophysical Journal, 389, 5, doi: 10.1086/171185

Tran, K.-V. H., Moustakas, J., Gonzalez, A. H., et al. 2008, The Astrophysical Journal, 683, L17, doi: 10.1086/591422

Tran, K.-V. H., Nanayakkara, T., Yuan, T., et al. 2015, The Astrophysical Journal, 811, 28, doi: 10.1088/0004-637X/811/1/28

Tremonti, C. A., Heckman, T. M., Kauffmann, G., et al. 2004, Astrophysical J, 613, 898, doi: 10.1086/423264

Troncoso, P., Maiolino, R., Sommariva, V., et al. 2014, Astron Astrophys, 563, A58, doi: 10.1051/0004-6361/201322099

Tumlinson, J., Peeples, M., & Werk, J. 2016, Annu Rev Astron Astr, 55, 1, doi: 10.1146/annurev-astro-091916-055240

Valentino, F., Daddi, E., Strazzullo, V., et al. 2015, Astrophysical J, 801, 132, doi: 10.1088/0004-637X/801/2/132

Velazquez, H., & White, S. D. M. 1999, Monthly Notices of the Royal Astronomical Society, 304, 254, doi: 10.1046/j.1365-8711.1999.02354.x

Villar, V., Gallego, J., Pérez-González, P. G., et al. 2008, The Astrophysical Journal, 677, 169, doi: 10.1086/528942

Vogelsberger, M., Genel, S., Springel, V., et al. 2014a, Monthly Notices of the Royal Astronomical Society, 444, 1518, doi: 10.1093/mnras/stu1536

—. 2014b, Nature, 509, 177, doi: 10.1038/nature13316

Vulcani, B., Poggianti, B. M., Finn, R. A., et al. 2010, The Astrophysical Journal, 710, L1, doi: 10.1088/2041-8205/710/1/L1

Walter, F., Brinks, E., de Blok, W. J. G., et al. 2008, The Astronomical Journal, 136, 2563, doi: 10.1088/0004-6256/136/6/2563

Wang, L.-L., Luo, A.-L., Shen, S.-Y., et al. 2018, Monthly Notices of the Royal Astronomical Society, 474, 1873, doi: 10.1093/mnras/stx2798

Whitaker, K., Franx, M., Leja, J., et al. 2014, Astrophysical J, 795, 104, doi: 10.1088/0004-637X/795/2/104

Whitmore, B. C., & Gilmore, D. M. 1991, The Astrophysical Journal, 367, 64, doi: 10.1086/169602

Willett, K. W., Lintott, C. J., Bamford, S. P., et al. 2013, Monthly Notices of the Royal Astronomical Society, 435, 2835, doi: 10.1093/mnras/stt1458

Willman, B., Governato, F., Wadsley, J., & Quinn, T. 2004, Monthly Notices of the Royal Astronomical Society, 355, 159, doi: 10.1111/j.1365-2966.2004.08312.x

Wilman, D. J., & Erwin, P. 2012, The Astrophysical Journal, 746, 160, doi: 10.1088/0004-637X/746/2/160

Wilman, D. J., Oemler, A., Mulchaey, J. S., et al. 2009, The Astrophysical Journal, 692, 298, doi: 10.1088/0004-637X/692/1/298

Wright, E. L., Eisenhardt, P. R. M., Mainzer, A. K., et al. 2010, The Astronomical Journal, 140, 1868, doi: 10.1088/0004-6256/140/6/1868

Wu, P.-F., Zahid, H., Hwang, H., & Geller, M. 2017, doi: 10.1093/mnras/stx597

Yahya, S., Bull, P., Santos, M. G., et al. 2015, Monthly Notices of the Royal Astronomical Society, 450, 2251, doi: 10.1093/mnras/stv695

Yang, X., Mo, H. J., van den Bosch, F. C., et al. 2007, The Astrophysical Journal, 671, 153, doi: 10.1086/522027

York, D. G., Adelman, J., Anderson, Jr., J. E., et al. 2000, The Astronomical Journal, 120, 1579, doi: 10.1086/301513

Yoshikawa, T., Akiyama, M., & Astrophysical …, K. M. 2010, The Astrophysical …, 718, 112, doi: 10.1088/0004-637X/718/1/112

Young, L. M., Bureau, M., Davis, T. A., et al. 2011, Monthly Notices of the Royal Astronomical Society, 414, 940, doi: 10.1111/j.1365-2966.2011.18561.x

Zahid, H., Kashino, D., Silverman, J., et al. 2014, Astrophysical J, 792, 75, doi: 10.1088/0004-637X/792/1/75

A

Stacked spectra in Sec. 3 and 4.

We summarize radio spectra stacked in Sec. 3.2, 4.1, 4.2, and 4.3. Here we note that we show the spectra stacked with the weight of $(1+z)^2/D_L(z)^2 M_*$. The $1-\sigma$ error drawn here is calculated from the *rms* of individual ALFALFA spectra (see Sec.3.1). However, we conduct the bootstrap analysis to include the sampling errors. We show the average gas fraction ($F_{\rm HI}$) and signal-to-noise ratio (S/N) determined by the bootstrap method in the upper right of each panel.

A.1 Stacking of all galaxies

Firstly, we show the spectra stacked in Sec. 3.2. We divide our 'star-forming' sample by M_* and SFR ($\Delta M_* = \Delta SFR = 0.5$ dex). The stacking analysis is performed for the bins with more than nine objects (Figure 3.2). Figure A.1–A.4 show our result.

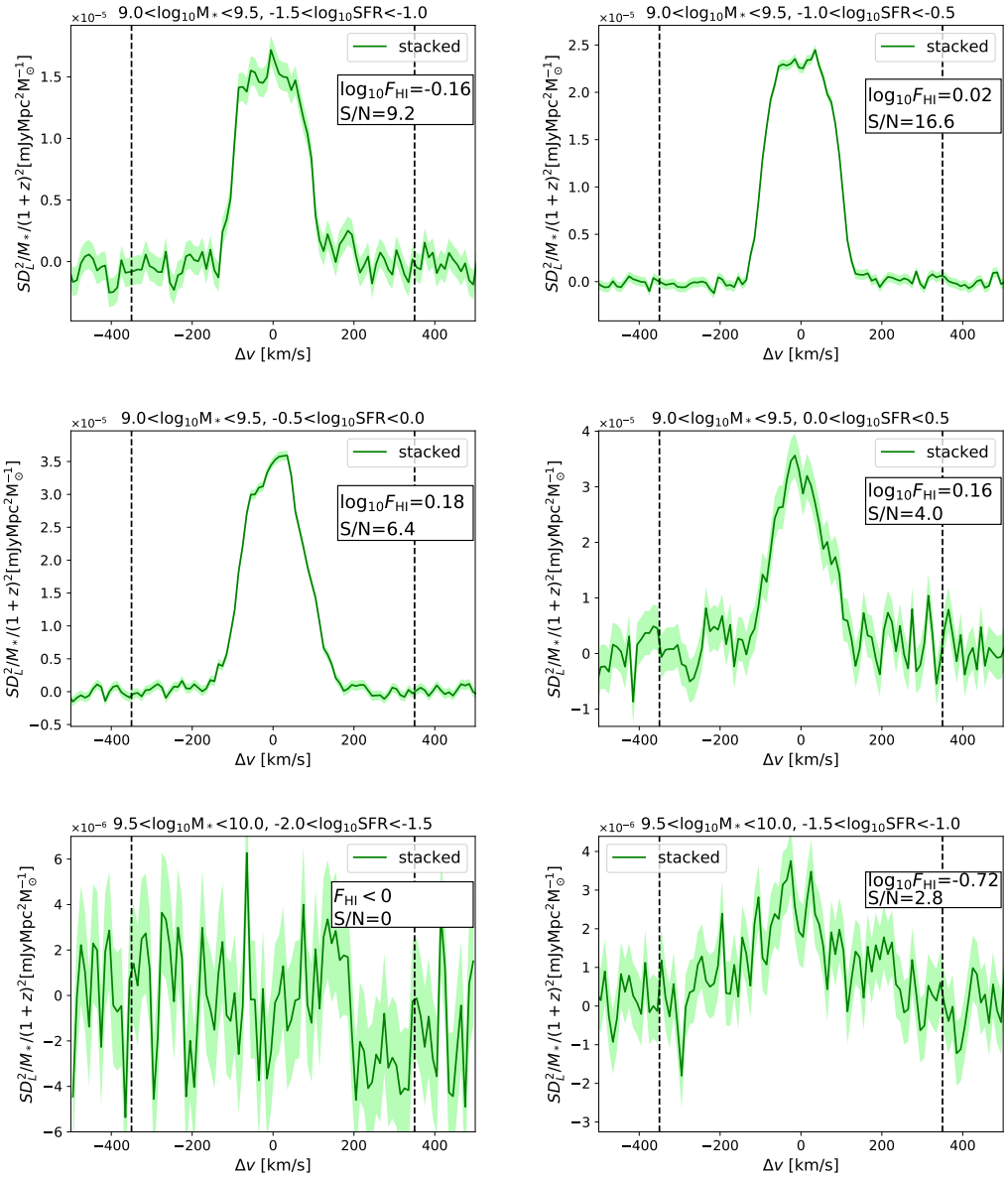

Figure A.1: A part of stacked H I spectra in Sec. 3.1. We write the M_* and *SFR* range on the top of each panel. The solid green line is the average spectra, and the shaded region shows $1-\sigma$ error derived from *rms* of ALFALFA spectra. Vertical dashed lines are written at ±350 km/s, between which the flux is summed up to calculate the gas fraction ($F_{\rm HI}$). We also show the average $F_{\rm HI}$ and S/N derived from our bootstrap analysis on the upper right. In the left bottom panel, the average $F_{\rm HI}$ has a minus value so that we cannot calculate $\log_{10} F_{\rm HI}$ and S/N.

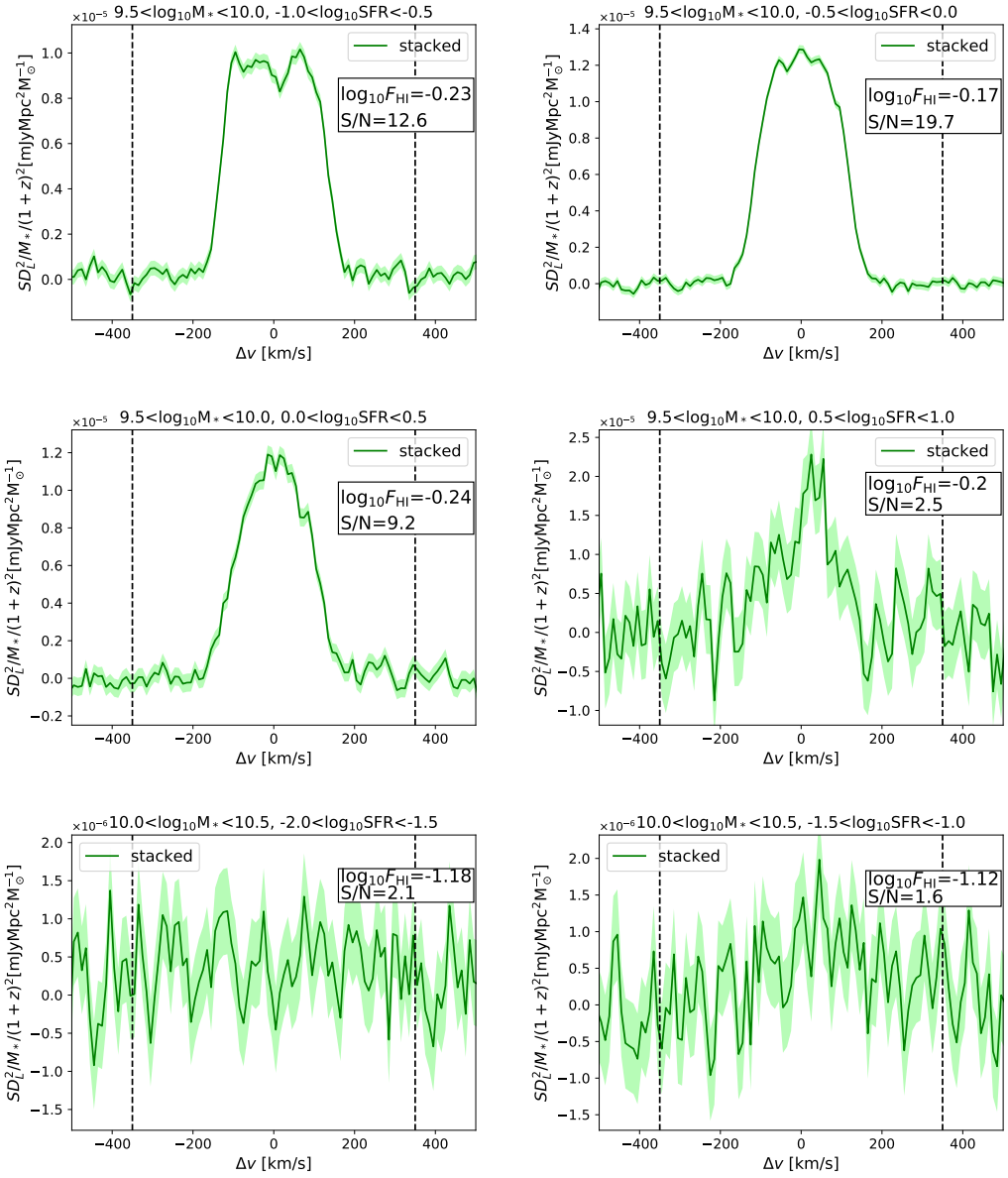

Figure A.2: Same figure as Figure A.1.

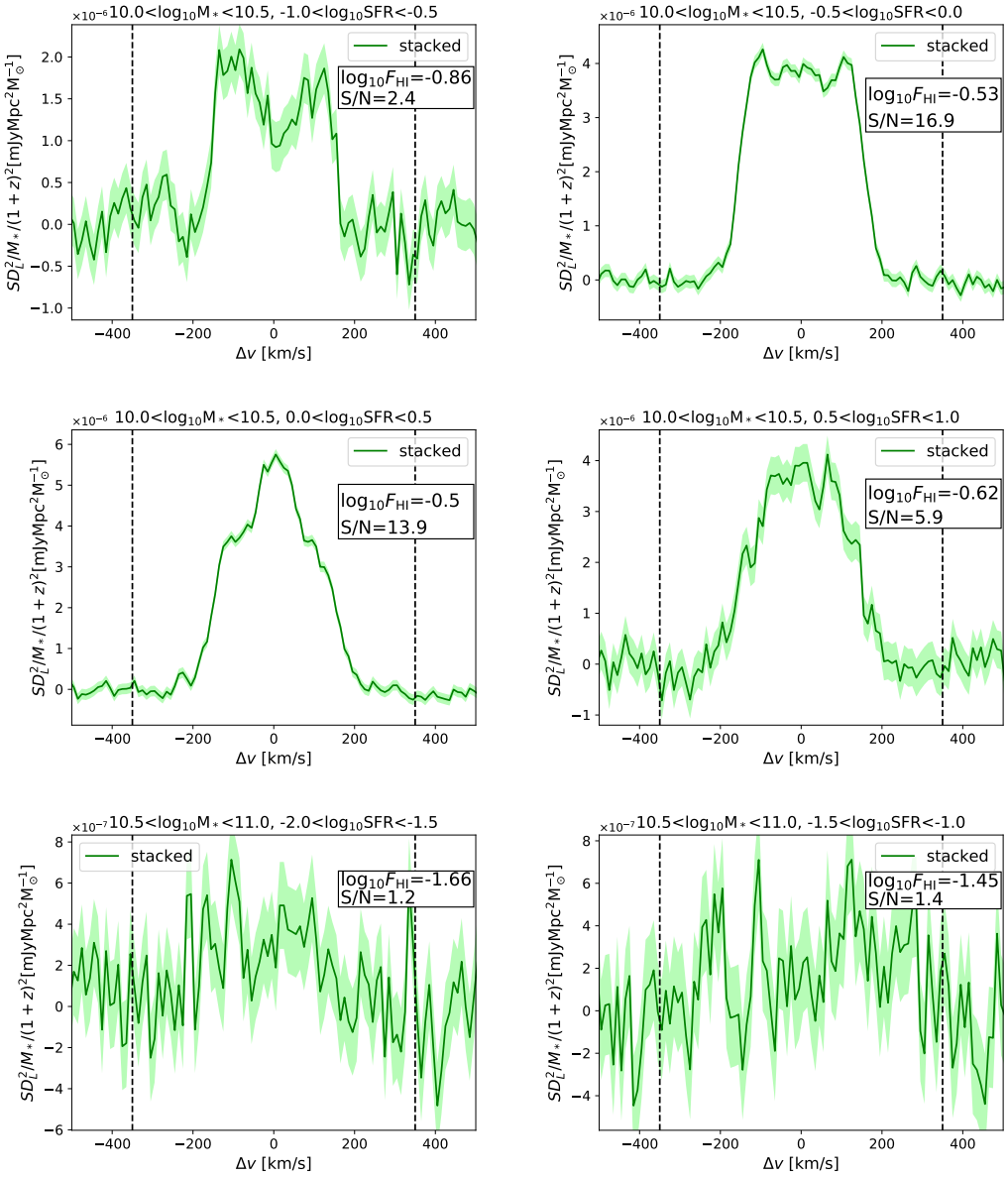

Figure A.3: Same figure as Figure A.1.

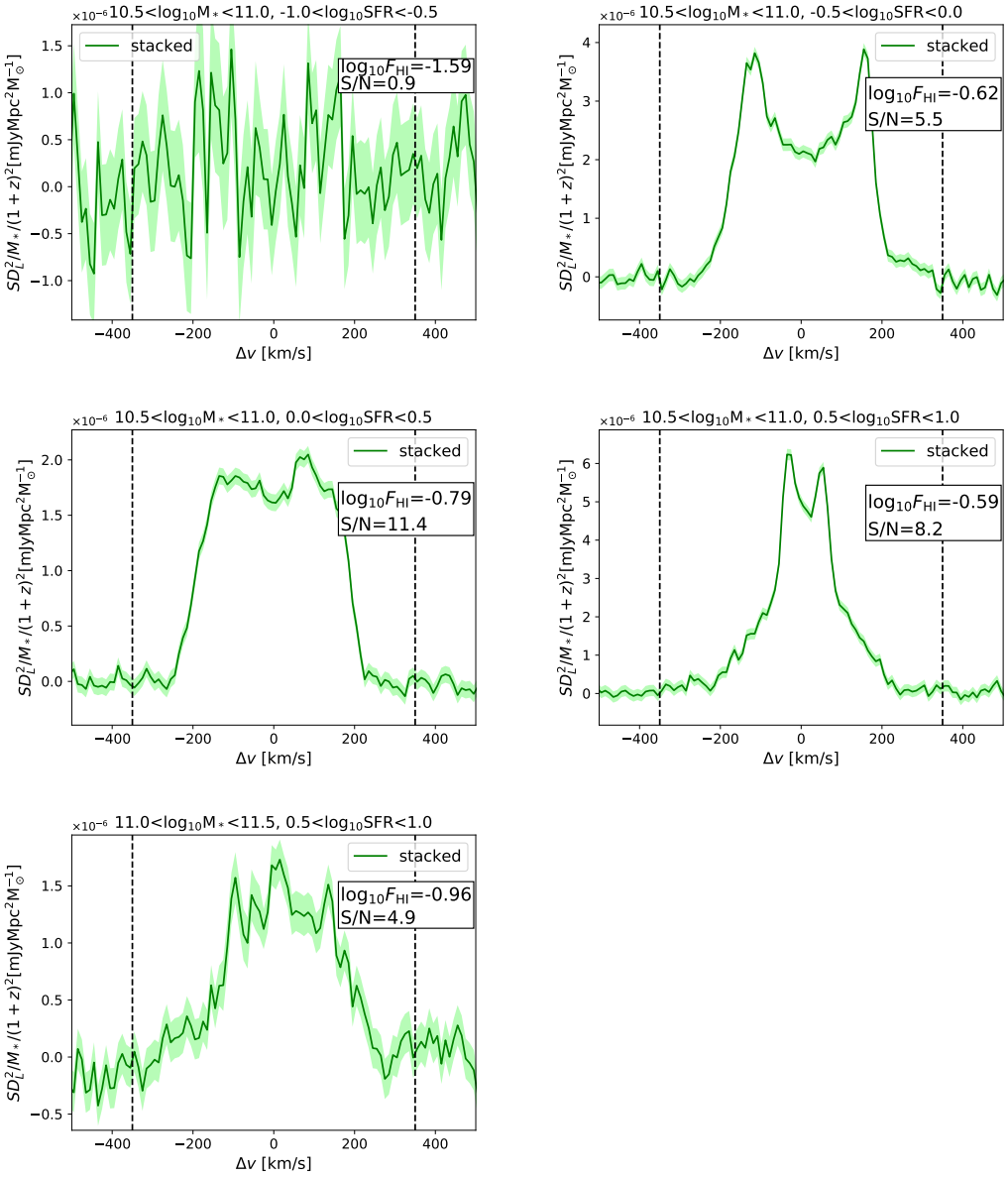

Figure A.4: Same figure as Figure A.1.

A.2 Stacking of early- and late-type galaxies

Secondly, we show the stacked spectra of early- and late-type galaxies in Sec.4.1. We choose the 'early-type' and 'late-type' galaxies by their Sérsic index n and further divide them by M_* and SFR ($\Delta M_* = \Delta SFR = 0.5$ dex). The stacking analysis is performed for the bins with more than nine objects (Figure 4.1). Figure A.5–A.7 show stacked spectra of early-type galaxies and A.8–A.9 show those of late-type galaxies.

A.3 Stacking of bulge and disk galaxies

Thirdly, we show the stacked spectra of bulge and disk galaxies in Sec.4.2. We choose the 'bulge' and 'disk' galaxies by their concentration index C and further divide them by M_* and SFR ($\Delta M_* = \Delta SFR = 0.5$ dex). The stacking analysis is performed for the bins with more than nine objects (Figure 4.3). Figure A.10–A.12 show stacked spectra of bulge galaxies and A.13–A.15 show those of disk galaxies.

A.4 Stacking of smooth and non-smooth galaxies

Finally, we show the stacked spectra of smooth and non-smooth galaxies in Sec.4.3. We choose the 'smooth' and 'non-smooth' galaxies by their debiased vote fraction and further divide them by M_* and SFR ($\Delta M_* = \Delta SFR = 0.5$ dex). The stacking analysis is performed for the bins with more than nine objects (Figure 4.3). Figure A.16–A.18 show stacked spectra of smooth galaxies and A.19–A.20 show those of non-smooth galaxies.

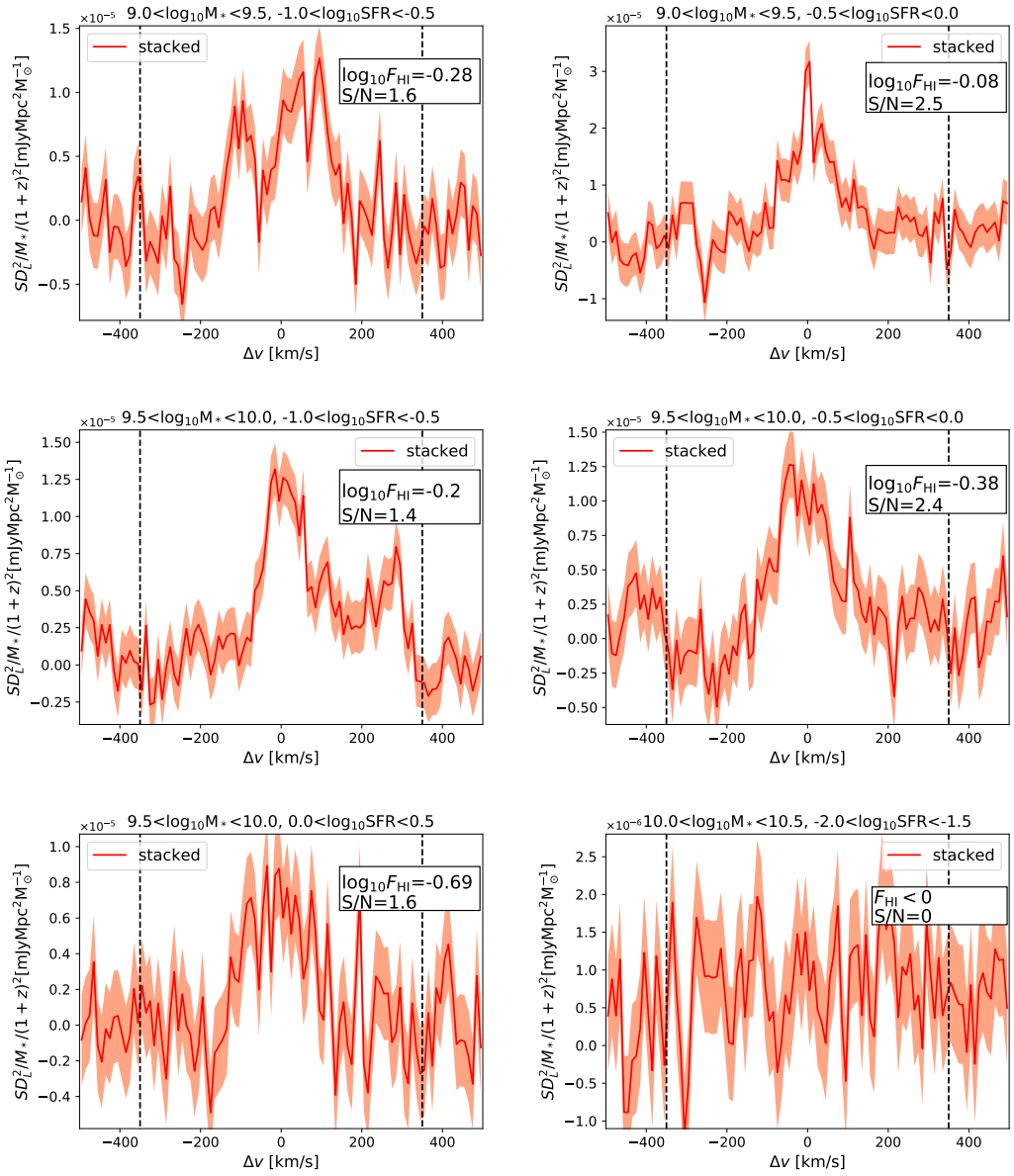

Figure A.5: A part of stacked H I spectra for early-type galaxies in Sec. 4.1. We write the M_* and *SFR* range on the top of each panel. The solid red line is the average spectra, and the shaded region shows $1-\sigma$ error derived from *rms* of ALFALFA spectra. Vertical dashed lines, $F_{\rm HI}$, and S/N are the same as Figure A.1.

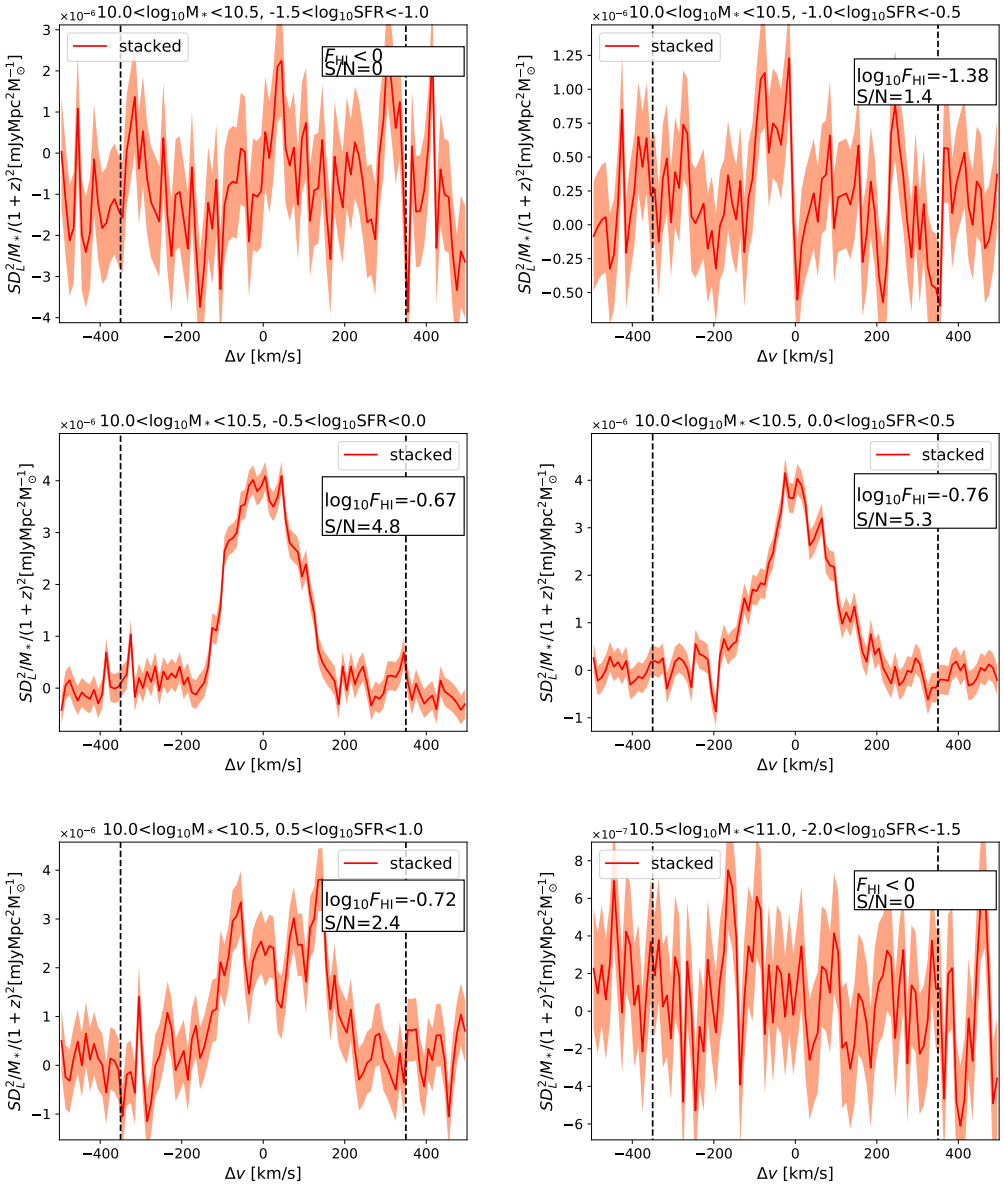

Figure A.6: Same figure as Figure A.5.

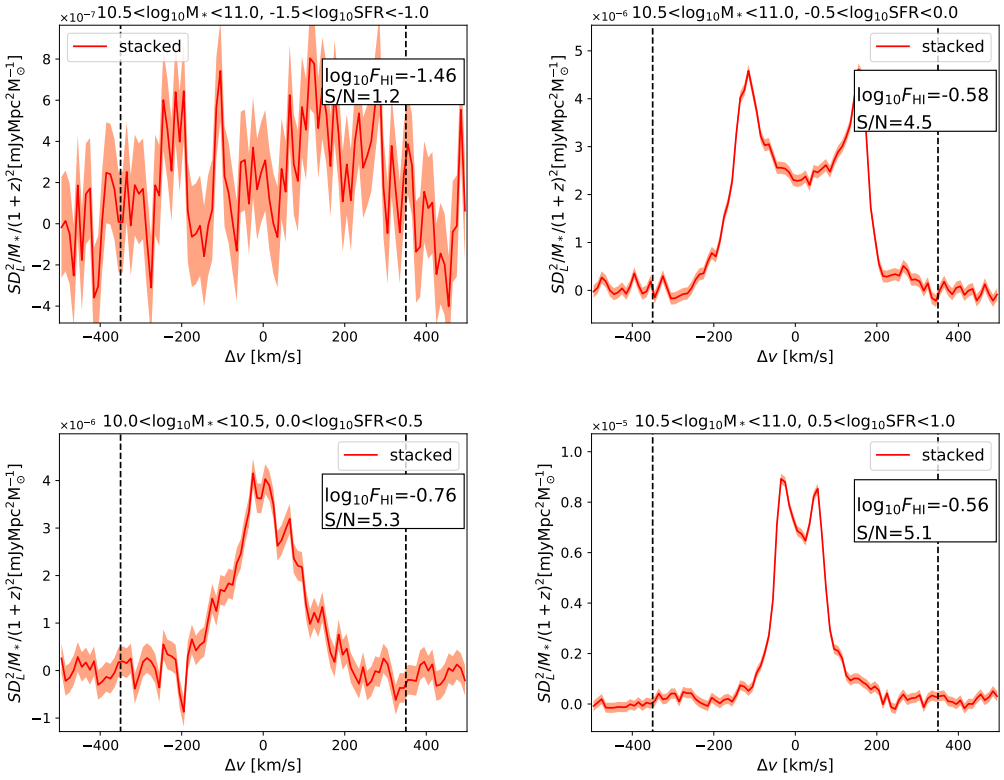

Figure A.7: Same figure as Figure A.5.

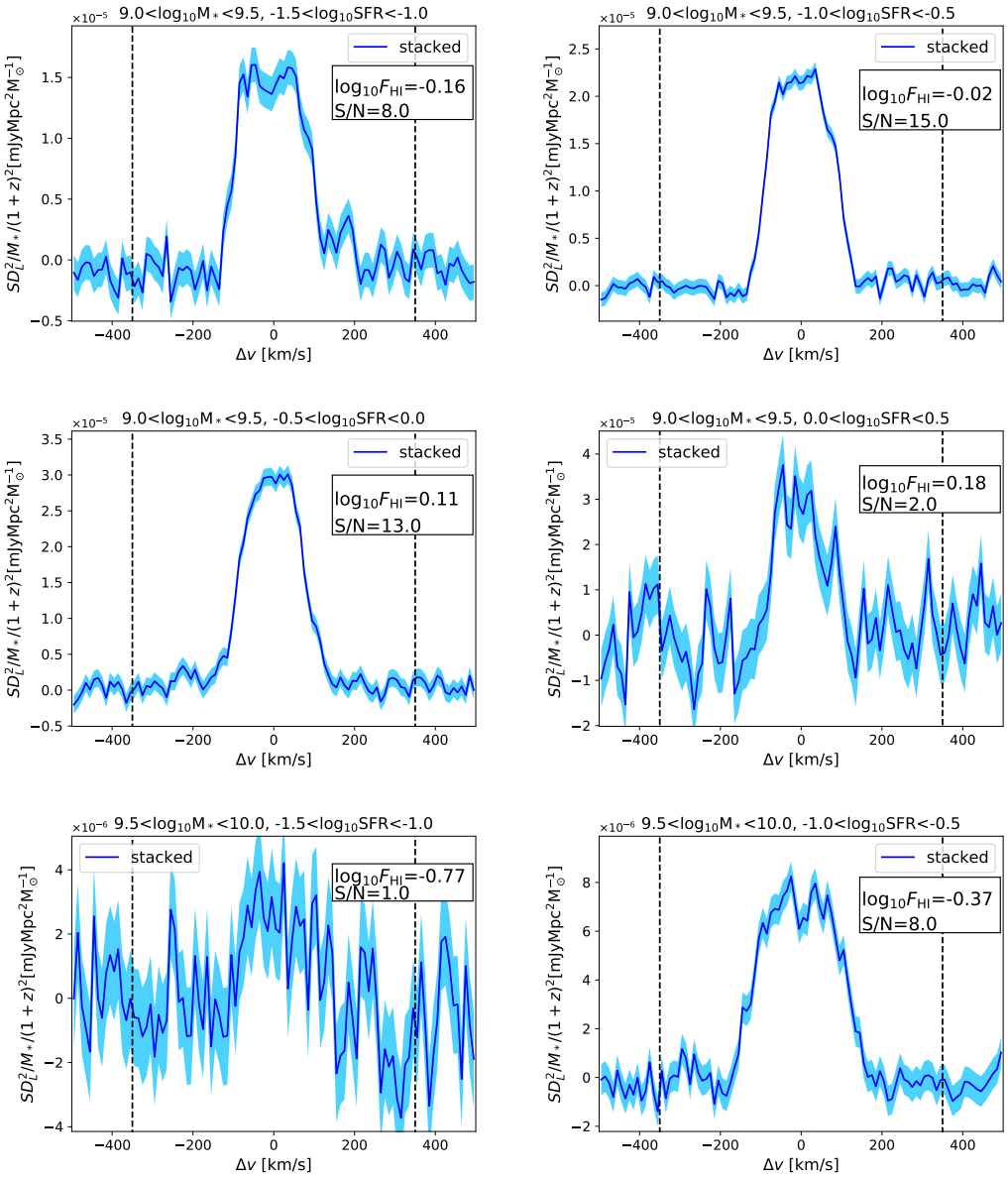

Figure A.8: A part of stacked H I spectra for late-type galaxies in Sec. 4.1. We write the M_* and *SFR* range on the top of each panel. The solid blue line is the average spectra, and the shaded region shows $1-\sigma$ error derived from *rms* of ALFALFA spectra. Vertical dashed lines, $F_{\rm HI}$, and S/N are the same as Figure A.1.

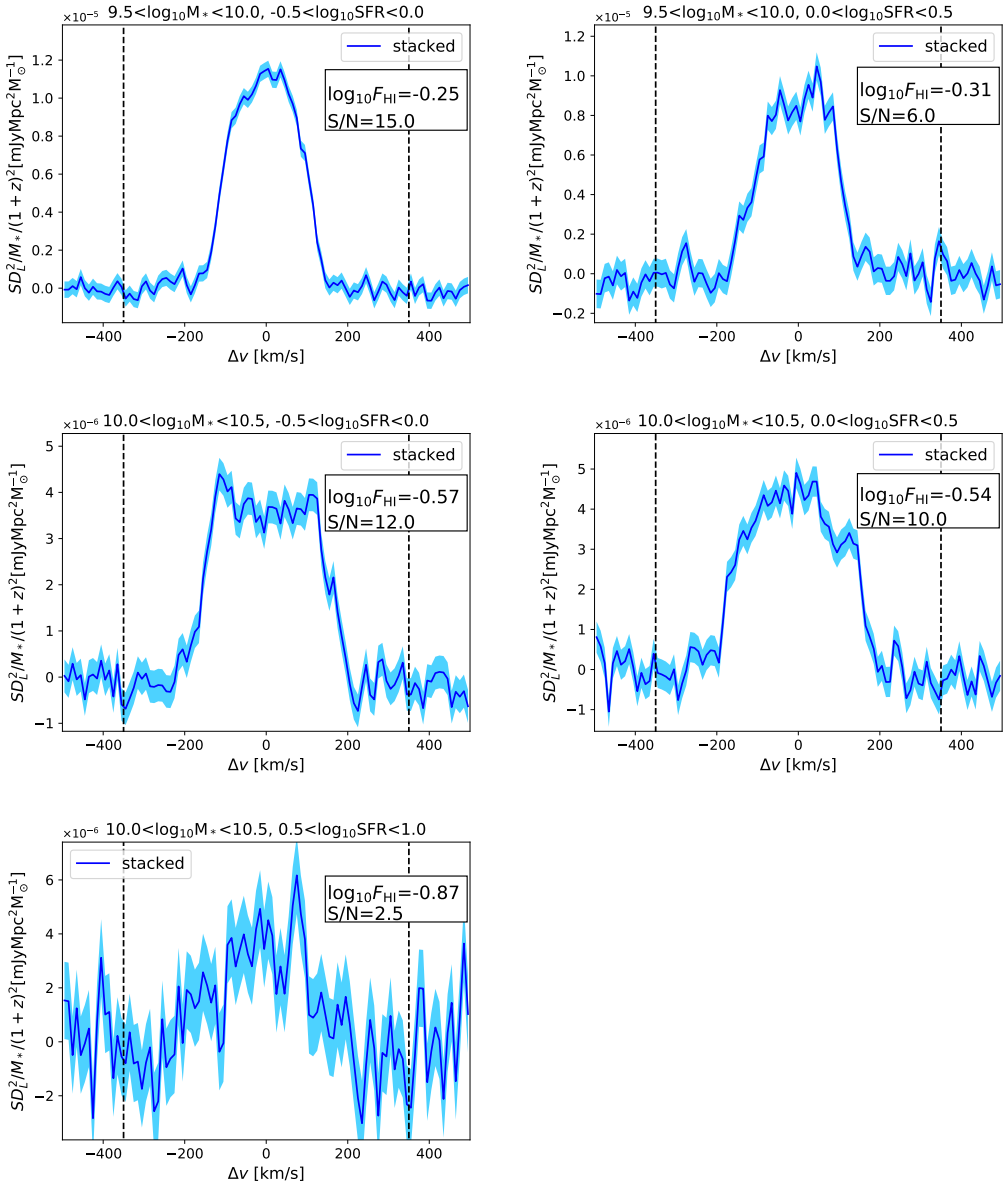

Figure A.9: Same figure as Figure A.8.

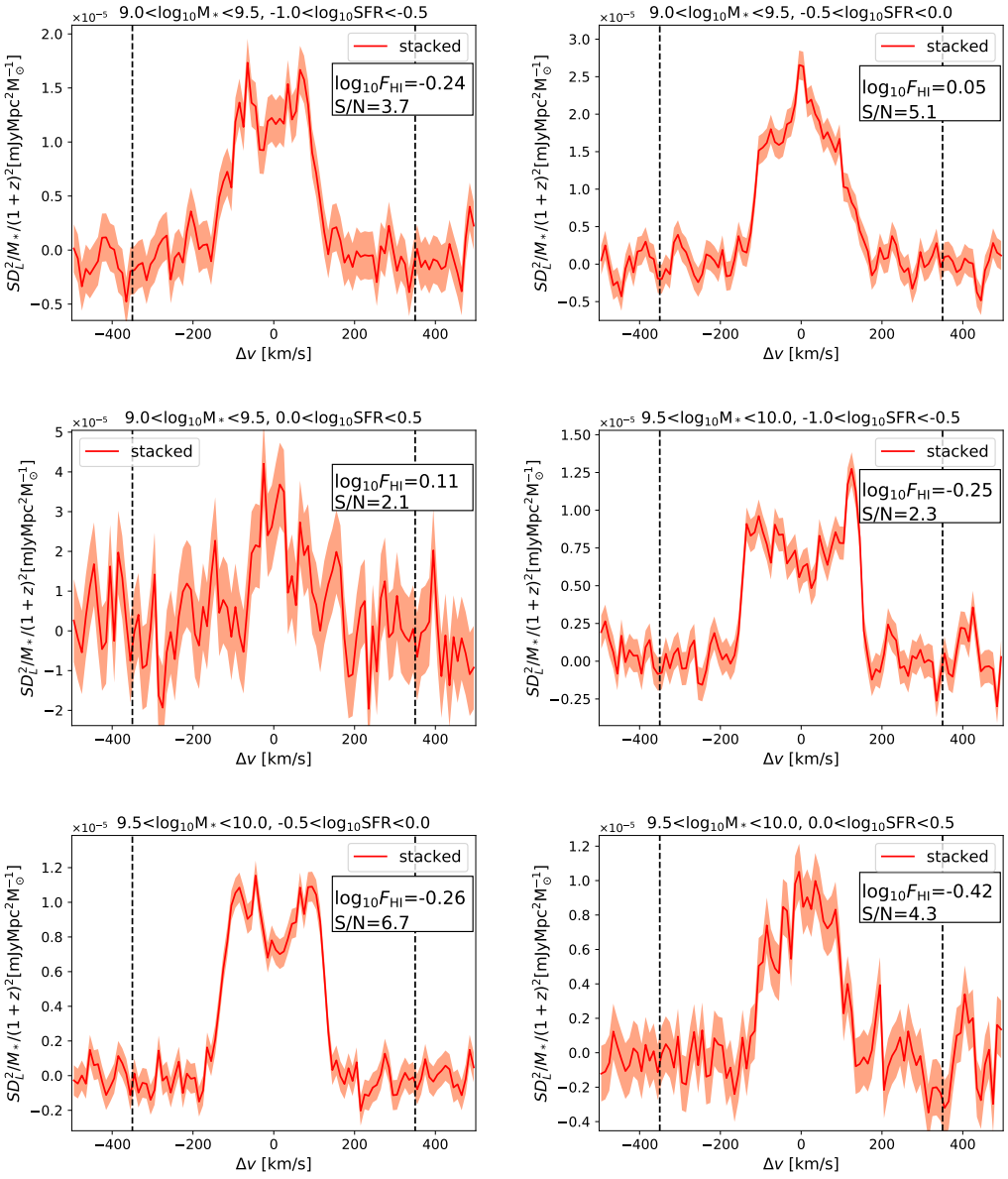

Figure A.10: A part of stacked H I spectra for bulge galaxies in Sec. 4.1. The M_* and *SFR* range, solid red line, shaded region, vertical dashed lines, $F_{\rm HI}$, and S/N are the same as Figure A.5.

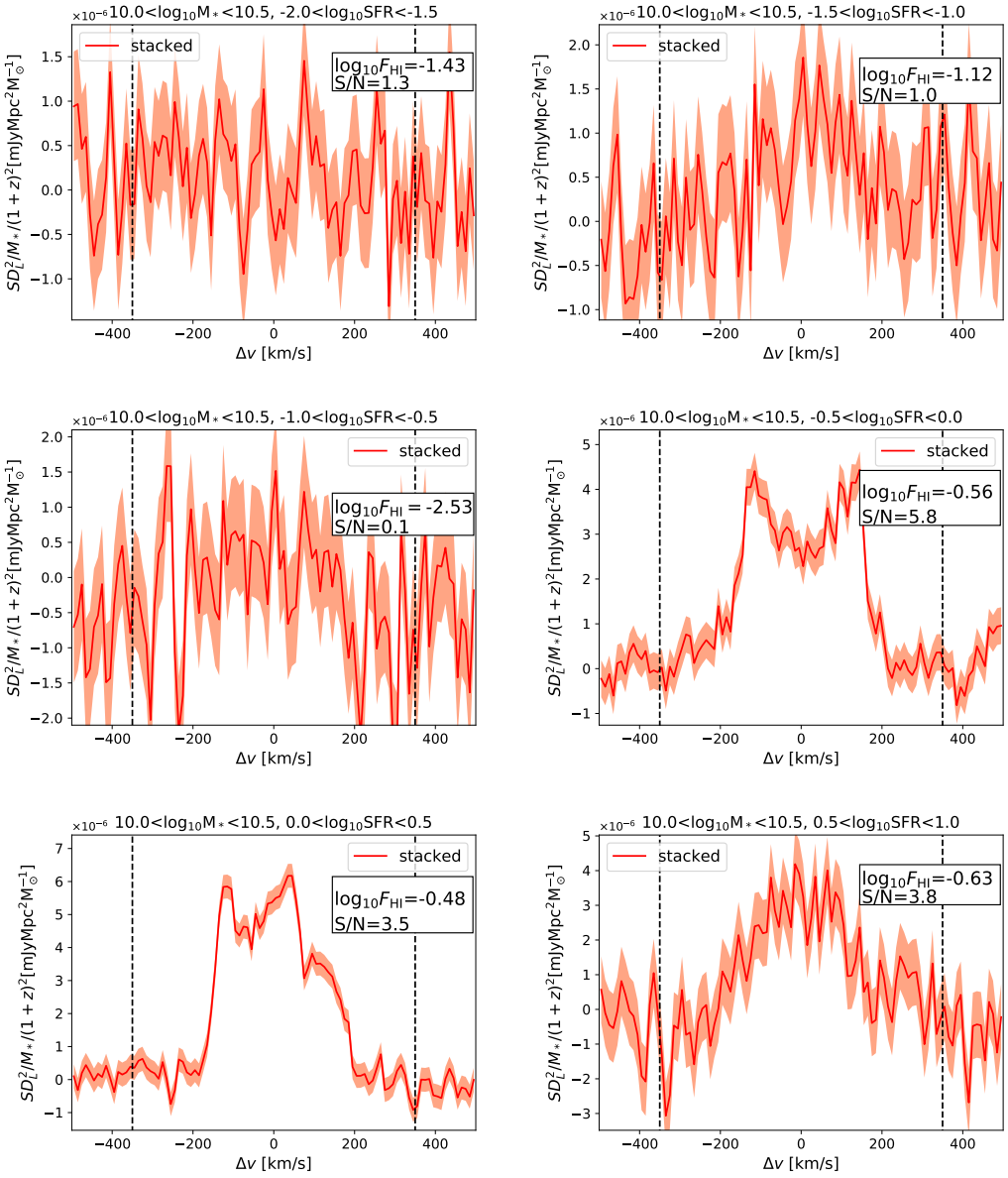

Figure A.11: Same figure as Figure A.10.

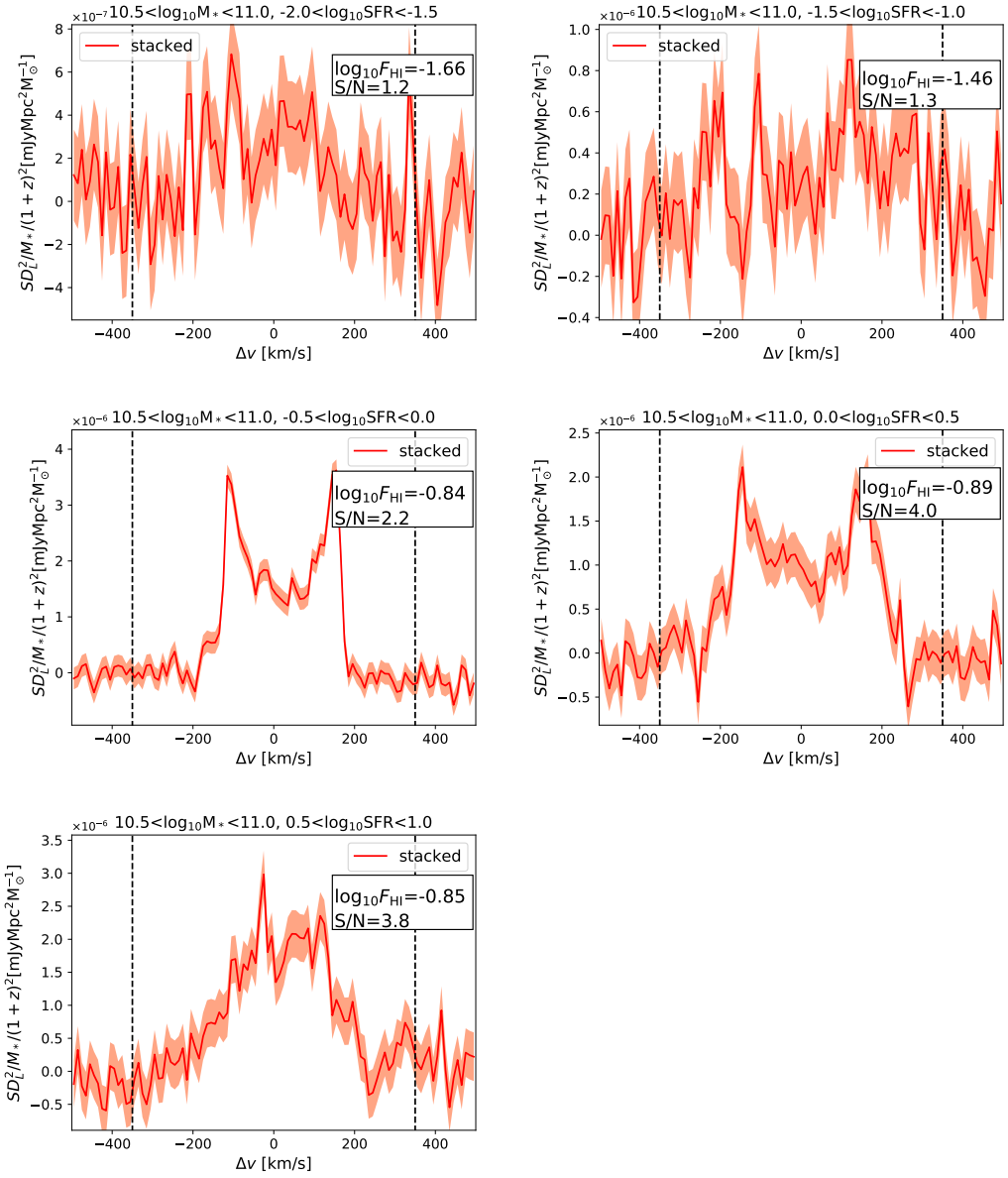

Figure A.12: Same figure as Figure A.10.

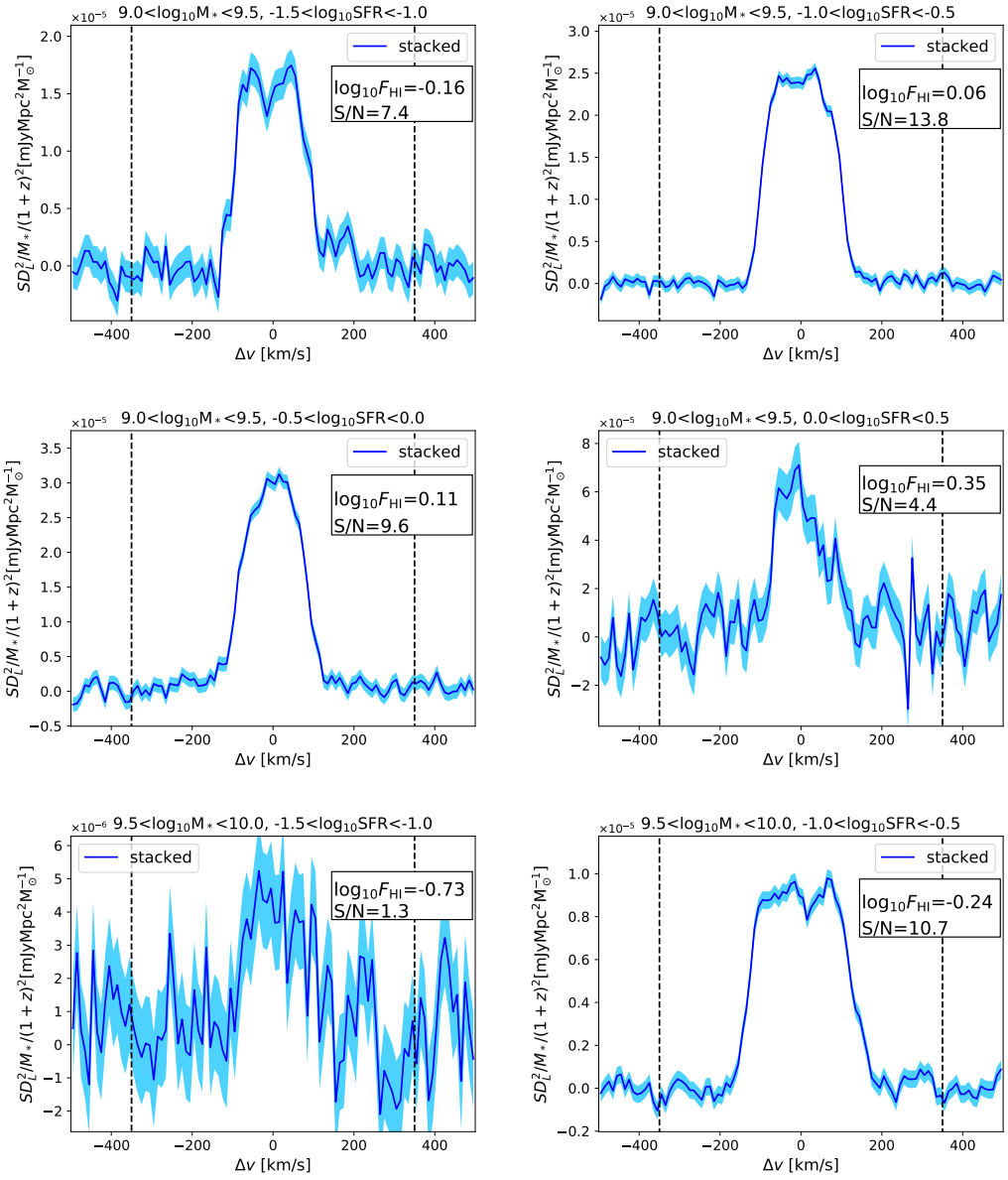

Figure A.13: A part of stacked H I spectra for disk galaxies in Sec. 4.2. The M_* and *SFR* range, solid blue line, shaded region, vertical dashed lines, $F_{\rm HI}$, and S/N are the same as Figure A.8.

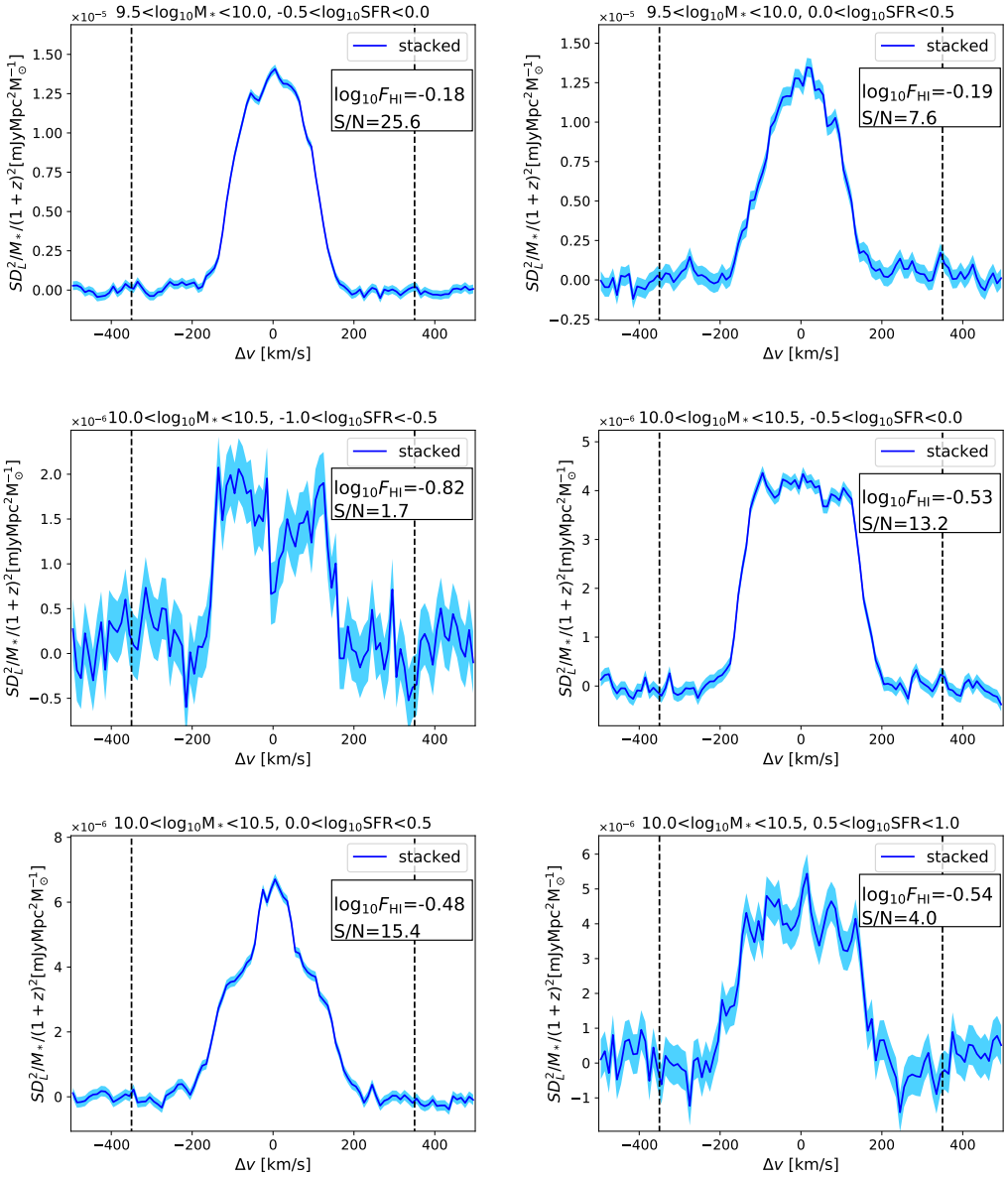

Figure A.14: Same figure as Figure A.13.

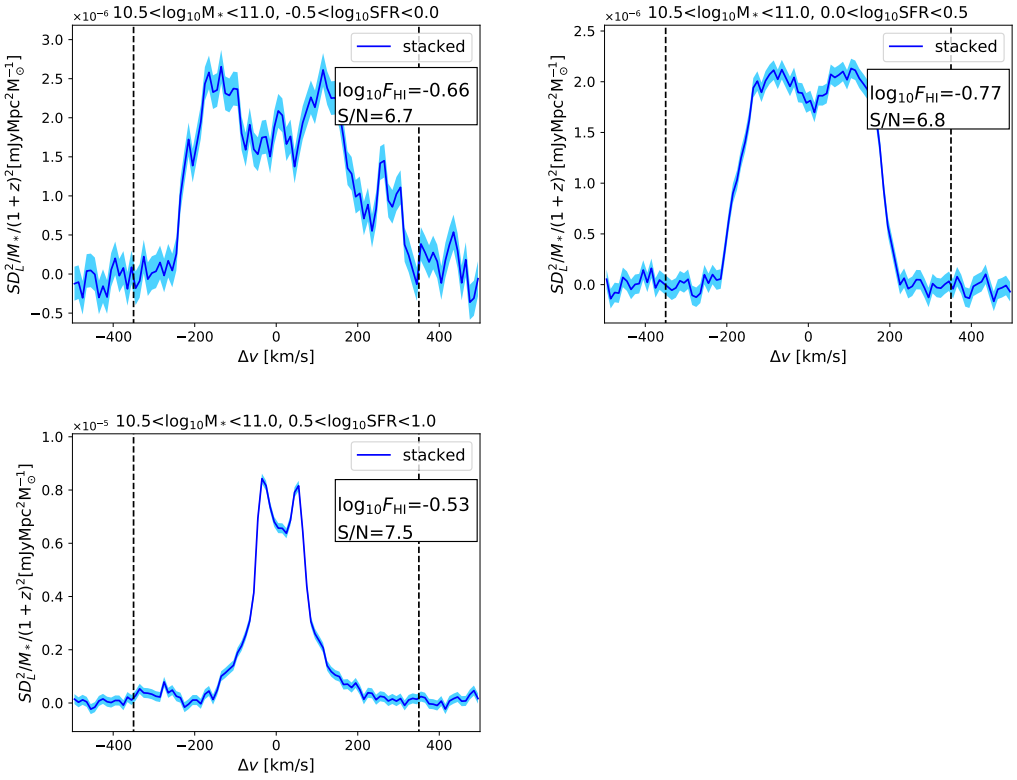

Figure A.15: Same figure as Figure A.13.

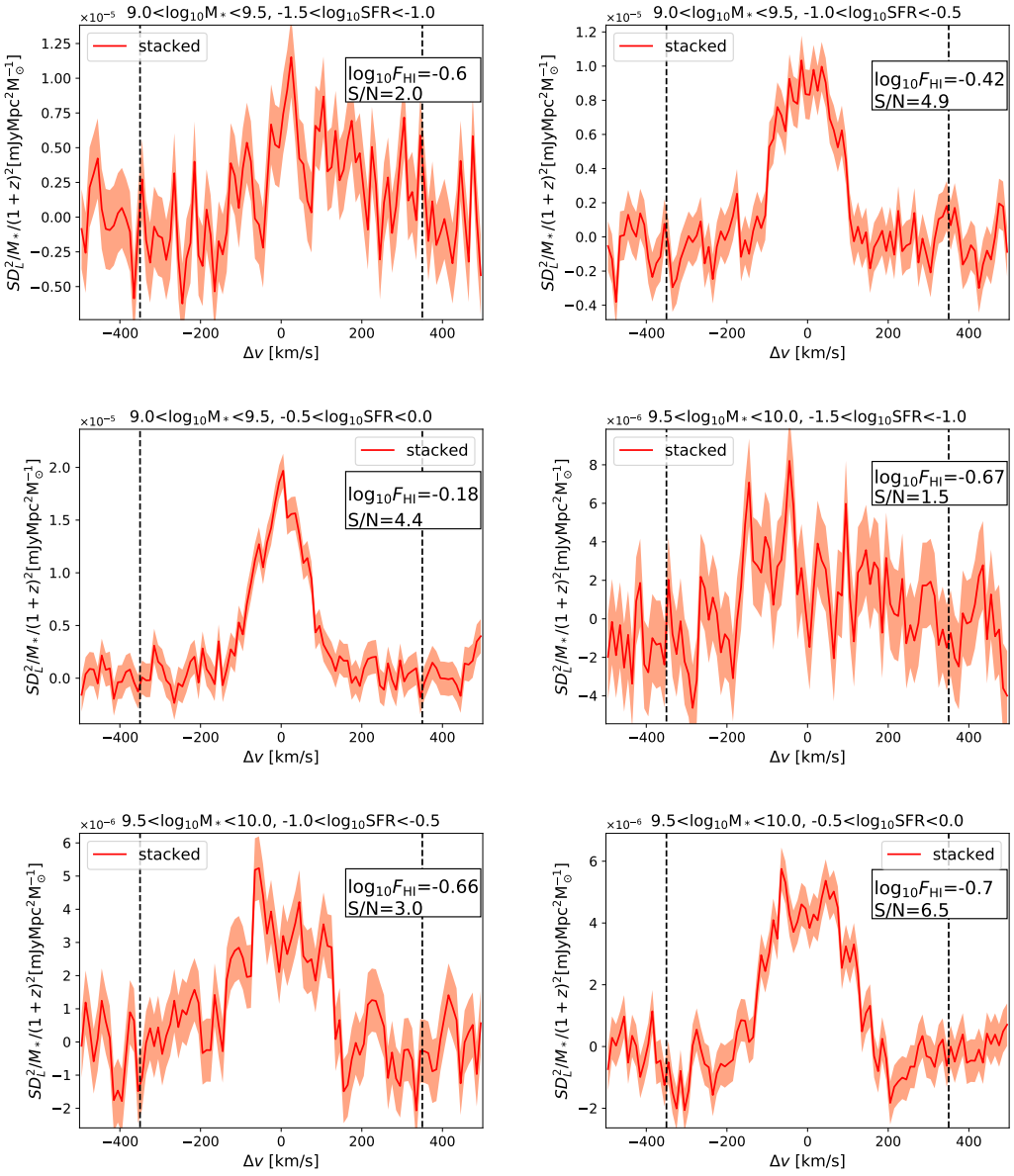

Figure A.16: A part of stacked H I spectra for smooth galaxies in Sec. 4.3. The M_* and *SFR* range, solid red line, shaded region, vertical dashed lines, $F_{\rm HI}$, and S/N are the same as Figure A.5.

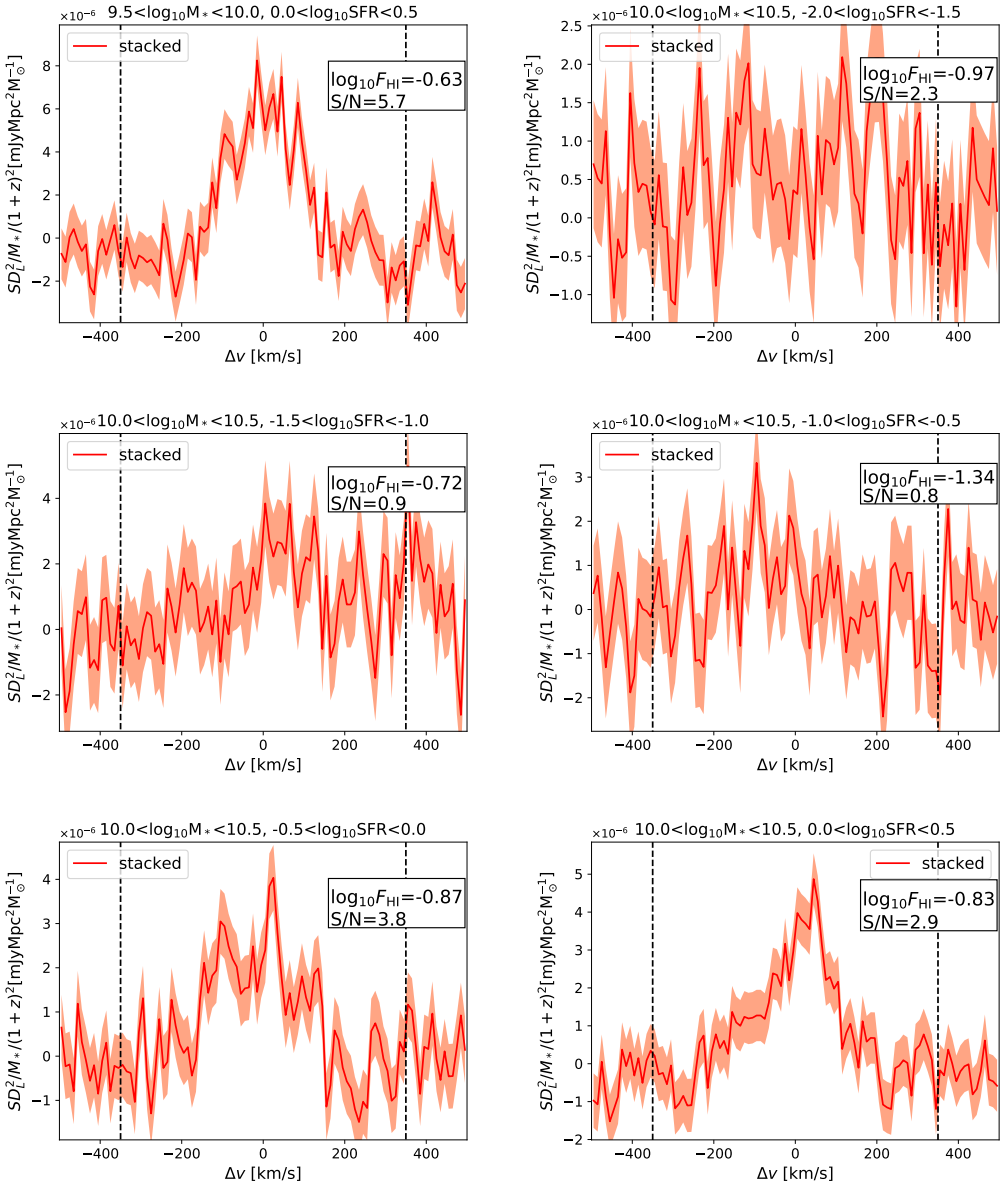

Figure A.17: Same figure as Figure A.16.

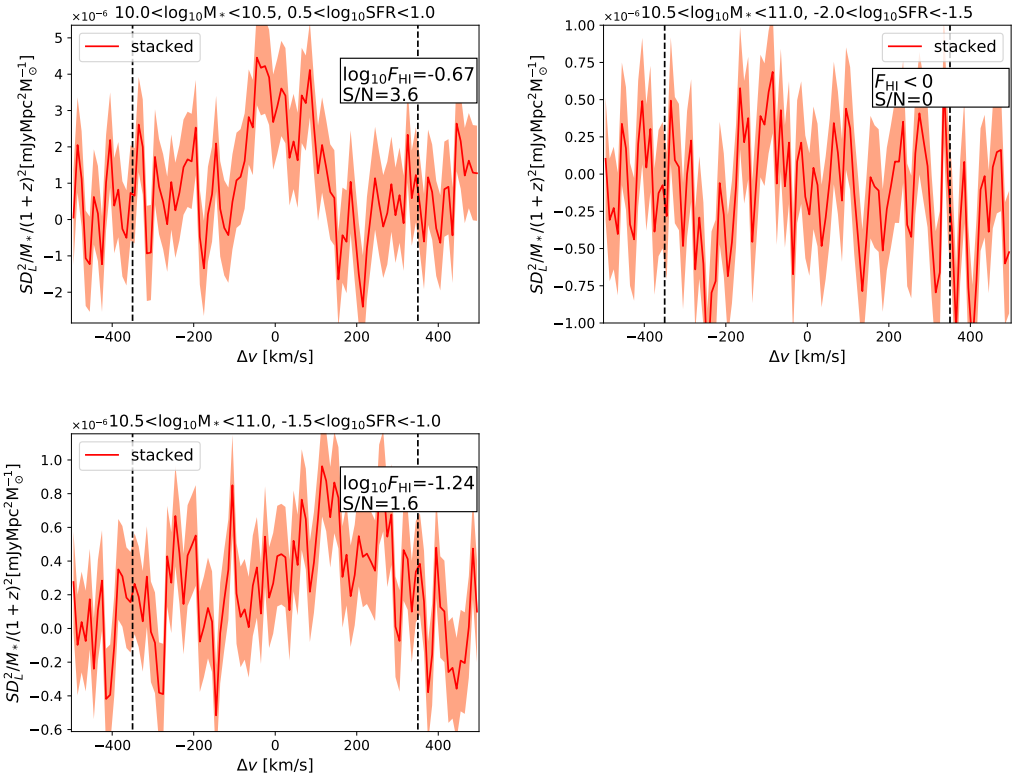

Figure A.18: Same figure as Figure A.16.

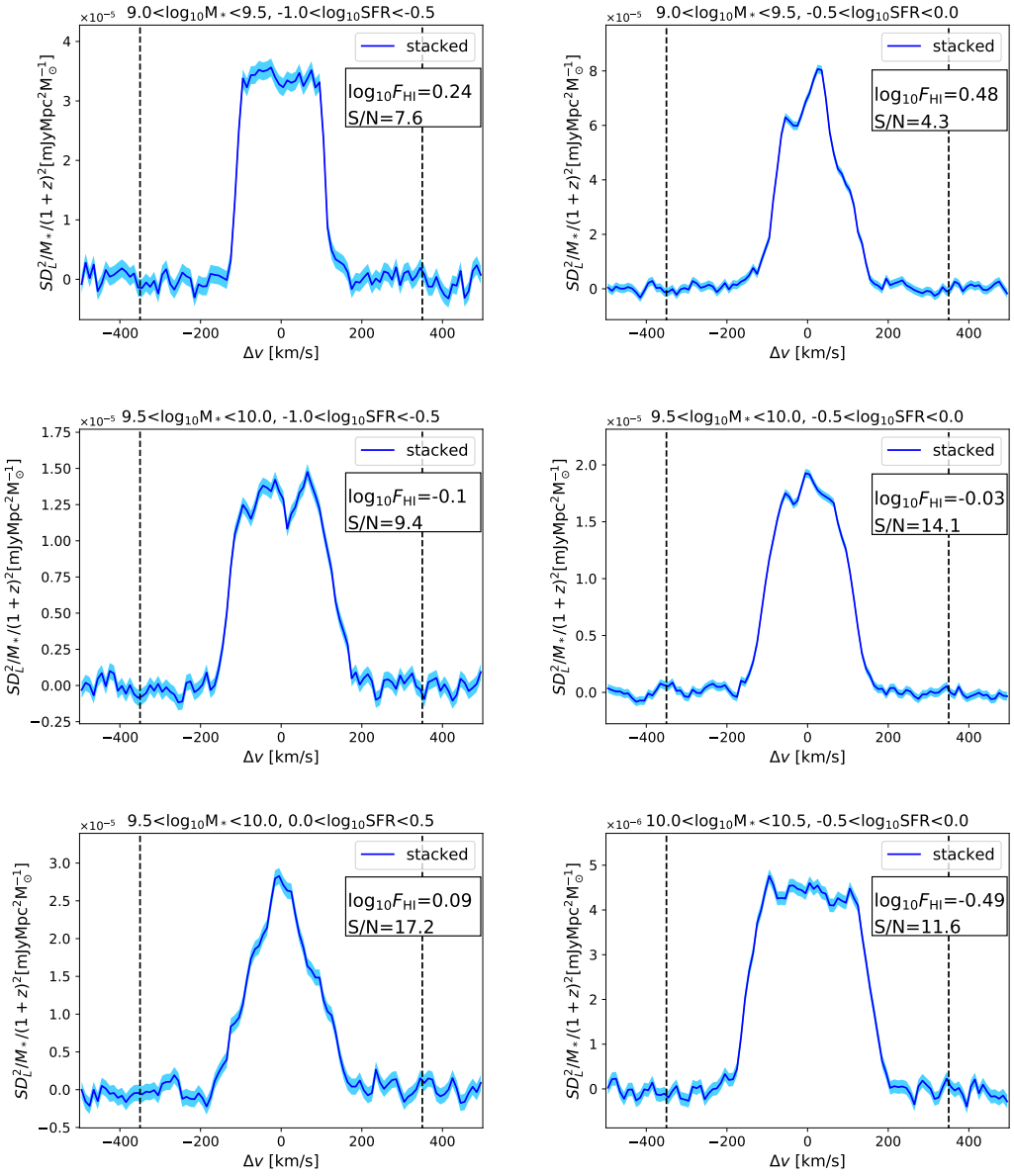

Figure A.19: A part of stacked H I spectra for non-smooth galaxies in Sec. 4.3. The M_* and *SFR* range, solid blue line, shaded region, vertical dashed lines, $F_{\rm HI}$, and S/N are the same as Figure A.8.

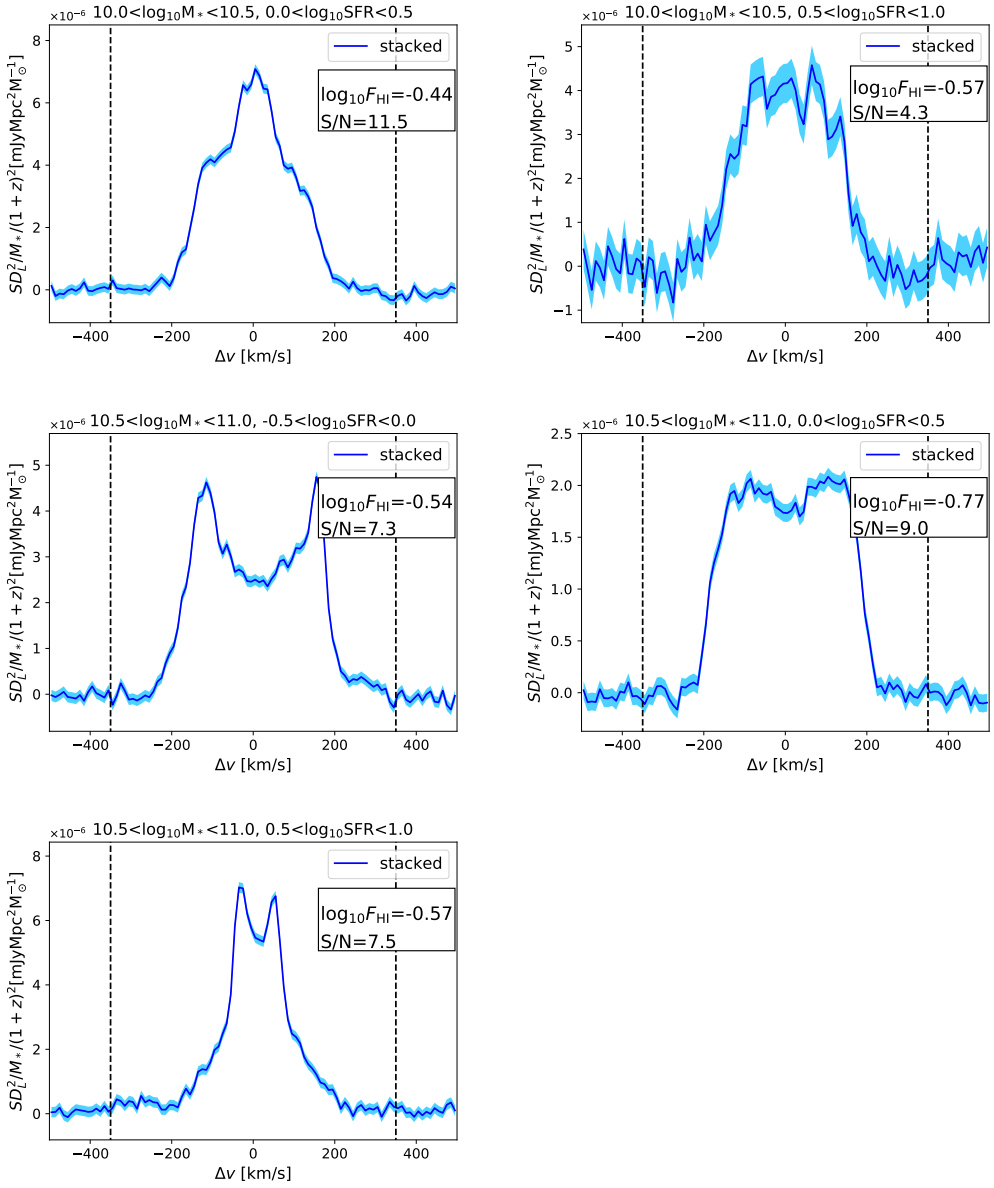

Figure A.20: Same figure as Figure A.19.

B

Spectroscopic study of a rich cluster at z=1.52 with Subaru & LBT: the environmental impacts on the mass-metallicity relation.

Abstract

Besides the study about the origin of the relation between galaxy morphology and its gas content, we investigated the environmental effect on the mass-metallicity relation at $z = 1.52$ (Namiki et al., 2019). Here we present the results of our near-infrared (NIR) spectroscopic observations of a cluster candidate around a radio galaxy at $z = 1.52$ (4C65.22) with Subaru/MOIRCS and LBT/LUCI. We observe 71 galaxies mostly on the star-forming main sequence selected by our previous broad-band (photo-z) and

narrow-band Hα imaging observation in this cluster environment. We successfully confirm the redshifts of 39 galaxies and conclude that this is a gravitationally bound, real cluster at $z = 1.517$. Our spectroscopic data also suggest a hint of large-scale filaments or sheet-like three-dimensional structures crossing at the highest-density cluster core. We stack the spectra to derive their average interstellar medium (ISM) gas-phase metallicity based on the [N II]/Hα emission line flux ratio. We find that the mass-metallicity relation (MZR) in the 4C65.22 cluster environment is consistent with Hα-selected field galaxies at similar redshifts. Our results suggest that the environmental impact on the MZR is small at high redshifts. However, a larger sample of high-z clusters and their member galaxies is still required to fully address the effect of the environment and its cluster-cluster variation.

B.1 Introduction

Galaxy properties are characterized by several parameters, e.g., stellar mass (M_*), star formation rate (SFR), color, or ISM gas-phase metallicity. Many studies have attempted to identify potential links between these parameters. A large sample of galaxies drawn by recent large surveys covering the vast area on the sky (like Sloan Digital Sky Survey; SDSS, York et al. 2000) allowed us to unveil many fundamental correlations between the physical parameters. One of the most prominent examples is the tight correlation between M_* and SFR for star-forming galaxies; so-called star formation main sequence (SFMS; Brinchmann et al. 2004; Peng et al. 2010). The correlation between M_* and ISM gas-phase metallicity (mass–metallicity relation, MZR) is also well established in the local universe (e.g., Tremonti et al. 2004).

The environment of galaxies is thought to be another critical parameter that influences galaxy properties. In the local universe, the central regions of galaxy clusters are in general dominated by red, passive galaxies, while blue, star-forming galaxies are mainly located in their outskirts (e.g., Dressler 1980; Goto et al. 2003; Gomez et al. 2003; Balogh et al. 2004; Tanaka et al. 2004). It is reported that the SFMS does not significantly change with the environment in the local Universe (Peng et al., 2010). Similarly, it is reported that MZR shows little environmental dependence, at least in the local universe (e.g., Cooper et al. 2008; Ellison et al. 2009; Wu et al. 2017).

However, the correlations between galaxy properties established in the local universe are not necessarily applicable to galaxies in the distant universe, where the cosmic star formation rate density is much higher than the present-day Universe (Hopkins & Beacom, 2006). Therefore, our next important step is to investigate the evolution of those relationships and understand how the correlations are formed and maintained across cosmic time and environment. Studies show the redshift evolution of the SFMS and MZR, and the existence of SFMS up to $z \sim 6$ (e.g., Salmon et al. 2015; Tomczak et al. 2016; Santini et al. 2017). The MZR is also shown to exist up to $z \sim 3.5$ (e.g., Erb et al. 2006; Maiolino et al. 2008; Troncoso et al. 2014; Onodera et al. 2016; Sanders et al. 2018).

Considering the well-known increasing fraction of star-forming galaxies in higher-redshift cluster environments (Butcher & Oemler, 1984; Dokkum et al., 2000), one might expect that environmental effects on galaxy properties could be weaker in the more

distant universe. However, it is always challenging to construct a large, uniform sample of galaxies in the distant universe. It prevents us from unveiling the environmental variation (if any) in the fundamental correlations between galaxy properties at high redshifts. However, some authors studied the environmental dependence of the SFMS by comparing star-forming galaxies in high- and low-density environments (e.g., Vulcani et al. 2010; Li et al. 2011; Koyama et al. 2013), a complete consensus has not yet been obtained.

Furthermore, because ISM gas-phase metallicity measurement of distant galaxies requires deep spectroscopy in NIR, it is much more difficult to investigate the environmental dependence of MZR at high redshifts. There are only a limited number of observational studies discussing the environmental impacts on the MZR at the "cosmic noon" epoch (e.g., Kulas et al. 2013; Shimakawa et al. 2015; Valentino et al. 2015; Tran et al. 2015; Kacprzak et al. 2015; Shimakawa et al. 2015), and interestingly, their conclusions are different from study to study. For instance, Kulas et al. (2013), Shimakawa et al. (2015), and Maier et al. (2019) investigated the ISM gas-phase metallicity of member galaxies of (proto-) clusters at z = 1.5, 2.2, 2.3, and 2.5. They suggested that the mean metallicity of low-mass cluster galaxies is *higher* than that of field galaxies with the same stellar mass. Kulas et al. (2013) and Shimakawa et al. (2015) claimed that the metal recycling of momentum-driven outflow could explain this difference; i.e., outflow from a star-forming galaxy returns to itself in a short time scale due to the higher pressure of surrounding IGM in a denser environment. This mechanism would work more effectively on low-mass galaxies because their escape velocity is lower than that of high-mass galaxies. Thus metal-enriched gas is easier to be blown out from less massive galaxies.

On the other hand, Tran et al. (2015) and Kacprzak et al. (2015) suggest that there is no significant environmental dependence in the MZR at $z \sim 2$. They concluded that the environmental effect is, if present, small and not a primary factor. In addition, Valentino et al. (2015) investigated a galaxy cluster at z = 1.99 and claimed that the member galaxies of this cluster have *lower* ISM gas-phase metallicity than field galaxies at the same redshift. Their interpretation is that the inflow of pristine gas into a high-density environment would dilute the gas metallicity and enhance the specific SFR of galaxies residing in high-density environments.

This part presents the results of our new spectroscopic observations for galaxies in another distant cluster at $z = 1.52$ (4C65.22). This cluster (candidate) was initially discovered by a photometric Hα study of a radio galaxy field with Subaru (Koyama et al., 2014). They observed this region with broad-band and narrow-band (Hα) imaging with Subaru/MOIRCS (FoV: $7' \times 4'$, Ichikawa et al. 2006; Suzuki et al. 2008) and found 44 Hα emitter candidates. In addition, by using the photometric redshifts (photo-z) derived with the optical (Subaru/Suprime-Cam; Miyazaki et al. 2002) and NIR (Subaru/MOIRCS) data, it was clearly shown that red-sequence galaxies (with $z' - J > 1.2$) are strongly clustered in the central region ($\lesssim$200 kpc). In contrast, blue galaxies ($z' - J < 1.2$) are located in the outskirt region. They claimed that this is an excellent example of a "mature" cluster at this high redshift, although the cluster was not spectroscopically confirmed so far. We performed a follow-up NIR spectroscopy of star-forming galaxies in this rich cluster environment with Subaru/MOIRCS and Large binocular telescope (LBT)/LUCI. We first confirm the physical association of the cluster member galaxies in this field. We investigate the gas-phase metallicity (hereafter "metallicity" for simplicity) of those cluster members and discuss the environmental dependence of MZR at $z = 1.5$.

The structure of this part is as the following. In Section B.2, we show our sample selection and summarize the NIR spectroscopic observations with LBT/LUCI and Subaru/MOIRCS. In Section B.3, we present the 2D distribution of cluster member galaxies and measure their gas-phase metallicity, and then discuss the environmental dependence of MZR in Section B.4. We summarize our results in Section B.5. Throughout this part, we adopt a flat ΛCDM cosmology with $\Omega_m = 0.3$, $\Omega_\Lambda = 0.7$ and $H_0 = 70$ km s^{-1} Mpc^{-1}, and a Salpeter initial mass function (IMF, Salpeter 1955). These cosmological parameters give a $1''$ scale of 8.46 kpc and the cosmic age of 4.2 Gyr at the redshift of our target cluster ($z = 1.52$). Magnitudes are all given in the AB system.

B.2 Observation & Data

This study aims to spectroscopically confirm the physical association of the strong over-density of galaxies in the 4C65.22 field reported by Koyama et al. (2014) and to study the properties of galaxies in a high-density environment at this redshift. We performed NIR spectroscopic observations of 71 galaxies in the 4C65.22 field with LBT/LUCI (Seifert et al. 2003) and Subaru/MOIRCS (Ichikawa et al. 2006; Suzuki et al. 2008). Our primary targets are Hα emitters and blue galaxies (star-forming galaxy candidates) identified by Koyama et al. (2014) because it is much harder to detect continuum emission and absorption lines of red galaxies without emission lines at this redshift. In Fig.B.1, we show the distribution of our Hα emitter sample on the M_*-SFR plane. The red circles represent Hα-emitter candidates reported in Koyama et al. (2014), and the blue points indicate Hα detected galaxies by our spectroscopic observation. The histograms at the top and right-hand side show the normalized distribution of M_* and SFR of our sample, respectively. It can be seen that our spectroscopic samples are typical star-forming galaxies located on the SFMS at $z \sim 1.5$, and there is no strong bias for the whole Hα emitter sample in this field constructed by Koyama et al. (2014). Below, we describe the details of our observations.

B.2.1 LBT/LUCI spectroscopy

The NIR spectroscopic observation was carried out in May 2014 with LBT/LUCI, a NIR spectrograph and imager for LBT (Seifert et al. 2003). We used the multi-object slit (MOS) mode with 210_zJHK grating with 1″ slit width, which gives a spectral resolution of $R \sim 3900$ over $\lambda = 1.55 - 1.74$ μm. We prepared three MOS masks, each of which includes ten target galaxies. There are three galaxies observed with two masks, and the total number of our LUCI targets is 27. The exposure time for each configuration (LUCI-1, 2, and 3) is 70, 110, and 130 minutes, respectively, with a mean seeing size of ∼1″. Table B.1 summarizes our observation.

We reduced the data using a custom-made pipeline, Pyroscope (developed by J. Kurk). The pipeline process includes bad-pixels, cosmic ray correction, distortion correction, wavelength calibration for each slit, sky subtraction, and combine. With a visual inspection of the 2-D spectra, we identified pixels with emission lines and

extracted the 1-D spectra. We detected emission line (with $> 3\sigma$) for 19 galaxies at $\lambda = 16370 - 16770$ Å. Here we use the background noise spectrum to measure the signal-to-noise ratio at the peak of emission lines. We note that this wavelength range corresponds to the transmission curve of the NB1657 filter used in Koyama et al. (2014) to identify Hα emitters at $z = 1.52$. For galaxies with emission lines, we determine the redshift of each galaxy by Gaussian fitting with the weight determined by the background noise spectrum. We also detect [N II]λ6583 line for 12 out of 19 galaxies. For the remaining 7 galaxies (with single emission line detection), we cannot rule out the possibility that other emission lines at different redshifts (such as [O III]λ5007, λ4959 lines at $z \sim 2.3$ or [O II]λ3726, λ3729 lines at $z \sim 3$.) could contaminate. However, we believe that this is less likely; in the case of [O II]λ3726, λ3729 we could detect the doublets with the spectral resolution of LUCI. In contrast, in the case of [O III]λ5007, λ4959, we expect H$\beta\lambda$4861 line (as well as [O III]λ4959 line in the case of bright objects) within the observed wavelength range in addition to the [O III] doublet. Therefore, We assume that the strong emission lines detected in the range of $\lambda = 16370 - 16770$ Å are Hα, but much deeper spectroscopy would be needed to confirm their redshifts fully.

B.2.2 Subaru/MOIRCS spectroscopy

We also performed multi-object NIR spectroscopy of galaxies in the 4C65.22 field in May 2015 with Subaru/MOIRCS using $zJ500$ grism with 0.8" slit width, which provides a spectral resolution of $R \sim 464$ over $\lambda = 0.9 - 1.78$ μm. We designed two MOS masks (with 33 objects for each), and the exposure time was 3 hours for each mask under the seeing conditions of 0.5" – 0.8" (see also Table B.1). We note that 16 of the MOIRCS targets are overlapped with our LUCI targets so that the number of galaxies observed only with Subaru/MOIRCS is 41.

The data reduction was performed using the MOIRCS spectroscopic pipeline, MCSMDP (Yoshikawa et al. 2010). The pipeline process includes flat-fielding, bad-pixels, cosmic ray correction, distortion correction, wavelength calibration for each slit, sky subtraction, combine, and flux calibration. By inspecting the reduced spectra, we determined the redshifts of 17 galaxies (for which significant emission lines are detected) in the same way as described in Section B.2.1. We note that, depending on

Mask	Exp. time (min)	Seeing (arcsec)	Slit width (arcsec)	N_{obj}
LUCI-1	70	~1.0	1.0	10
LUCI-2	110	~0.7	1.0	10
LUCI-3	130	~1.2	1.0	10
MOIRCS-1	180	~0.5	0.8	33
MOIRCS-2	180	~0.8	0.8	33

Table B.1: Summary of our spectroscopic observations

the slit positions on the masks, some of the spectra do not cover the wavelength range of $\lambda \sim 1.65$ μm (where we expect the Hα lines of cluster member galaxies). For those galaxies, we instead try to identify emission lines over the range between $\lambda = 12175$Å and 13015Å to look for the [O III]λ5007 line for the same redshift. With this approach, we additionally identify three galaxies in this field.

B.2.3 Final Sample

We successfully determined the redshifts of 39 galaxies in total; 19 from LUCI, 27 from MOIRCS, and seven are observed with both. For seven galaxies observed with both LUCI and MOIRCS, we confirm that their redshifts derived from LUCI/MOIRCS data are consistent, suggesting no systematic bias between the data obtained with different telescopes/instruments. We show in Table B.2 the complete list of the spectroscopically confirmed cluster member galaxies in the 4C65.22 field and their basic properties.

We comment that we quote the M_* and SFR derived by Koyama et al. (2014); they determined M_* with K_s-band photometry with $M_*/L_{K_s,obs}$ correction based on the $z' - K_s$ color (see eq.1 in Koyama et al. 2014), while they derived SFR with Hα photometry. To measure the Hα flux of individual galaxies, they first calculated the Hα+[N II] line flux, continuum flux density, and EW_{rest} of each Hα emitter from their broad-band and narrow-band imaging data. They derived the [N II]/Hα line flux ratio from the Hα+[N II] equivalent width using the empirical relation for local star-forming galaxies established by Sobral et al. (2012). Then, they corrected for the dust attenuation effect with $SFR_{H\alpha}/SFR_{UV}$ ratio (Buat 2003; Tadaki et al. 2013; see also Koyama et al. 2014) to finally derive SFR and sSFR of the Hα emitter sample. We note that the [N II] correction and the dust extinction correction are the major sources of

uncertainty when deriving the SFRs with this approach. Koyama et al. (2015) reported that the uncertainty associated with the dust extinction correction from the Hα/UV ratio is typical $\sim$ 0.4 mag. Also, Villar et al. (2008) showed that the scatter around the correlation between the Hα/[N II] ratio and the Hα+[N II] equivalent width is $\sim$0.4 dex. Accordingly, we estimate the typical error of the SFR of our sample is $\sim$ 0.2 dex. On the other hand, we propagate the photometric errors of our z-band and Ks-band data for the stellar mass estimate. These uncertainties are shown with the red-line error bars in Fig.B.1.

We have mainly used the Hα line for the redshift determination, but another important goal of this study is to investigate the metallicity of galaxies in this cluster region. In order to use N2 index (Pettini & Pagel 2004) for metallicity calibration (see Sec.B.3.3), we choose galaxies whose [N II]λ6583 emission line is not contaminated by strong OH night sky lines. We visually inspect the spectra of our final sample and carefully select 19 galaxies from the LUCI sample and 12 galaxies from the MOIRCS sample, in which five galaxies are observed with both instruments. [1] We use these 26 "clean" galaxies when we study the environmental impacts on the MZR (Sec.B.3.3). Here we note that we do not apply any aperture correction because the results of this part rely only on the Hα and [N II]λ6583 line flux ratio. We note that the seeing size is larger than the slit width for ten galaxies observed with LUCI-3. This slightly degrades the quality (S/N) of the spectra, but the line flux ratio should not be strongly affected.

Finally, we note that AGNs can contribute to enhancing their [N II] emission line fluxes, which might affect our metallicity measurement (N2 index, Pettini & Pagel 2004; see Sec.B.3.3). In addition, it is also expected that AGN at these redshifts is often accompanied by strong outflow (Genzel et al. 2014). Because the S/N ratio of our MOIRCS sample is not enough, we cannot rule out the possibility of AGN. For galaxies observed with LUCI, we carefully inspected each spectrum, and we confirm that there are no broad-line features with $FWHM \gtrsim 1000$ km/s or no extremely enhanced [N II]λ6583 emission lines in our sample. We, therefore, conclude that the effect from type-1 AGN is small, but we cannot eliminate the possibility of contamination from type-2 AGN. On the other hand, for the galaxies observed with MOIRCS, we examine the

[1] We note that the FWHMs of OH emission lines are large for our MOIRCS spectra because of their spectral resolution ($\sim$ 290). We realize that the relatively large number (15) of our MOIRCS sample is severely affected by the OH emission lines at the wavelengths corresponding to their [N II]λ6583 lines.

line flux ratios on the BPT diagram (e.g., Baldwin et al. 1981, Kewley et al. 2013) using the stacked spectrum (see Sec.B.3.2). We find that the emission line flux ratios for both high-mass ($10^{10.48}M_{\odot} < M_{*} < 10^{11.41}M_{\odot}$) and low-mass ($10^{9.93}M_{\odot} < M_{*} < 10^{10.48}M_{\odot}$) subsamples are consistent with HII (star-forming) galaxies on the BPT diagram at $z = 1.5$ (Kewley et al. 2013), but it is difficult to completely rule out the potential contribution from AGNs due to the large error in log([O III]/Hβ) ($\sim$ 0.3 dex)[2]. We thus need to keep in mind that the metallicity derived for our sample may be slightly overestimated by the potential AGN contribution.

[2]The large errors for the log([O III]/Hβ) ratio are partly caused by the contamination from strong OH emission lines at the wavelengths of their Hβ and/or [O III] lines. We carefully removed the spectra whose Hα or [N II] lines are contaminated by OH emission lines from our analyses (see also Sec.B.3.2). Howevrer, we do not do this for the Hβ or [O III] lines to keep a reasonable sample size (and it is not a problem because we do not use Hβ or [O III] lines for the metallicity measurements in this study).

Table B.2: List of all Hα detected sample

ID	R.A. (deg)	Dec. (deg)	Redshift	M_* $\log_{10}(M_\odot)$	SFR $\log_{10}(M_\odot yr^{-1})$	Inst. L/M	Lines	Stacking Y/–
293	266.822007	65.514093	$1.5135^{\pm 0.0029}$	$10.14^{\pm 0.25}$	1.49	M	Hα, [N II], [O III]	Y
357	266.767425	65.516084	$1.5135^{\pm 0.0031}$	$10.75^{\pm 0.05}$	1.47	M	Hα, Hβ	Y
409	266.786743	65.517948	$1.5130^{\pm 0.0027}$	$10.70^{\pm 0.05}$	1.27	M	Hα, [N II]	Y
453	266.73966	65.519072	$1.5119^{\pm 0.0026}$	–	–	M	Hα, [O III]	–
538	266.79246	65.521753	$1.5312^{\pm 0.0381}$	–	–	M	Hα	–
576*	266.705835	65.523181	$1.4492^{\pm 0.0021}$	$11.06^{\pm 0.02}$	1.21	M	Hα	–
665*	266.73212	65.526527	$1.6493^{\pm 0.0039}$	–	–	M	Hα	–
874	266.908468	65.535837	$1.5133^{\pm 0.0009}$	$10.63^{\pm 0.07}$	1.41	L	Hα	Y
930	266.793808	65.537622	$1.5104^{\pm 0.0017}$	$10.32^{\pm 0.15}$	1.01	M	Hα, [N II], [O III]	Y
1002	266.680192	65.540946	$1.5139^{\pm 0.0009}$	$10.73^{\pm 0.05}$	1.54	L	Hα, ([N II])	Y
1006	266.821641	65.541230	$1.5126^{\pm 0.0006}$	$10.45^{\pm 0.09}$	1.09	L/M	Hα, Hβ	Y
1046	266.811661	65.542944	$1.4980^{\pm 0.0017}$	$11.38^{\pm 0.02}$	1.51	M	Hα	–
1085	266.773938	65.544516	$1.5247^{\pm 0.0009}$	$10.30^{\pm 0.18}$	1.57	L/M	Hα, [N II]	Y
1151	266.808950	65.546952	$1.5338^{\pm 0.0013}$	$10.78^{\pm 0.04}$	1.49	L/M	Hα, [N II]	Y
1193	266.857945	65.548677	$1.5153^{\pm 0.0007}$	$10.21^{\pm 0.16}$	1.26	L	Hα	Y
1248	266.818480	65.550677	$1.5157^{\pm 0.0011}$	$11.28^{\pm 0.02}$	1.89	L	Hα, ([N II])	Y
1249	266.823656	65.550228	$1.5211^{\pm 0.0007}$	$10.87^{\pm 0.05}$	1.68	L/M	Hα, [N II], (Hβ)	Y
1259	266.910546	65.551014	$1.5192^{\pm 0.0003}$	$11.32^{\pm 0.01}$	1.70	L	Hα, ([N II])	Y
1263	266.639261	65.550909	$1.5130^{\pm 0.0008}$	$9.93^{\pm 0.38}$	1.19	L	Hα	Y
1271	266.737076	65.551622	$1.5240^{\pm 0.0027}$	$10.65^{\pm 0.06}$	0.71	M	Hα, [N II], [O III], Hβ	Y
1292	266.876375	65.552945	$1.5117^{\pm 0.0014}$	$11.41^{\pm 0.02}$	2.19	L	Hα, ([N II])	Y
1304	266.782085	65.552903	$1.5180^{\pm 0.0008}$	$10.23^{\pm 0.14}$	1.19	L/M	Hα, ([N II])	Y
1328	266.76224	65.552301	$1.5224^{\pm 0.0036}$	–	–	M	Hα	–

ID	R.A. (deg)	Dec. (deg)	Redshift	M_* $\log_{10}(M_\odot)$	SFR $\log_{10}(M_\odot yr^{-1})$	Inst. L/M	Lines	Stacking Y/–
1339	266.848079	65.552234	$1.5167^{\pm 0.0008}$	$10.10^{\pm 0.25}$	1.41	L	Hα, [N II]	Y
1369	266.810181	65.555050	$1.5211^{\pm 0.0007}$	$9.93^{\pm 0.21}$	0.80	L	Hα, ([N II])	Y
1400	266.711057	65.556204	$1.5150^{\pm 0.0034}$	$10.41^{\pm 0.09}$	1.29	M	Hα	Y
1412	266.803357	65.556741	$1.5135^{\pm 0.0030}$	$10.70^{\pm 0.05}$	1.20	M	Hα, ([N II])	Y
1422*	266.713480	65.557074	$1.5567^{\pm 0.0018}$	$11.45^{\pm 0.01}$	–	M	Hα	–
1456	266.722739	65.559353	$1.5124^{\pm 0.0017}$	$10.43^{\pm 0.09}$	1.25	L/M	Hα, ([N II])	Y
1461	266.909417	65.559817	$1.5129^{\pm 0.0011}$	$10.85^{\pm 0.07}$	1.84	L	Hα	Y
1500*†	266.86996	65.56176	$1.4523^{\pm 0.0019}$	–	–	M	[O III]	–
1509	266.736187	65.561929	$1.5232^{\pm 0.0008}$	$10.46^{\pm 0.09}$	1.65	L/M	Hα, [O III], Hβ	Y
1521	266.644548	65.562259	$1.5126^{\pm -0.0008}$	$10.87^{\pm 0.03}$	1.87	L	Hα, [N II]	Y
1554	266.682257	65.563721	$1.5154^{\pm 0.0004}$	$10.66^{\pm 0.07}$	1.89	L	Hα	Y
1567†	266.683695	65.564301	$1.5182^{\pm 0.0028}$	$11.00^{\pm 0.04}$	1.97	M	[O III], Hβ	–
1604*†	266.837147	65.565738	$1.4912^{\pm 0.0044}$	–	–	M	[O III]	–
1644*	266.73666	65.568059	$1.5180^{\pm 0.0026}$	–	–	M	Hα, [O III]	–
1887	266.767721	65.573595	$1.5391^{\pm 0.0026}$	$10.38^{\pm 0.16}$	1.28	M	Hα, (Hβ)	–

Note: We include marginal detection ($< 2\sigma$) in the column of "Lines" with the parentheses surrounding them. [O III] and Hβ lines are detected only for MOIRCS targets because of the wavelength coverage. There are seven galaxies whose Hα lines fall outside the range of NB1657 (marked as *). † means the objects identified only with [O III]. M_* and SFR are not shown for galaxies that were not detected at K-band or NB1657 in Koyama et al. (2014). "L" and "M" in the 'Inst.' column means galaxies observed with LUCI and MOIRCS, respectively. The errors in M_* are derived from the photometric uncertainties, while we assign typical 0.2-dex errors in *SFR* for all the galaxies (see Sec.B.2.3).

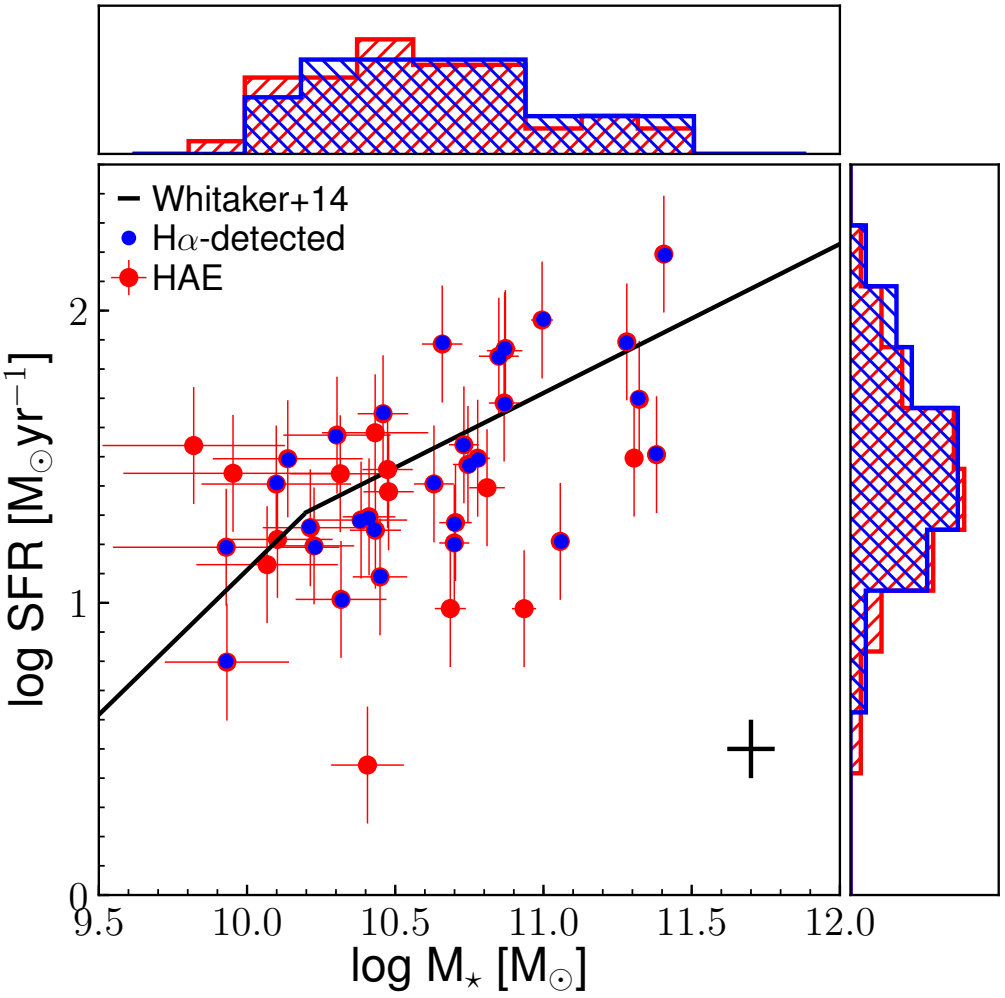

Figure B.1: The distribution of our sample on the stellar mass versus star formation rate plane. The red circles show Hα emitters (HAE) candidates selected in Koyama et al. (2014), and the blue points are HAEs confirmed by our spectroscopic observation. The solid black line indicates the star-forming main sequence at $z = 1.52$ (Whitaker et al. 2014). The error-bars for stellar mass are calculated from the photometric uncertainties in Koyama et al. (2014), while we adopt a typical uncertainty (~ 0.2 dex) in SFRs for all our sample (see B.2.3). The histograms in the top and right panels show the normalized distribution of stellar mass and SFR of the HAEs (red) and our spectroscopic members (blue), respectively.

B.3 Results

B.3.1 Redshift Distribution and 2D-map

We show in Fig.B.2 the redshift distribution of our spectroscopic sample. The blue, red, and magenta histograms indicate the number of galaxies observed with LUCI, MOIRCS, and both instruments. We use LUCI's results for the magenta histogram. The black solid-line curve drawn in Fig.B.2 is the average filter response function of the MOIRCS NB1657 filter at the center of the FoV. The dotted-line curves are the transmission at the edge of FoV (Tanaka et al., 2011); we note that the response function of the MOIRCS NB1657 filter changes with the location within the FoV. It is now clear that $z_{\rm spec}$ of galaxies in the 4C65.22 field are concentrated at $z = 1.510 - 1.525$ with very few outliers. This range is much narrower than the width of the narrow-band filter (even if we consider the wavelength shift of the filter transmission at the edge of the FoV), suggesting that these galaxies are concentrated in this small redshift range and not randomly distributed.

In Fig.B.3, we show the 2-D distribution of our spectroscopic sample. The triangles, squares, and circles indicate galaxies with spec-z determined by LBT/LUCI, Subaru/MOIRCS, and both instruments, respectively. The top and right panels show the projected distribution on the R.A.−z and Dec.−z plane, respectively. We can see that the relatively high-z data points tend to be located in the central region (or high-density regions). In contrast, the low-z data points tend to be located in the outskirts, suggesting that there are two large-scale filaments (or planes) crossing at the cluster's central region. Such complicated large-scale structures are often seen in the nearby Universe or numerical simulations. Our data suggest that the situation seems to be similar around this newly discovered structure at $z = 1.52$.

To determine the redshift of the cluster by eliminating the effect of surrounding structures, we here focus on galaxies located in the very central region. By taking the median of the $z_{\rm spec}$ for galaxies located within one arcmin from the density peak (corresponding to 500 kpc, green circle in Fig. B.3), we determine the redshift of this galaxy cluster to be $z = 1.517$. We note that there remains an uncertainty for the estimate of the cluster redshift because eight passive red galaxies dominating the very central region of the cluster are not observed in this study (see Koyama et al. 2014).

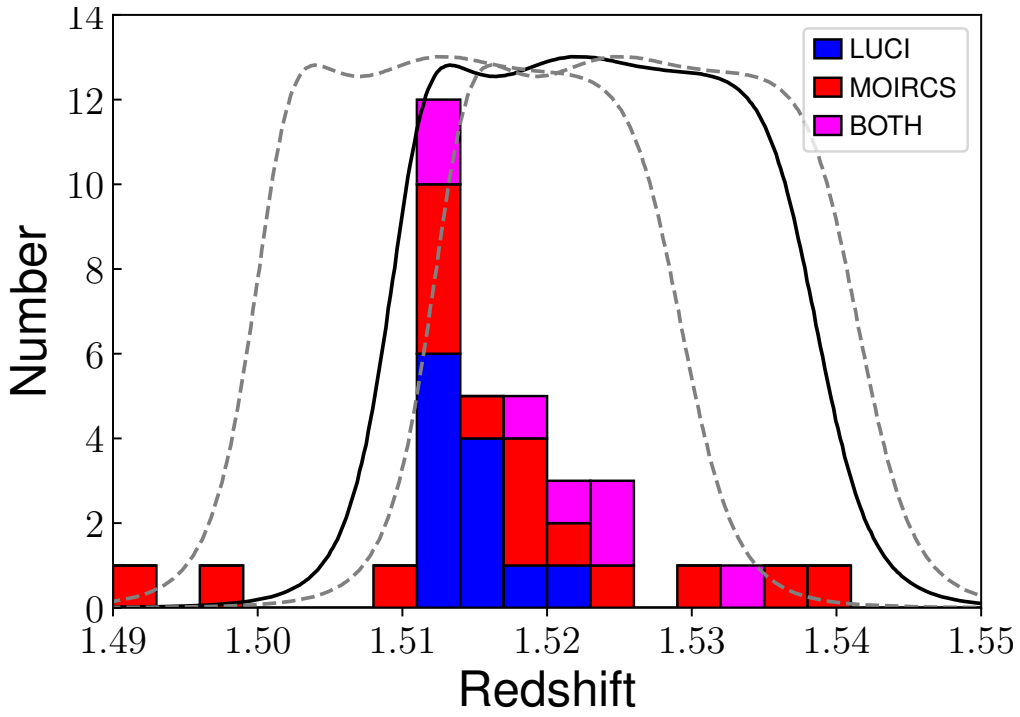

Figure B.2: Redshift distribution of all our spectroscopic sample at $z_{\rm spec} = 1.49 - 1.55$. The blue and red histograms show the number of galaxies observed with LBT/LUCI and Subaru/MOIRCS, respectively. Galaxies observed by both LUCI and MOIRCS are shown with the magenta histogram. The black- and grey-line curves represent the transmission curve of the MOIRCS narrow-band filter (NB1657) used in Koyama et al. (2014) at the center and the edge of the FoV, respectively (see Section B.2).

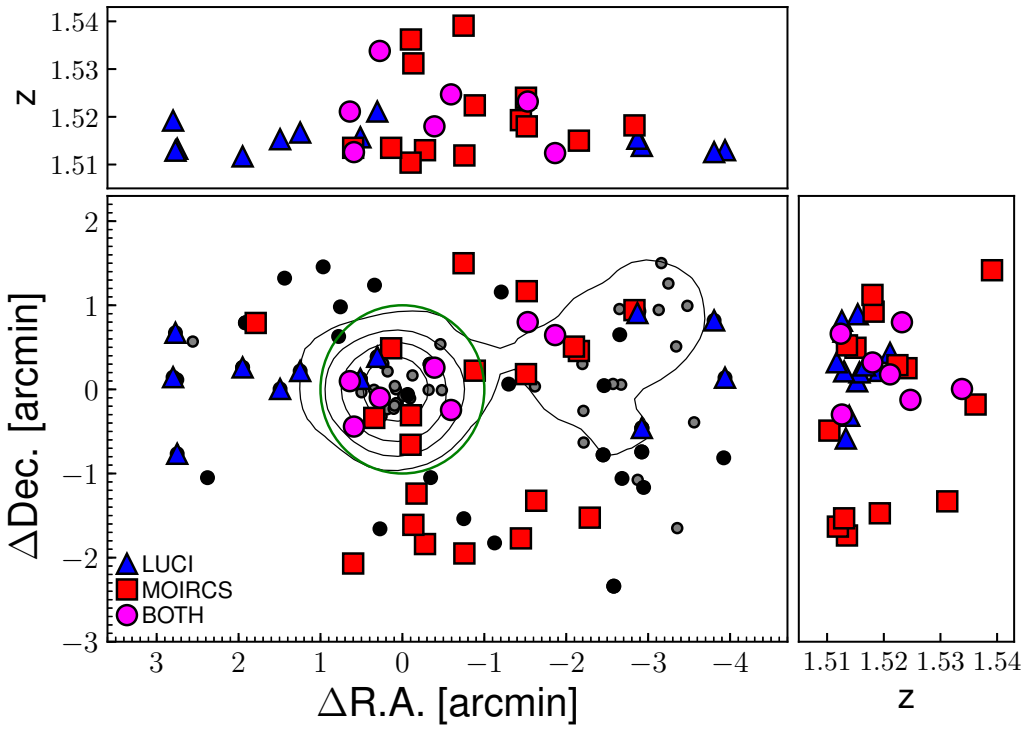

Figure B.3: 2-D distribution of the cluster member galaxies in the 4C65.22 field. The grey dots represent all the photometric member galaxies identified in Koyama et al. (2014), while the black circles indicate our spectroscopic targets. The triangles, squares, and circles show galaxies of which Hα line are detected with LBT/LUCI, Subaru/MOIRCS, and both. Galaxies within one arcmin from density peak (green circle) are used to determine the cluster redshift. The top and right panels show their projected distribution on the R.A.–z and Dec.–z plane, respectively. The black contours show the local density computed by using all the member galaxies from Koyama et al. (2014).

B.3.2 Stacking & Fitting

The next section will discuss the metallicity of the cluster member galaxies and their environmental dependence. However, the signal-to-noise ratios of our data are not very high (typically S/N(Hα)~4), and it is impossible to determine the metallicity of individual galaxies. We apply stacking analysis for carefully selected 19 galaxies observed with LUCI and 12 galaxies observed with MOIRCS, whose Hα and [N II] lines are not contaminated by strong O.H. sky lines. We note that this includes five galaxies observed with both LUCI and MOIRCS. To study the stellar mass dependence of the metallicity of cluster galaxies, we divide our sample into two equal-sized bins by the median stellar mass (at $10^{10.48} M_{\odot}$). Also, we account for LUCI and MOIRCS samples separately due to their different spectral resolution). We describe the detail of the stacking analysis below for each subsample.

We first determine the continuum level of individual galaxies by applying the linear fitting to the spectrum around Hα except for emission lines and subtract it from the individual spectrum. We then normalize the spectra by their Hα flux before stacking. We note that the details of the spectral stacking procedure are different from study to study. In particular, this flux normalization step is not performed in many studies. This step would not be necessary when we can assume that the galaxies used for stacking analysis have the same properties (e.g., in the case that the sample has the same stellar mass). However, the results would be biased to galaxies with more significant Hα flux. For example, since galaxies with large Hα flux are expected to have pristine gas that has less oxygen in general, this may lead to an underestimate of the mean metallicity of our sample. Another possible way for the spectral stacking is to stack the spectra without normalization with Hα flux (but putting a weight based on their background noise). Still, in this case, galaxies with strong Hα emission (hence with high S/N) would largely contribute to the results. Because we aim to study environmental dependence of the metallicity (determined by the Hα/[N II] flux ratio) at fixed stellar mass, we decided to normalize the spectra based on the Hα flux.

Finally, we stack the (normalized) spectra by calculating the mean flux density at each wavelength, weighted by the noise levels estimated in the original spectra (before normalization) because it represents the real quality of the spectra. We believe that the procedure described above is the best approach to study the mean Hα/[N II] flux ratio

in this study. Still, we verified that our conclusions are not changed even if we stack the spectra without any normalization. Fig. B.4 and B.5 show our stacked spectra for each subsample.

We fit Hα and [N II]λ6583 lines of the stacked spectra with double Gaussian function (blue lines in Fig. B.4 and B.5). We set the peak flux density and the velocity width of Hα and [N II]λ6583 as free parameters and assume the common velocity widths between Hα and [N II]λ6583. We note that [N II]λ6548 is also covered in the range of our spectroscopy, but we do not use it in our fitting process because of its low S/N ratio.

B.3.3 Mass-Metallicity Relation

The MZR is the correlation between galaxy stellar mass (M_*) and their oxygen abundance (e.g., Tremonti et al. 2004). In general, more massive galaxies tend to have higher metallicity, and the slope of the MZR becomes flatter in the massive end. Tremonti et al. (2004) suggested that the steepness of the MZR towards the low-mass end is related to the escape velocity of galactic outflow. Massive galaxies have profound potential well and require large escape velocity, which results in the decrease/suppression of outflowing gas. In other words, for more massive galaxies, a more significant fraction of outflowing gas/material driven by their star-forming activity returns to themselves. On the other hand, less massive galaxies have shallower potential well and require smaller escape velocity. This scenario is consistent with the predictions of numerical simulations as well as some observational results (e.g., Finlator & Davé 2008; Davé et al. 2012; Erb et al. 2006; Onodera et al. 2016; Sanders et al. 2018). In addition, the gas fraction of galaxies is another critical parameter that influences their gas-phase metallicity. For instance, gas-rich galaxies tend to have lower metallicity with higher star formation rate (e.g., Bothwell et al. 2013).

This part investigates environmental impacts on the chemical enrichment in (star-forming) galaxies in a cluster environment at $z = 1.52$. It should be noted that there are many metallicity calibrators used for distant galaxies. In this part, we use the [NII]/Hα method (Pettini & Pagel 2004) because of the limited wavelength coverage of our LUCI data. As we mentioned in the previous sections, we here use only 26 cluster member galaxies at $z = 1.52$ whose Hα and [N II]λ6583 are not contaminated by OH

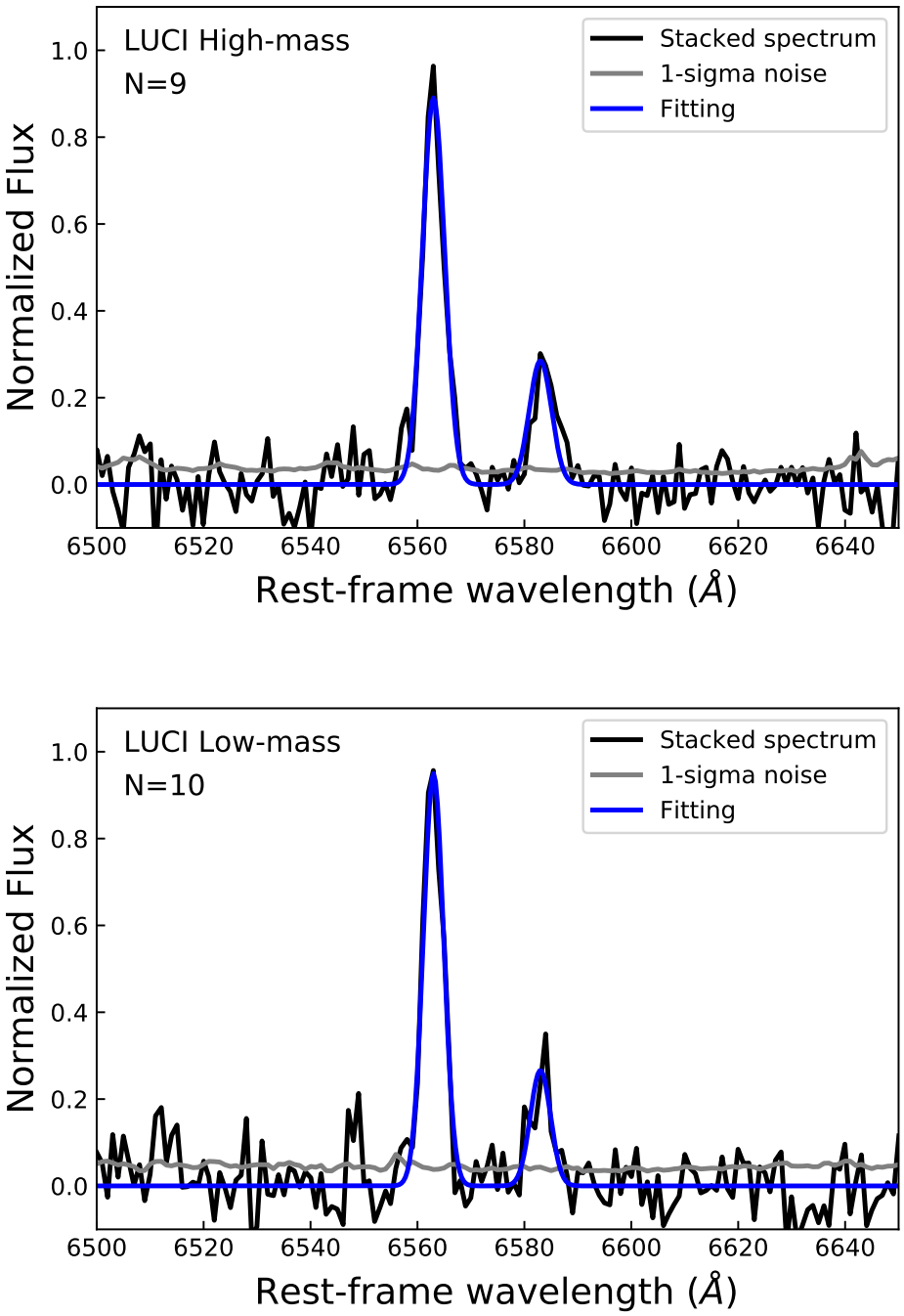

Figure B.4: The 1-D stacked spectra of our cluster galaxies observed by LUCI. The top and bottom panels show the results for high-mass and low-mass bins, respectively. The black and grey lines show the stacked spectra and its 1-sigma error calculated from original data. The blue-line curve shows the best-fit double gaussian.

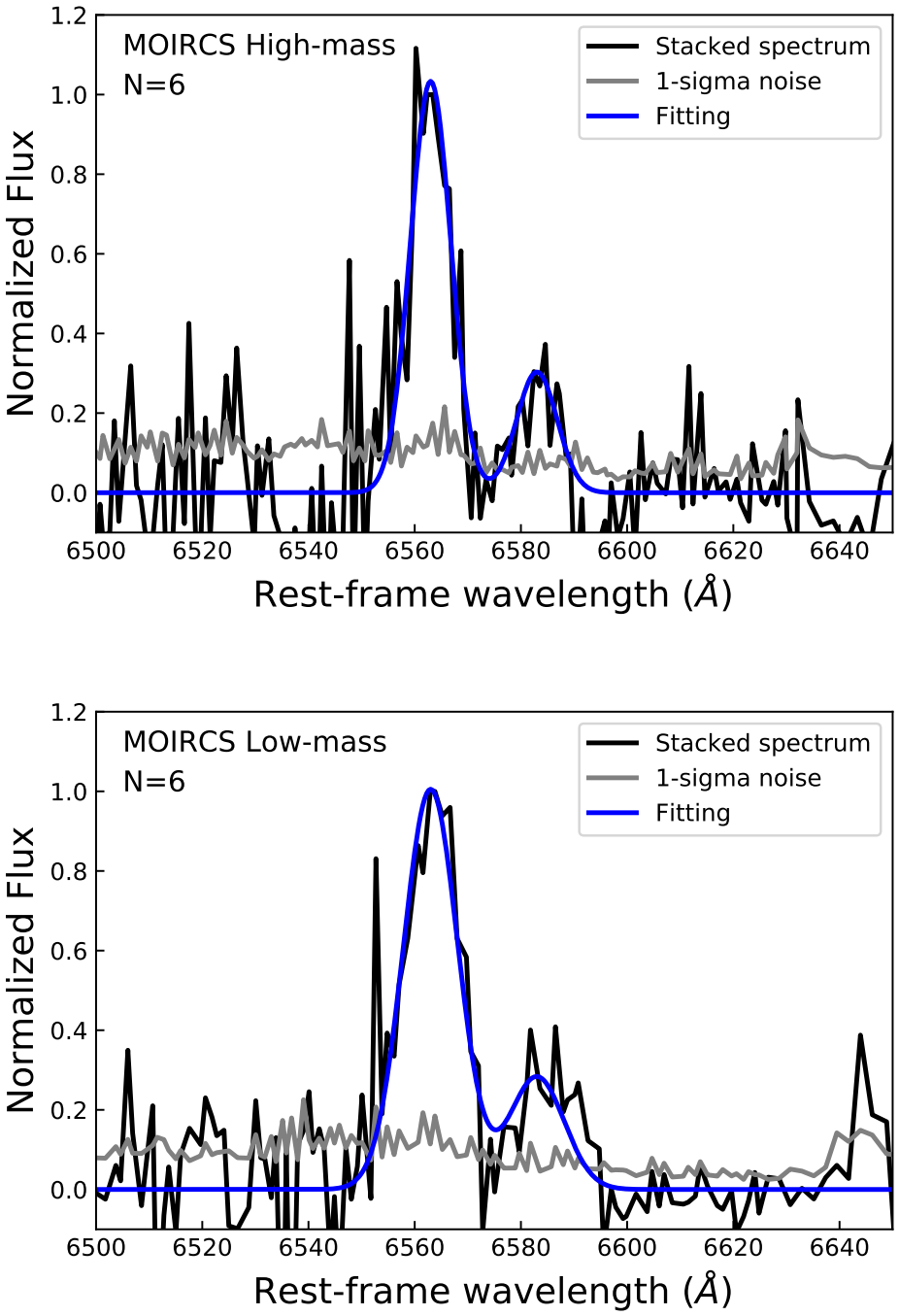

Figure B.5: The same figure to Fig.B.4 but for galaxies observed by MOIRCS.

emission lines, in order to derive the average [N II]/Hα line flux ratio (see Sec.B.2.3; B.3.2; Pettini & Pagel 2004).

We note that our sample is distributed over a wide stellar mass range. Some recent studies suggest that the environmental effect on MZR appears especially in the low-mass side (Kulas et al. 2013 and Shimakawa et al. 2015). To check this possibility, we divide our sample into the high- and low-mass subsamples based on their stellar mass (for LUCI and MOIRCS samples separately). Using the stacked spectrum of each subsample (see Fig.3.1), we calculate the N2 index, $N2 \equiv \log [\mathrm{N_{II}}]\lambda 6583/\mathrm{H}\alpha$, for each stacked spectrum. We then derive their mean metallicity with the equation of $12 + \log(O/H) = 8.90 + 0.57 \times N2$ (Fig.B.6).

In Fig.B.6, we compare the average metallicity of our sample with the MZR for general field galaxies at the same redshifts. The grey shaded region shows the MZR for field galaxies at $1.4 < z < 1.7$ derived by Zahid et al. (2014), and the solid black line indicates the result at $0.8 < z < 1.4$ derived by Stott et al. (2013), respectively. We note that the redshift range of the galaxy samples used in Stott et al. (2013) (313 at $z \sim 1.47$ and 68 at $z \sim 0.84$) is slightly different from that of our sample, but we believe that we can use their results as the comparison sample for our cluster galaxies at $z = 1.52$. In general, using a different method of metallicity calibration can produce other metallicity estimates. We here choose those two studies for our comparison because they use the exact metallicity calibration as our analysis (based on Pettini & Pagel 2004, N2 index) at similar redshifts. It can be seen that low-mass cluster galaxies ($10^{9.93} M_\odot < M_* < 10^{10.48} M_\odot$, blue symbols in Fig. B.6) tend to be more metal-rich than those in the field environment derived by Zahid et al. (2014), while the MZR at the same redshifts shown by Stott et al. (2013) is almost flat, which is in good agreement with our results. We expect that the different sample selection causes this difference between these two MZR for field galaxies. We will discuss more in detail the potential bias in Sec.B.4.1.

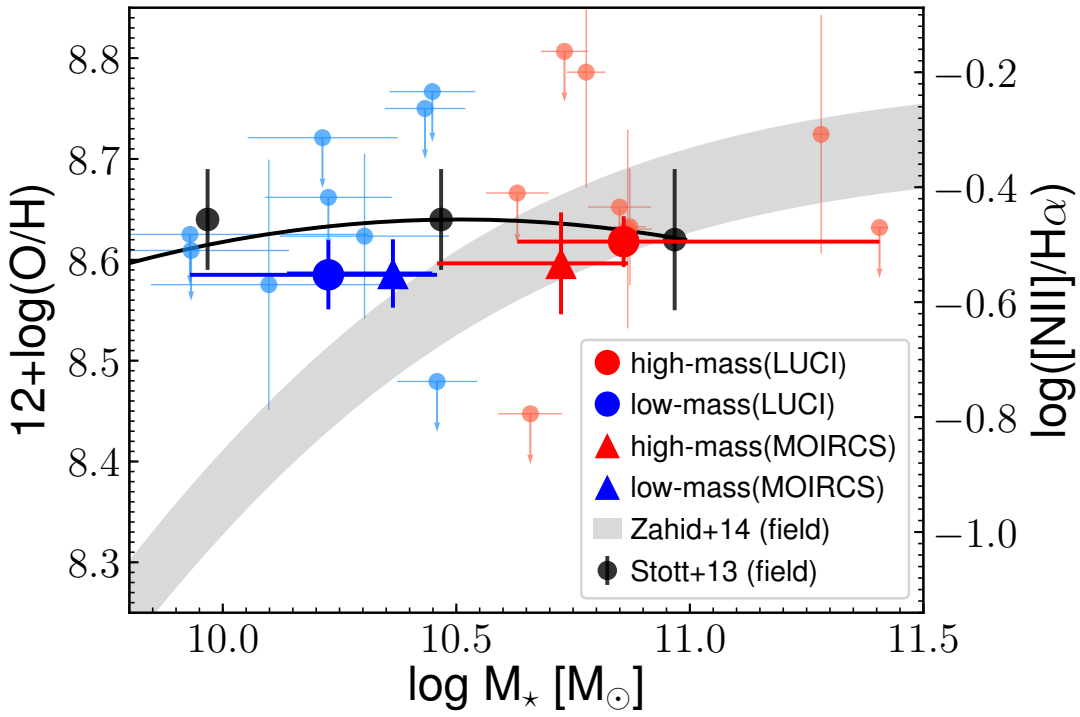

Figure B.6: The MZR for our low-mass (blue) and high-mass (red) cluster sample at $z = 1.52$. The triangles and circles indicate the results for MOIRCS and LUCI sample, respectively. The stellar mass is the median of each subsample and horizontal error bar shows its bin size. Light blue and red points show the metallicity of individual galaxies observed with LUCI ([N II]$> 2\sigma$) and their upper limit ([N II]$< 2\sigma$). For comparison, we also show the MZR for field galaxies at $1.4 < z < 1.7$ from Zahid et al. (2014) (grey shade), and those at $0.8 < z < 1.4$ from Stott et al. (2013) (black solid line).

B.4 Discussion

With large efforts to investigate the metallicity of galaxies in the high-z Universe over the last decade, it is now established that the MZR exists in the high-z Universe (Erb et al., 2006; Maiolino et al., 2008; Troncoso et al., 2014; Onodera et al., 2016; Sanders et al., 2018), which is also reproduced by recent numerical simulations (Torrey et al. 2012). However, only countable studies investigate the environmental dependence of the MZR at high redshifts, and a consensus has yet to be reached.

Kulas et al. (2013) and Shimakawa et al. (2015) showed that low-mass (proto-)cluster galaxies tend to have *higher* metallicity than those in the field environment. They interpreted this trend as a result of a high metallicity recycling rate caused by cluster gaseous IGM with high pressure. On the other hand, Tran et al. (2015) and Kacprzak et al. (2015) showed that there is *no* environmental dependence in the MZR. Kacprzak et al. (2015) also showed the comparable metallicity of galaxies in cluster and field by using hydrodynamical simulations. In contrast, Valentino et al. (2015) have investigated the MZR in a cluster at $z = 1.99$ and claimed that cluster galaxies have *lower* metallicity than those in the field environment. Their interpretation is that inflowing pristine gas would lower the gas metallicity within the galaxies and boost their SFR at the same time.

In this part, we have focused on star-forming galaxies in a newly confirmed galaxy cluster around the radio galaxy, 4C65.22, at $z = 1.52$. With LUCI and MOIRCS spectroscopy presented in this part, our results suggest that low-mass star-forming galaxies in the 4C65.22 field have slightly higher metallicity than those in Zahid et al. (2014) but comparable to Stott et al. (2013) (Fig.B.6). Below, we discuss which study is more appropriate for our comparison. Then we also discuss whether there is any environmental effect on the chemical enrichment in galaxies at this redshift.

B.4.1 Different Sample Selection

As shown in Fig.B.6, Stott et al. (2013) showed high metallicity in low-mass galaxies, implying a flat MZR, which is consistent with our results (black points and the connecting black line in Fig.B.6). On the other hand, MZR in Zahid et al. (2014) (grey shade in Fig.B.6) shows a clear difference from our results and Stott et al. (2013) in particular at the low-mass end ($10^{9.93} M_\odot < M_* < 10^{10.48} M_\odot$). We note that Stott

et al. (2013) selected their targets primarily based on their NB Hα imaging (HiZELS, $z = 0.84 - 1.47$; Sobral et al. 2013), while the targets in Zahid et al. (2014) are selected by the K-band magnitudes ($K < 23$ mag) and their broad-band colors.

Stott et al. (2013) explained that the reason for the discrepancy between their results and MZRs shown by previous studies is the effect of dust attenuation in the photometric selection in the rest-UV and optical bands, which can miss dusty galaxies, especially at the low-mass side. Stott et al. (2013) claimed that the previous MZRs could be biased from the low metallicity galaxies at the low-mass end because dusty galaxies tend to have higher metallicity. Also, Stott et al. (2013) pointed out that the samples in the previous studies are biased toward the higher SFR. Generally, galaxies with higher SFR tend to show lower metallicity, most likely driven by the increasing amount of pristine inflowing gas (Fundamental Metallicity Relation; Mannucci et al. 2010).

In order to avoid these biases, Zahid et al. (2014) selected their sample using K-band magnitude and color-color plane. Zahid et al. (2014) claimed that the effect of dust attenuation would move the object parallel to their criteria on the color-color diagram so that their sample is not affected by the dust compared with UV-selected galaxies used in the previous studies (Daddi et al. 2004). They also argued that their exposure time for each target is much longer than that in Stott et al. (2013), which enables them to observe galaxies down to lower SFRs. For these reasons, Zahid et al. (2014) conclude that their MZR and their suggestion on the redshift evolution of MZR should be valid.

Although the exact reason for the discrepancy between the results of these studies is unclear, we use the MZR of Stott et al. (2013) as the field sample. We note that the choice of different field samples for the comparison can lead to a different interpretation of the environmental impacts on the MZR. Our original sample was selected with the narrow-band Hα imaging survey performed by Koyama et al. (2014), which is the same method as Stott et al. (2013) for field galaxies.

B.4.2 Fundamental Metallicity Relation

Stott et al. (2013) fit the relation between the stellar mass, SFR, and the metallicity of their sample at $z = 0.8 - 1.47$ using the 2-variable polynomial (Fundamental Metallicity Relation, FMR). The typical scatter around the best-fit relation for their sample (σ) is 0.2 dex. Their scatter is about a factor of two smaller than the scatter around the

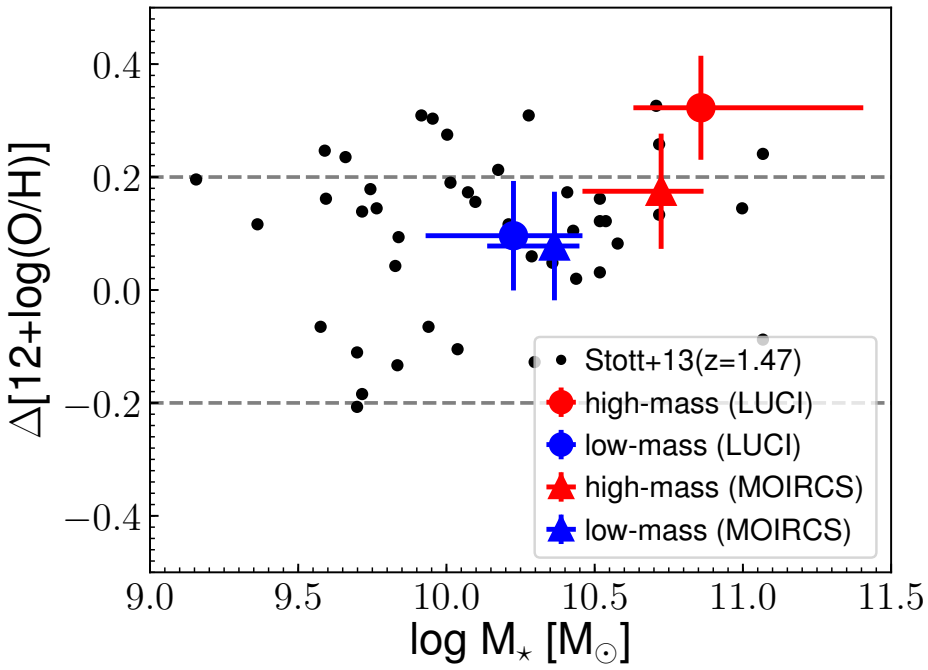

Figure B.7: The offset from the fundamental plane established by Stott et al. (2013) (in the metallicity direction) against the stellar mass for our cluster sample (colored symbols; the meanings of the symbols are the same as Fig.B.6). The black points are the HiZELS-FMOS sample at $z = 1.47$ from Stott et al. (2013). Both high- and low-mass samples of our MOIRCS data and the low-mass sample for our LUCI data are located within the 1σ (0.2 dex, grey dashed lines) from the field FMR. The high-mass sample of LUCI data shows a slightly larger offset, but it is still within the 2σ level.

fundamental plane reported for local galaxies (Mannucci et al. 2010). Stott et al. (2013) suggested the FMR evolves with redshift, while the original work by Mannucci et al. (2010) suggested that the FMR does not change over the cosmic time.

In order to evaluate the environmental effects on the chemical enrichment in galaxies in the 4C65.22 cluster field, we here calculate the metallicity offset from the FMR of Stott et al. (2013), $\Delta[12+\log(O/H)] = (12+\log(O/H))_{obs} - (12+\log(O/H))_{S13}$, and the results are shown in Fig.B.7.

We find that both low- and high-mass MOIRCS subsamples and the low-mass LUCI sample show $\Delta[12+\log(O/H)] < 1\sigma$. The LUCI high-mass sample shows a slightly larger deviation from the FMR of Stott et al. (2013), but it is still within the 2σ level.

Therefore, we conclude that our sample has similar properties in their gas-phase metallicity to the field galaxies at similar redshifts. The consistency between our cluster and field FMR in Stott et al. (2013) can be interpreted as the balance between the inflow and outflow in the dense environment looks not affected by the global environment.

B.5 Summary

We present the results of our NIR spectroscopic observations with LUCI and MOIRCS of 71 star-forming galaxies in a high-redshift ($z = 1.52$) galaxy cluster candidate discovered by Koyama et al. (2014). We successfully determined the spectroscopic redshifts of 39 galaxies with Hα and [O III]λ5007 lines. We confirm the redshift of the central region in this cluster to be $z = 1.517$ (< 500 kpc from the peak of galaxy over-density) and confirm that this is a real, physically associated, well-matured cluster at $z = 1.517$. By mapping the 3-D structures around the cluster, we find a hint that this cluster is located at the intersection of two filaments/sheet-like structures, and the large-scale structures may be extended even beyond our survey field.

We then divide our spectroscopic members of this cluster environment into two subsamples by the median of their stellar mass, at $10^{10.48} M_{\odot}$ (for those observed with LUCI and MOIRCS separately). For each subsample, we performed stacking analysis after subtracting continuum and normalizing each spectrum by their Hα flux. We derived "mean" metallicity of each subsample without being affected by those with very strong OH sky lines. Using these stacked spectra and the commonly used N2 method developed by Pettini & Pagel (2004), we investigated the environmental dependence of gas-phase metallicity in galaxies at $z \sim 1.5$. We note that our sample would not be strongly affected by type-1 AGNs, but we cannot rule out the possibility of some contamination from type-2 AGNs with the current data alone.

By comparing the MZR of our cluster sample to that of field galaxies at similar redshifts derived by Stott et al. (2013), we find that the metallicity of our targets is consistent with the field galaxies. On the other hand, the metallicity of our less massive galaxies ($10^{9.93} M_{\odot} < M* < 10^{10.48} M_{\odot}$) shows a slight enhancement from the MZR of Zahid et al. (2014). Importantly, our targets and the sample in Stott et al. (2013) are selected by NB (Hα) selection, while Zahid et al. (2014) select their sample by the K-band magnitude. The discrepancy between the two studies for field galaxies could be caused by their different sample selection, and thus we consider that it would be more appropriate to compare our results to Stott et al. (2013), who selected their spectroscopic sample from the NB (Hα) imaging data.

We then investigated the metallicity offset of our cluster sample from the FMR shown by Stott et al. (2013). We find that both of our MOIRCS subsamples and the

LUCI low-mass sample are consistent with the FMR of Stott et al. (2013) within 1σ. The LUCI high-mass sample shows a slightly larger offset, but it is still within 2σ level. We therefore conclude that our cluster galaxies have the gas-phase metallicity comparable to the field galaxies at similar redshifts.

It should be noted that some previous studies show a lower, consistent, and higher metallicity in high-z clusters compared to field galaxies (e.g. Kulas et al. 2013; Shimakawa et al. 2015; Valentino et al. 2015; Tran et al. 2015; Kacprzak et al. 2015). The authors always try to introduce some preferable mechanisms to explain their results; e.g. higher recycling rate, enriched IGM, and pristine inflow, all of which are supported by the observations or simulations (e.g. Davé et al. 2008, 2011; Dekel et al. 2009; Ellison et al. 2013; Torrey et al. 2012). Continuous efforts for determining the MZR in high-z cluster environments are necessary to understand whether environment would ubiquitously affect the galaxy metallicity and, if the environment really matters, we need to understand what kind of process is at work.